

ON MIXED-INTERPOLATED GENERAL SHELL FINITE  
ELEMENTS FOR NONLINEAR ANALYSIS

by

Seong Wook Cho

B.S.M.E., Seoul National University (1979)  
M.S.M.E., Korea Advanced Institute of Science and Technology (1981)

Submitted to the Department of Mechanical Engineering  
in partial fulfillment of the requirements  
for the degree of


Doctor of Philosophy

at the

MASSACHUSETTS INSTITUTE OF TECHNOLOGY

December 1990

© Massachusetts Institute of Technology 1990

Signature of Author.....  .....

Department of Mechanical Engineering

December 3, 1990

Certified by.....

Klaus-Jürgen Bathe

Department of Mechanical Engineering

Thesis Supervisor

Accepted by.....  .....

Chairman of the

Thesis Committee

MASSACHUSETTS INST  
OF TECHNOLOGY

APR 26 1991

LIBRARIES

# ON MIXED-INTERPOLATED GENERAL SHELL FINITE ELEMENTS FOR NONLINEAR ANALYSIS

by

Seong Wook Cho

Submitted to the Department of Mechanical Engineering  
on December 3, 1990, in partial fulfillment of the  
requirements for the degree of  
Doctor of Philosophy

## Abstract

New plate and shell elements for nonlinear finite element analysis are presented. These elements are formulated using three-dimensional continuum mechanics theory with degeneration and mixed-interpolations, and they are applicable to the analysis of thin and moderately thick shells.

The mixed-interpolated plate bending elements are based on Reissner/Mindlin plate theory with interpolation of the transverse displacement, section rotations and transverse shear strain components. The elements considered are various 9 and 16-node quadrilateral elements, as well as 7 and 12-node triangular elements. Although the theory for most of these elements had been proposed earlier, the elements have not been studied in great detail. In this thesis the formulation of these elements is summarized and some numerical results are presented which demonstrate the high predictive capabilities of the elements.

In the case of a general nonlinear shell analysis, the 9-node mixed-interpolated plate bending element is extended to a general nonlinear shell element. In addition to the separate transverse shear strain interpolation, in-plane strains are also interpolated to improve the membrane action of the element. Various interpolation fields for the in-plane strains are studied. The tying scheme between the displacement assumptions and the strain assumptions is also studied for the proposed element, and an efficient computational scheme is proposed.

A study is performed to identify the characteristics of the elements regarding convergence, distortion sensitivity, and applicability to thin and moderately thick shells. It is demonstrated that the elements are reliable and very effective in both linear and nonlinear analysis. The key features of the elements are a sound mathematical foundation and an efficient computational algorithm.

Thesis Supervisor: Klaus-Jürgen Bathe  
Title: Professor of Mechanical Engineering

*To my wife Hye Sun  
For her love and patience*

# Acknowledgements

I would like to express my appreciation to Professor Klaus-Jürgen Bathe for his continuous interest, encouragement, and guidance throughout this research and I am grateful for his support. I am also grateful to Professor Rohan Abeyaratne and Professor Oral Buyukozturk for their valuable advice as members of my thesis committee.

I am indebted to the past and current colleagues of our Finite Element Research Group for their comments and suggestions. I give my special thanks to Mr. Hyun-Seok Yang and Mr. Hyunjune Yim for their help in preparing the illustrations, and to Mr. Seung Jin Song and Mr. Dae Eun Kim for their help in proofreading the thesis.

I am also most grateful to the Korean Government for the fellowship that made it possible for me to study at M.I.T.

Last but not the least, I would like to express my utmost gratitude to my wife Hye Sun, my mother, and my family. Because of their sacrifices, I was able to pursue my education.

# Contents

<b>Titlepage</b>	<b>1</b>
<b>Abstract</b>	<b>2</b>
<b>Dedication</b>	<b>3</b>
<b>Acknowledgments</b>	<b>4</b>
<b>Contents</b>	<b>5</b>
<b>List of Figures</b>	<b>8</b>
<b>List of Tables</b>	<b>10</b>
<b>1 Introduction</b>	<b>11</b>
<b>2 The Mixed-Interpolated Plate Bending Elements</b>	<b>16</b>
2.1 Mathematical Background . . . . .	16
2.2 The Elements . . . . .	21
2.2.1 The MITC4 Element . . . . .	21
2.2.2 The MITC7 Element . . . . .	23
2.2.3 The MITC9 Element . . . . .	27
2.2.4 The MITC12 Element . . . . .	30
2.2.5 The MITC16 Element . . . . .	31

---

2.2.6	The MITC8 Element . . . . .	32
2.3	Reliability of the Elements . . . . .	33
2.3.1	Patch Test . . . . .	34
2.3.2	Analysis of a Square Plate . . . . .	34
2.3.3	Analysis of a Circular Plate . . . . .	53
<b>3</b>	<b>Formulation of the Mixed-Interpolated Nine-Node Shell Element</b>	<b>65</b>
3.1	Kinematics . . . . .	66
3.2	Displacement-Based Shell Element . . . . .	67
3.3	Formulation of the Mixed-Interpolated Shell Element . . . . .	76
3.3.1	In-Layer Strain Interpolation . . . . .	78
3.3.2	Transverse Shear Strain Interpolation . . . . .	79
3.4	Tying Scheme for Shell Element . . . . .	81
3.5	Incremental Formulation . . . . .	85
<b>4</b>	<b>Analysis of the Mixed-Interpolated Shell Element</b>	<b>87</b>
4.1	Covariant Strain Interpolation and Its Analysis . . . . .	87
4.1.1	Covariant Strain in a One-Dimensional Bar . . . . .	88
4.1.2	Covariant Strain Interpolations in a Square Plate . . . . .	91
4.2	Improvement of the Eight-Node Element . . . . .	94
4.3	Discussion of Different Interpolation Fields for the Nine-Node Elements	99
4.4	Implementation . . . . .	109
<b>5</b>	<b>Numerical Tests and Problem Solutions</b>	<b>117</b>
5.1	Stability of the Element . . . . .	117
5.2	Sample Analyses . . . . .	120
5.2.1	Analysis of a Perforated Tension Strip . . . . .	120
5.2.2	Analysis of a Cantilever under Distributed Load . . . . .	120
5.2.3	Analysis of Morley Skew Plate . . . . .	120
5.2.4	Analysis of Scordelis-Lo Cylindrical Roof . . . . .	122

---

5.2.5	Analysis of a Pinched Cylindrical Shell . . . . .	124
5.2.6	Fundamental Frequency of a Cantilever . . . . .	128
5.2.7	Fundamental Frequency of a Simply Supported Plate . . . . .	128
5.2.8	Analysis of a Cantilever under Large Displacement . . . . .	128
5.2.9	Large Displacement Analysis of a Simply-Supported Plate . . . .	135
5.2.10	Linearized Buckling Analysis of a Circular Arch . . . . .	141
5.2.11	Large Deflection Analysis of a Shallow Cylindrical Shell . . . . .	141
<b>6</b>	<b>Concluding Remarks</b>	<b>144</b>
	<b>References</b>	<b>146</b>
<b>A</b>	<b>Appendix</b>	<b>151</b>
A.1	Comparison between the MITC9 and MITC9 <sup>I</sup> Elements . . . . .	151

# List of Figures

2-1	Nodal point variables for each of the MITC elements. . . . .	24
2-2	Gauss points used for tying of covariant shear strain components. . . . .	28
2-3	Patch of the elements used in a patch test. . . . .	35
2-4	Stress distribution in the patch using the MITC9 <sup>I</sup> elements. . . . .	36
2-5	Analysis of a square plate. . . . .	39
2-6	Convergence of center displacement of a clamped square plate. . . . .	44
2-7	Displacement/stress response of a simply supported square plate. . . . .	46
2-8	Graded mesh used in a simply-supported plate. . . . .	50
2-9	Shear stress predictions of a simply-supported square plate. . . . .	51
2-10	Finite element meshes used for the analysis of a circular plate. . . . .	54
2-11	Displacement/stress response of a circular plate. . . . .	56
2-12	Finite element meshes used for the analysis of clamped circular plate. . . . .	60
2-13	Distorted mesh used for a clamped circular plate. . . . .	61
2-14	Radial bending stress prediction in a clamped circular plate. . . . .	62
2-15	Transverse shear stress predictions in a clamped circular plate. . . . .	63
2-16	Transverse shear stress predictions in a clamped circular plate. (Distorted mesh) . . . . .	64
3-1	The geometry of the typical shell element. . . . .	67
3-2	Definition of rotational degrees of freedom. . . . .	68
3-3	Sampling points used for the MITC9 and MITC8 <sup>N</sup> shell elements. . . . .	80
3-4	Reduced integration for integral tying. . . . .	83



---

4-1	Covariant strains in a truss element. . . . .	90
4-2	Sampling points for the membrane strain interpolation . . . . .	91
4-3	Lines of shear strain plot. . . . .	95
4-4	Shear strain oscillation in a circular plate. . . . .	96
4-5	Shear stress oscillation in a square plate. . . . .	100
4-6	Physical model of the curved cantilever considered. . . . .	101
4-7	Analysis of a curved cantilever beam. . . . .	104
4-8	Base vector variation in a curved cantilever beam. . . . .	107
5-1	Patch of the elements used in a patch test. . . . .	119
5-2	Analysis of a perforated tension strip. . . . .	121
5-3	Analysis of a cantilever under a distributed load. . . . .	122
5-4	Analysis of Morley skew plate. . . . .	123
5-5	Analysis of Scordelis-Lo cylindrical roof. . . . .	125
5-6	Analysis of a pinched cylindrical shell. . . . .	129
5-7	Fundamental frequency of a cantilever. . . . .	132
5-8	Fundamental frequency of a simply supported plate. . . . .	133
5-9	A cantilever under large displacement. . . . .	136
5-10	Large displacement analysis of a simply-supported plate. . . . .	140
5-11	Linearized buckling analysis of a circular arch. . . . .	142
5-12	Analysis of a shallow cylindrical shell. . . . .	143
A-1	Points used for the shear strain interpolation. . . . .	152

# List of Tables

2-1	Analysis of a square plate. . . . .	41
2-2	Analysis of a circular plate under a concentrated load. . . . .	55
4-1	A curved cantilever under the tip moment for various mesh distortions. .	102
4-2	Response of a horizontally distorted curved cantilever. . . . .	108
5-1	Number of iterations for the cantilever analysis using the MITC9 element.	138
5-2	Convergence ratio for the out-of-balance energy at time step 10. . . . .	139

# Chapter 1

## Introduction

Although much research effort has been focused on developing reliable and efficient plate and shell elements, the need for improved elements persists. For a shell finite element to be generally applicable to both linear and nonlinear shell analyses with high reliability, it must satisfy, among others, the following three important conditions [Bathe and Dvorkin, 1986; Bathe, 1982; Bathe and Ho, 1981b].

- The element should be applicable to general shell structures.
- The element should be mechanistically clear and “numerically sound”: it must not contain any spurious zero energy modes; it must not ever lock; and it must not depend on numerically adjusted factors.
- The predictive capability of the element should be high and relatively insensitive to geometric distortions of the element.

Many elements proposed in the literature for analyzing plates and shells violate these conditions to a high degree. While some elements satisfy these conditions to a certain extent, only a few elements are useful for engineering practice, and even these elements require further improvements.

A promising approach towards the development of general plate and shell elements has been the use of the isoparametric formulation [Bathe and Bolourchi, 1980; Bathe,

1982]. However, in the formulation of isoparametric plate and shell elements (degenerate from three-dimensional conditions, or equivalently for plate analysis, based on Reissner/Mindlin plate theory), the only purely displacement-based element that may be recommended for general practical analysis of plates and shells is the 16-node bicubic element with  $4 \times 4$  Gauss integration [Bathe, 1982]. And yet, while being reliable, and in some analyses efficient, the element can exhibit a rather low convergence rate when geometrically distorted elements are used. This is largely due to the effects of membrane and shear locking which, though negligible when the element is flat and undistorted, increase as the element is geometrically distorted — a highly undesirable phenomenon.

Recently, much research effort has been concentrated on establishing reliable and efficient lower-order elements, and improving the performance of the 16-node element. Since the displacement-based isoparametric elements suffer major deficiencies, many authors have proposed lower order (4-node and 9-node) elements based on reduced integration [Hughes *et al.*, 1978]. However, the selectively reduced integrated elements exhibit poor convergence for some problems. Furthermore, the uniformly reduced integrated element is rank deficient, even though this element may be convergent in some cases.

To satisfy the above requirements, a new approach based on *assumed strains* has been proposed by Bathe *et al.* The approach is based on *Mixed-Interpolated Tensorial Components* (hence the resulting elements are referred to as MITC elements), and a 4-node element (the MITC4 element) [Dvorkin and Bathe, 1984; Bathe and Dvorkin, 1985] and an 8-node element (the MITC8 element) [Bathe and Dvorkin, 1986] have been proposed. These elements employ the same nodal degrees of freedom as the standard displacement-based isoparametric elements, but the strain fields are also assumed in the elements. The assumed strain field,  $\underline{\varepsilon}$ , used in these elements is expressed as:

$$\underline{\varepsilon} = \sum_{i=1}^N h_i \underline{\varepsilon}_i^{DI}$$

where  $\underline{\epsilon}|_i^{DI}$  is the strain tensor at the tying point  $i$  which is calculated from the strains directly evaluated by the displacement assumptions, and  $h_i$  are the interpolation functions for the strain assumptions.

While the MITC4 shell element shows excellent performance, higher-order curved elements can be considered to be advantageous in the following circumstances:

- Modeling curved boundaries.
- In dynamic analysis, higher order elements are usually more effective.
- Shell structures in which the stresses vary rapidly.

During the recent years, many authors also proposed other assumed strain plate/shell elements [MacNeal, 1982; Crisfield, 1984; Park and Stanley, 1986; Huang and Hinton, 1986; Jang and Pinsky, 1987; Jang and Pinsky, 1988]. These elements have been largely developed for linear analysis, even though they supposedly “can easily be extended to general nonlinear analysis”. Practical implementations show that the extension of a linear plate bending element formulation to a general effective shell element is not trivial, and that for some plate element formulations, this extension is almost impossible. Most of these assumed strain elements were based on physical insight and numerical experiments.

The MITC4 and MITC8 shell elements were proposed in [Bathe and Dvorkin, 1985; Bathe and Dvorkin, 1986; Dvorkin and Bathe, 1984]. Since the construction of these elements was based on insights about the element behavior and the use of the patch test, there has been a continuous effort to derive a more mathematically rigorous formulation [Bathe and Brezzi, 1985; Brezzi and Bathe, 1986]. Based on the mathematical analogies between the linear plate formulation and the analysis of incompressible media [Sussman and Bathe, 1987], the MITC4 element has been analyzed mathematically. These mathematical considerations have led to some interesting and general results for the linear analysis of plates and suggestions for the additional MITC elements for the plate bending problem [Bathe and Brezzi, 1987; Brezzi *et al.*, 1989]. Since these new plate bending elements were constructed much like the MITC4 and MITC8 elements, elements for the

general shell analysis could be developed using similar approach as that of the MITC4 and MITC8 elements [Bathe and Dvorkin, 1986].

The major objective of this research is to develop a reliable and high-order accurate finite element formulation for the analysis of general plate/shell structures in CAE applications. The approach has been to fully understand and evaluate the performance of the mathematically proposed plate elements before attempting to develop a general shell element formulation. Hence the research for this thesis has been divided into three major parts:

1. Development and implementation of various plate bending elements as suggested by mathematical analysis.
2. Performance evaluation of various MITC plate bending elements, including the MITC7, MITC9, MITC12 and MITC16 elements.
3. Extension of the MITC9 plate bending element to a general shell element.

The extension of the MITC9 plate element to a general shell element involves the following tasks:

- Research and development of an effective in-plane strain field assumption for the shell element.
- Development of an efficient computational scheme for the element matrix evaluations.

In order to design an element free from “locking” problems, the proper choice of an assumed strain field is essential. The MITC plate elements which employ the mathematically proposed transverse shear strain field show good performance, as predicted theoretically. For a general shell element, the proper choice of the in-plane strain field is also necessary to prevent membrane locking.

An efficient computational scheme for the strain field interpolation was also developed for the proposed element, and the treatment of the tying constraints was studied.

The proposed solution procedure was tested numerically on various problems for which either analytical solutions or experimental test results were available.

# Chapter 2

## The Mixed-Interpolated Plate Bending Elements

In this chapter, a family of finite element approximations for Reissner/Mindlin plates are presented. Essentially, the whole family is based on a common idea, which is to combine in a proper way the approximation of Stokes problems with the approximation of linear elliptic problems. The mathematical analysis provides the requirements which the mixed interpolated plate elements must satisfy.

### 2.1 Mathematical Background

The analysis summarized here is in some sense a simplified one. While a more general analysis is available for the 4-node element, only the limiting case as the thickness,  $t$ , approaches zero is discussed in this section. Consider the spaces:  $(\underline{\Theta} = (H_0^1(\Omega))^2$  and  $W = H_0^1(\Omega))$ , and a load function  $f$  given in  $L^2(\Omega)$ . A typical sequence of problems of the Reissner/Mindlin plate under consideration is:

$$P_t : \quad \inf_{\underline{\varrho} \in \underline{\Theta}, w \in W} \frac{t^3}{2} a(\underline{\varrho}, \underline{\varrho}) + \frac{\lambda t}{2} \|\underline{\varrho} - \nabla w\|_0^2 - t^3(f, w). \quad (2.1)$$



where  $\frac{t^3}{2}a(\underline{\theta}, \underline{\theta})$  is the internal bending energy, and  $\frac{\lambda t}{2} \|\underline{\theta} - \underline{\nabla}w\|_0^2$  is the shear energy.  $\|\cdot\|_0$  and  $(\cdot, \cdot)$  represent the norm and the inner product in  $L^2(\Omega)$  respectively.

Assume now that we are given the finite element subspaces  $\underline{\mathcal{Q}}_h \subset \underline{\mathcal{Q}}$  and  $W_h \subset W$ . The corresponding discretized problem is described by

$$\tilde{P}_{th} : \quad \inf_{\underline{\theta}_h \in \underline{\mathcal{Q}}_h, w_h \in W_h} \frac{t^3}{2}a(\underline{\theta}_h, \underline{\theta}_h) + \frac{\lambda t}{2} \|\underline{\theta}_h - \underline{\nabla}w_h\|_0^2 - t^3(f, w_h). \quad (2.2)$$

In general,  $\tilde{P}_{th}$  “locks” for small  $t$ . A common procedure to overcome this problem is to reduce the influence of the shear energy. Consider the case in which the reduction is carried out in the following way: assume that we are given a third finite element space,  $\underline{\Gamma}_h$ , and a linear operator  $R$  which takes the values in  $\underline{\Gamma}_h$ . Then  $\|R(\underline{\theta}_h - \underline{\nabla}w_h)\|_0^2$  can be used in place of  $\|\underline{\theta}_h - \underline{\nabla}w_h\|_0^2$  in the expression of the shear energy. It is further assumed that

$$R\underline{\nabla}w_h = \underline{\nabla}w_h \quad \text{for all } w_h \in W_h \quad (2.3)$$

so that the discretized problem takes its final form

$$P_{th} : \quad \inf_{\underline{\theta}_h \in \underline{\mathcal{Q}}_h, w_h \in W_h} \frac{t^3}{2}a(\underline{\theta}_h, \underline{\theta}_h) + \frac{\lambda t}{2} \|R\underline{\theta}_h - \underline{\nabla}w_h\|_0^2 - t^3(f, w_h). \quad (2.4)$$

Setting

$$\underline{\gamma} = \lambda t^{-2}(\underline{\theta} - \underline{\nabla}w) \quad \text{and} \quad \underline{\gamma}_h = \lambda t^{-2}(R\underline{\theta}_h - \underline{\nabla}w_h), \quad (2.5)$$

the Euler equations of  $P_t$  and  $P_{th}$  are respectively

$$\begin{aligned} a(\underline{\theta}, \underline{\eta}) + (\underline{\gamma}, \underline{\eta} - \underline{\nabla}\zeta) &= (f, \zeta) \quad \forall \underline{\eta} \in \underline{\mathcal{Q}}, \quad \forall \zeta \in W \\ \underline{\gamma} &= \lambda t^{-2}(\underline{\theta} - \underline{\nabla}w), \end{aligned} \quad (2.6)$$

and

$$\begin{aligned} a(\underline{\theta}_h, \underline{\eta}) + (\underline{\gamma}_h, R\underline{\eta} - \underline{\nabla}\zeta) &= (f, \zeta) \quad \forall \underline{\eta} \in \underline{\mathcal{Q}}_h, \quad \forall \zeta \in W_h \\ \underline{\gamma}_h &= \lambda t^{-2}(R\underline{\theta}_h - \underline{\nabla}w_h). \end{aligned} \quad (2.7)$$

We may note that the limit problems are

$$\begin{aligned} a(\underline{\theta}, \underline{\eta}) + (\underline{\gamma}, \underline{\eta} - \underline{\nabla}\zeta) &= (f, \zeta) \quad \forall \underline{\eta} \in \underline{\Theta}, \forall \zeta \in W \\ \underline{\theta} &= \underline{\nabla}w \end{aligned} \tag{2.8}$$

and

$$\begin{aligned} a(\underline{\theta}_h, \underline{\eta}) + (\underline{\gamma}_h, R\underline{\eta} - \underline{\nabla}\zeta) &= (f, \zeta) \quad \forall \underline{\eta} \in \underline{\Theta}_h, \forall \zeta \in W_h \\ R\underline{\theta}_h &= \underline{\nabla}w_h. \end{aligned} \tag{2.9}$$

**Remark 1** The limit problems in Eq. 2.8 and Eq. 2.9 were analyzed in refs. [Bathe and Brezzi, 1987] and [Brezzi *et al.*, 1989]. Even though incomplete, such analysis gives valuable insight into the behavior of element formulations when applied to the analysis of very thin plates.

**Remark 2** It can be shown that Eq. 2.8 and Eq. 2.9 are the limit problems of Eq. 2.6 and Eq. 2.7 respectively [Bathe and Brezzi, 1985]. In particular, the limit  $w$  will be the solution corresponding to the Kirchhoff model. Note also that the limit  $\underline{\gamma}_h$  that appears in Eq. 2.9 will still belong to  $R(\underline{\Theta}_h) - \underline{\nabla}(W_h)$ . The results given in [Brezzi and Bathe, 1986] with the discussion below give some insight into the behavior of  $\underline{\gamma}_h$ .

**Remark 3** The operator  $R$  defines the “tying” to be employed between the basis functions used in  $\underline{\Gamma}_h$  and the interpolation functions used in  $W_h$  and  $\underline{\Theta}_h$ .

Now for each element formulation in the family, the following must be chosen:

- A finite element space  $\underline{\Theta}_h$  for the approximation of the rotations;
- A finite element space  $W_h$  for the approximation of the transverse displacement;
- A finite element space  $\underline{\Gamma}_h$  for the approximation of the shear strains; and
- A reduction operator  $R$  which interpolates piecewise smooth function into  $\underline{\Gamma}_h$ .

The choice of element variables are not arbitrary and the following mathematical analysis gives restrictions in the selection of each variables.

The analysis of the above elements greatly depends on the theoretical results for finite element solutions of the response of incompressible media. The solution seeks a “pressure space”  $Q_h$  made of discontinuous finite element functions<sup>1</sup> such that, for all  $\underline{\eta} \in \underline{\Theta}_h$ ,

$$(\text{rot } \underline{\eta}, q_h) = (\text{rot } (R\underline{\eta}), q_h) \quad \forall q_h \in Q_h \quad (2.10)$$

where  $\text{rot } \underline{\eta} \equiv \frac{\partial \eta_2}{\partial x} - \frac{\partial \eta_1}{\partial y}$ , and

$$\text{rot } (\underline{\Gamma}_h) \subseteq Q_h. \quad (2.11)$$

The space  $Q_h$  is never used in the actual computations; however, its existence (with the suitable properties) is crucial in mathematical analysis. Conditions Eqs. 2.10 and 2.11 are related to the so-called “commuting diagram property” of Douglas and Roberts [Douglas, Jr. and Roberts, 1985] that is used in the study of mixed methods for elliptic equations.

To analyze the error between  $\underline{\theta}$  and  $\underline{\theta}_h$  in Eq. 2.8 and Eq. 2.9 (and as a consequence the error between  $w$  and  $w_h$ ), a pair  $\hat{\underline{\theta}}, \hat{w}$  in  $\underline{\Theta}_h \times W_h$ , needs to be built such that  $\|\underline{\theta} - \hat{\underline{\theta}}\|_1$  is optimally small and

$$R\hat{\underline{\theta}} = \underline{\nabla} \hat{w}. \quad (2.12)$$

Condition Eq. 2.12 implies

$$\text{rot } R\hat{\underline{\theta}} = 0 \quad (2.13)$$

which, in turn, using Eqs. 2.10 and 2.11 is equivalent to

$$(\text{rot } \hat{\underline{\theta}}, q_h) = 0 \quad \forall q_h \in Q_h. \quad (2.14)$$

Hence, a possible way of  $\hat{\underline{\theta}}$  construction is as follows. For  $\underline{\theta}$  given in  $(H_0^1(\Omega))^2$  and

---

<sup>1</sup>This space corresponds to the pressure space in incompressible solutions.

satisfying  $\text{rot } \underline{\theta} = 0$ , consider the problem:

Find  $\underline{\beta}, p \in \underline{\Theta} \times L^2(\Omega)$  such that

$$\begin{aligned} a(\underline{\beta}, \underline{\eta}) + (p, \text{rot } \underline{\eta}) &= a(\underline{\theta}, \underline{\eta}) \quad \forall \underline{\eta} \in \underline{\Theta} \\ (q, \text{rot } \underline{\beta}) &= 0 \quad \forall q \in L^2(\Omega) \end{aligned} \quad (2.15)$$

and its approximation,

Find  $\hat{\underline{\theta}}, p_h \in \underline{\Theta}_h \times Q_h$  such that

$$\begin{aligned} a(\hat{\underline{\theta}}, \underline{\eta}) + (p_h, \text{rot } \underline{\eta}) &= a(\underline{\theta}, \underline{\eta}) \quad \forall \underline{\eta} \in \underline{\Theta}_h \\ (q, \text{rot } \hat{\underline{\theta}}) &= 0 \quad \forall q \in Q_h. \end{aligned} \quad (2.16)$$

Note that Eq. 2.15 is a kind of Stokes problem and its solution is given by  $\underline{\beta} = \underline{\theta}, p = 0$ . If the pair  $\underline{\Theta}_h, Q_h$  used in Eq. 2.16 is a suitable finite element discretization for the Stokes problem, then one might expect to have optimal error bounds for  $\hat{\underline{\theta}} - \underline{\theta}$ . However, note that once  $\hat{\underline{\theta}}$  satisfying Eq. 2.13 has been found, the  $\hat{w} \in W$  that uniquely satisfies Eq. 2.12 can be determined. It can be shown that in each case such a  $\hat{w}$  is an element of  $W_h$ .

Condition Eq. 2.10 provides the tying scheme (restriction in the choice of  $R$ ).

Equation 2.10 can be rewritten as,

$$(\text{rot } (R\underline{\eta} - \underline{\eta}), q_h) = 0 \quad \forall q_h \in Q_h. \quad (2.17)$$

Now, expressing the above equation in integral form and applying Green's theorem twice,

$$\int_{\partial K} (R\underline{\eta} - \underline{\eta}) \cdot \underline{\tau} q_h ds - \int_K (R\underline{\eta} - \underline{\eta}) \cdot \text{rot } q_h dA = 0 \quad \forall q_h \in Q_h \quad (2.18)$$

which can be further expressed in two equations:

$$\int_{\partial K} (R\underline{\eta} - \underline{\eta}) \cdot \underline{\tau} q_h ds = 0 \quad \forall q_h \in Q_h \quad (2.19)$$

and

$$\int_K (R\underline{\eta} - \underline{\eta}) \cdot \text{rot } q_h dA = 0 \quad \forall q_h \in Q_h \quad (2.20)$$

where  $\underline{\tau}$  is the tangential unit vector to each edge of each element. Equations. 2.19 and 2.20 are the tying scheme used to relate the directly interpolated strains and the assumed strains.

## 2.2 The Elements

The MITC plate element formulations consist of the choices of the spaces  $\underline{\mathcal{Q}}_h$ ,  $W_h$ ,  $\underline{\Gamma}_h$  and the tying used between the interpolations in  $\underline{\Gamma}_h$  and the transverse shear strain components as evaluated from  $\underline{\mathcal{Q}}_h$  and  $W_h$ .

The choices for each element considered are presented below. The elements use the Cartesian coordinates, thus consider the uniform rectangular and triangular decompositions. The same interpolations are used in the natural coordinates for the covariant strain components in the general elements [Bathe *et al.*, 1989a; Bathe and Dvorkin, 1985; Bathe and Dvorkin, 1986; Dvorkin and Bathe, 1984]. Figure 2-1 illustrates the nodal point variables employed for each MITC family of plate elements.

### 2.2.1 The MITC4 Element

For the 4-node element,

$$\underline{\mathcal{Q}}_h = \{ \underline{\eta} \mid \underline{\eta} \in (H_0^1(\Omega))^2, \underline{\eta}|_K \in (Q_1)^2 \quad \forall K \} \quad (2.21)$$

$$W_h = \{ \zeta \mid \zeta \in H_0^1(\Omega), \zeta|_K \in Q_1 \quad \forall K \} \quad (2.22)$$

are used where  $Q_1$  is the set of polynomials of degree  $\leq 1$  in each variable and  $K$  is the current element in the discretization [Bathe and Dvorkin, 1985; Dvorkin and Bathe, 1984]. The space  $\underline{\Gamma}_h$  is given by

$$\underline{\Gamma}_h = \{\underline{\delta} \mid \underline{\delta}|_K \in TR(K) \quad \forall K, \underline{\delta} \cdot \underline{\tau} \text{ continuous at the interelement boundaries}\} \quad (2.23)$$

and

$$TR(K) = \{\underline{\delta} \mid \delta_1 = a_1 + b_1 y, \delta_2 = a_2 + b_2 x\}. \quad (2.24)$$

The space  $TR(K)$  is a sort of “rotated Raviart-Thomas” space of order zero [Raviart and Thomas, 1975].

It can be shown that Eqs. 2.10 and 2.11 hold if we take for the MITC4 element,

$$Q_h = \{q \mid q|_K \in P_0 \quad \forall K\} \quad (2.25)$$

where  $P_k$  denotes the set of polynomials of total degree  $\leq k$ . Hence,  $Q_h$  has a local dimension of 1 in the MITC4 case. Note that the relation given in Eq. 2.10 is satisfied because of the specific operator  $R$  used for the element.

Next, the reduction operator  $R$  is introduced by describing its action on the current element: for  $\underline{\eta}$  smooth in  $K$ ,  $R\underline{\eta}|_K$  is the unique element in  $TR(K)$  that satisfies the tying scheme in Eq. 2.18. Equation 2.20 is automatically satisfied and Eq. 2.19 has the form

$$\int_e (\underline{\eta} - R\underline{\eta}) \cdot \underline{\tau} \, ds = 0 \quad \text{for all edges } e \text{ of } K. \quad (2.26)$$

Note that if  $\underline{\eta} \in (Q_1)^2$  then Eq. 2.26 holds if and only if  $\underline{\eta} \cdot \underline{\tau} = R(\underline{\eta}) \cdot \underline{\tau}$  at the midpoints of each edge.

In refs. [Bathe and Brezzi, 1985; Bathe and Brezzi, 1987; Brezzi *et al.*, 1989], the error estimate for the MITC4 element is given by,

$$\|\underline{\theta} - \underline{\theta}_h\|_1 + \|\underline{\nabla} w - \underline{\nabla} w_h\|_0 \leq c h (\|\underline{\theta}\|_2 + \|\underline{\gamma}\|_0). \quad (2.27)$$

Hence, the MITC4 element shows a linear convergence behavior. For the MITC4 element the pair  $\underline{Q}_h, Q_h$  is the classical bilinear velocities-constant pressure element. Hence the result in Eq. 2.27 corresponds to the behavior of the  $Q_1 - P_0$  elements, and an excellent predictive capability of the MITC4 element can be anticipated.

### 2.2.2 The MITC7 Element

For the 7-node triangular element,

$$\underline{Q}_h = \{\underline{\eta} \mid \underline{\eta} \in (H_0^1(\Omega))^2, \underline{\eta}|_T \in (S_7(T))^2 \quad \forall T\} \quad (2.28)$$

$$W_h = \{\zeta \mid \zeta \in H_0^1(\Omega), \zeta|_T \in P_2 \quad \forall T\} \quad (2.29)$$

are used where  $T$  is the triangular element in the discretization,  $P_2$  is the space of complete second-order polynomials (corresponding to a 6-node element), and  $S_7$  is expressed as

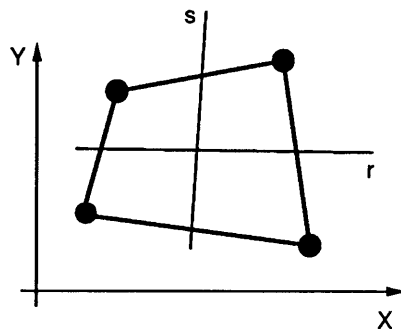
$$S_7(T) = \{\varphi \mid \varphi \in P_3, \varphi|_e \in P_2 \text{ on each edge } e \text{ of } T\} \quad (2.30)$$

where  $P_3$  is the space of complete third-order polynomials [Bathe *et al.*, 1989a; Brezzi *et al.*, 1989].

Clearly  $S_7$  is a finite dimensional linear space of dimension 7. It can also be characterized as  $S_7 = P_2 \oplus \{\lambda_1 \lambda_2 \lambda_3\}$  where  $\lambda_1 \lambda_2 \lambda_3$  is the cubic bubble in  $T$ . As the degrees of freedom in  $S_7(T)$ , the values can be chosen at the vertices, the midpoints of the edges, and the barycenter of  $T$ . Also, in each triangle  $T$ ,

$$\begin{aligned} TR_1(T) = \{\underline{\delta} \mid & \delta_1 = P_1 + y(ax + by); \\ & \delta_2 = P_1 - x(ax + by)\}. \end{aligned} \quad (2.31)$$

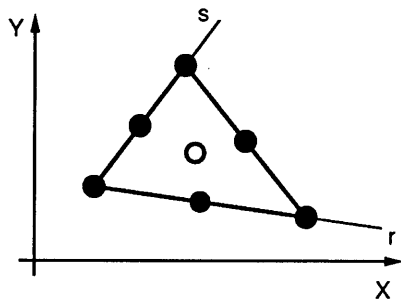
The space  $TR_1(T)$  is a kind of “rotated Raviart-Thomas” space of order one [Raviart and Thomas, 1975].



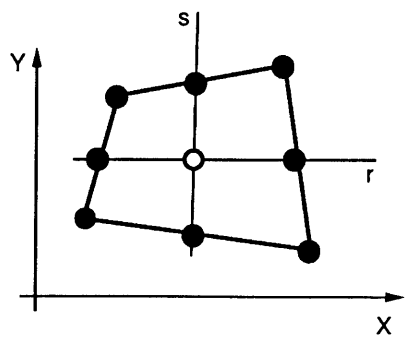
(a) MITC4 element

Nodal Point Variables:

- rotations and transverse displacement
- rotations only



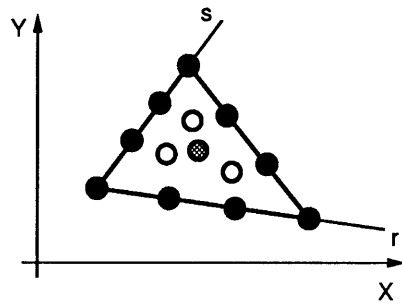
(b) MITC7 element



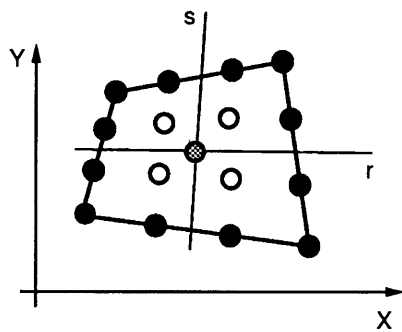
(c) MITC9 element

Figure 2-1: Nodal point variables for each of the MITC elements.





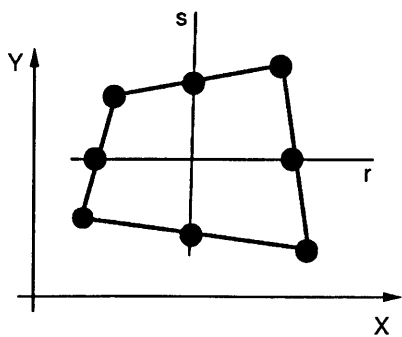
(d) MITC12 element



(e) MITC16 element

Nodal Point Variables:

- rotations and transverse displacement
- rotations only
- ⊗ transverse displacement only



(f) MITC8 element

Figure 2-1 Continued.

The space  $\underline{\Gamma}_h$  is given by

$$\begin{aligned} \underline{\Gamma}_h = \{ \underline{\delta} \mid \underline{\delta}|_T \in TR_1(T), \forall T, \quad \underline{\delta} \cdot \underline{\tau} \text{ continuous at the interelement boundaries,} \\ \underline{\delta} \cdot \underline{\tau} = 0 \text{ on } \partial\Omega \}. \end{aligned} \quad (2.32)$$

It can be shown that Eqs. 2.10 and 2.11 hold if we take for the MITC7 element,

$$Q_h = \{ q \mid q|_T \in P_1 \quad \forall T \}. \quad (2.33)$$

Here,  $Q_h$  has a local dimension of 3 in the MITC7 case. Note that the relation Eq. 2.10 is satisfied because of the specific operator  $R$  used for the element.

Next, the reduction operator  $R$  is introduced. Its action on the current element is given as follows: for  $\underline{\eta}$  smooth in  $T$ ,  $R\underline{\eta}$  in  $T$  is the unique element in  $TR_1(T)$  that satisfies the tying scheme in Eqs. 2.19 and 2.20.

$$\int_e (\underline{\eta} - R\underline{\eta}) \cdot \underline{\tau} p_1(s) ds = \underline{0} \quad \forall e \text{ edge of } T, \quad \forall p_1(s) \in P_1(e) \quad (2.34)$$

$$\int_T (\underline{\eta} - R\underline{\eta}) dx dy = 0. \quad (2.35)$$

Note that if  $\underline{\eta} \in (S_7)^2$  then Eq. 2.34 holds if and only if  $\underline{\eta} \cdot \underline{\tau} = (R\underline{\eta}) \cdot \underline{\tau}$  at the two Gauss points of each edge. Notice that Eqs. 2.34 and 2.35 characterize  $R\underline{\eta}$  in  $T$  in a unique way. It is also clear that if  $\underline{\eta}$  is continuous in  $\Omega$ , then the  $R\underline{\eta}$  constructed element by element through Eqs. 2.34 and 2.35 actually belongs to  $\underline{\Gamma}_h$  (because Eq. 2.34 ensures the continuity of  $(R\underline{\eta}) \cdot \underline{\tau}$  at the interelement boundaries).

The above integral tying scheme requires a numerical integration over the element. Instead of the integral-tying given by Eq. 2.35, simply the mean of the values at points  $TA$ ,  $TB$  and  $TC$  of the element can also be used (see Fig. 2-2); hence Eq. 2.35 is replaced by

$$\frac{1}{3}(\eta_1|_{TA} + \eta_1|_{TB} + \eta_1|_{TC}) = R\eta_1|_A \quad (2.36)$$

$$\frac{1}{3}(\eta_2|_{TA} + \eta_2|_{TB} + \eta_2|_{TC}) = R\eta_2|_A$$

where point  $A$  corresponds to the barycenter of the element and the points  $TA$ ,  $TB$ , and  $TC$  correspond to the Gauss points of 3-point integration in the triangle [Bathe *et al.*, 1989a].

The element using Eq. 2.35 is referred to as the MITC7<sup>I</sup> element, and the element using Eq. 2.36 the MITC7 element.

In refs. [Bathe and Brezzi, 1985; Bathe and Brezzi, 1987; Brezzi *et al.*, 1989], the error estimate for the MITC7 element is given by,

$$\|\underline{\theta} - \underline{\theta}_h\|_1 + \|\underline{\nabla}w - \underline{\nabla}w_h\|_0 \leq c h^2 (\|\underline{\theta}\|_3 + \|\underline{\gamma}\|_1). \quad (2.37)$$

Hence the MITC7 element shows quadratic convergence. For the MITC7 element the pair  $\underline{Q}_h$ ,  $Q_h$  is the Crouzeix-Raviart element with the velocities given by quadratic plus cubic bubble variations and the pressure given by linear variation. Hence the result in Eq. 2.37 corresponds to the behavior of the  $Q_2 - P_1$  elements [Sussman and Bathe, 1987], and an excellent predictive capability of the MITC7 element can be anticipated.

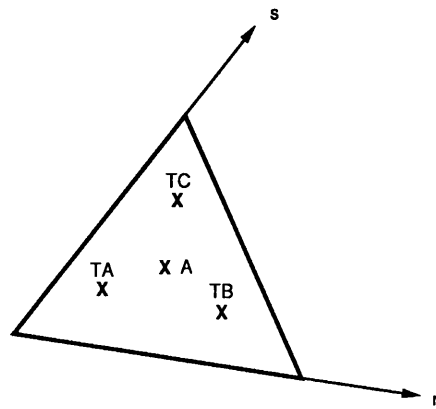
### 2.2.3 The MITC9 Element

For the 9-node element,

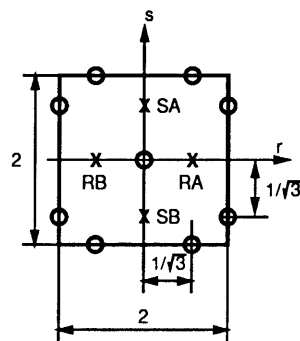
$$\underline{Q}_h = \{\underline{\eta} \mid \underline{\eta} \in (H_0^1(\Omega))^2, \underline{\eta}|_K \in (Q_2)^2 \quad \forall K\} \quad (2.38)$$

$$W_h = \{\zeta \mid \zeta \in H_0^1(\Omega), \zeta|_K \in Q_2^r \quad \forall K\} \quad (2.39)$$

are used where  $Q_2^r$  is the usual serendipity reduction of  $Q_2$  (the space of polynomials of degree  $\leq 2$  in each variable corresponding to a 9-node element) [Bathe and Brezzi, 1987;



(a) Tying for MITC7 element



(b) Tying for MITC9 element

Figure 2-2: Gauss points used for tying of covariant shear strain components.

Bathe *et al.*, 1989a; Brezzi *et al.*, 1989]. The space  $\underline{\Gamma}_h$  is given by

$$\underline{\Gamma}_h = \{\underline{\delta} \mid \underline{\delta}|_K \in G_1(K) \quad \forall K, \quad \underline{\delta} \cdot \underline{\tau} \text{ continuous at the interelement boundaries}\} \quad (2.40)$$

where

$$G_1(K) = \{\underline{\delta} \mid \begin{aligned} \delta_1 &= Q_1 + ay^2; \\ \delta_2 &= Q_1 + bx^2. \end{aligned}\}. \quad (2.41)$$

The space  $G_1$  is some kind of rotated Brezzi-Douglas-Fortin-Marini space [Brezzi *et al.*, 1987].

Note that if  $\zeta \in Q_2^r$  then  $\underline{\nabla}\zeta \in G_1$ . Therefore,  $W_h$  has been discretized with the interpolations of the 8-node element instead of the 9-node element.

It can be shown that Eqs. 2.10 and 2.11 hold if we take for the MITC9 element,

$$Q_h = \{q \mid q|_K \in P_1 \quad \forall K\}. \quad (2.42)$$

Here,  $Q_h$  has a local dimension of 3 in the MITC9 case. Note that the relation Eq. 2.10 is satisfied because of the specific operator  $R$  used for the element.

Next, the reduction operator  $R$  is introduced. Its action on the current element is given as follows: for  $\underline{\eta}$  smooth in  $K$ ,  $R\underline{\eta}|_K$  is the unique element in  $G$  that satisfies the tying scheme in Eqs. 2.19 and 2.20.

$$\int_e (\underline{\eta} - R\underline{\eta}) \cdot \underline{\tau} p_1(s) ds = 0 \quad \forall e \text{ edge of } K, \quad (2.43)$$

$\forall p_1(s)$  polynomial of degree  $\leq 1$  on  $e$

$$\int_K (\underline{\eta} - R\underline{\eta}) dx dy = \underline{0}. \quad (2.44)$$

Note that if  $\underline{\eta} \in (Q_2)^2$  then Eq. 2.43 holds if and only if  $\underline{\eta} \cdot \underline{\tau} = (R\underline{\eta}) \cdot \underline{\tau}$  at the two Gauss points of each edge.

As in the MITC7 element, instead of the integral-tying given by Eq. 2.44, the mean of the values at points  $RA$ ,  $RB$  and  $SA$ ,  $SB$  respectively can be used (see Fig. 2-2). Hence Eq. 2.44 is replaced by

$$\begin{aligned}\frac{1}{2}(\eta_1|_{RA} + \eta_1|_{RB}) &= R\eta_1|_A \\ \frac{1}{2}(\eta_2|_{SA} + \eta_2|_{SB}) &= R\eta_2|_A\end{aligned}\tag{2.45}$$

where  $A$  corresponds to the center point of the element and  $RA$ ,  $RB$ , and  $SA$ ,  $SB$  correspond to the Gauss points along the  $x$  and  $y$  axes, respectively [Bathe *et al.*, 1989a].

The element using Eq. 2.44 is called the MITC9<sup>I</sup> element, and the element using Eq. 2.45, the MITC9 element. These elements yield identical results when they are of rectangular shape [Bathe *et al.*, 1989a]. (See Appendix A.1 for proof.) The point tying scheme used in the MITC9 element can be interpreted as a kind of reduced integration of integral tying constraint of Eq. 2.44. Additional discussion on the integral tying scheme for the general 9-node shell element is given in Sec. 3.4.

In refs. [Bathe and Brezzi, 1985; Bathe and Brezzi, 1987; Brezzi *et al.*, 1989], the error estimate for the MITC9 element is given by,

$$\|\underline{\varrho} - \underline{\varrho}_h\|_1 + \|\underline{\nabla}w - \underline{\nabla}w_h\|_0 \leq c h^2 (\|\underline{\varrho}\|_3 + \|\underline{\gamma}\|_1).\tag{2.46}$$

Hence, the MITC9 element show quadratic convergence. For the case of the MITC9 element the pair  $\underline{\varrho}_h$ ,  $Q_h$  is the biquadratic velocities and linear pressure element. Thus, the result in Eq. 2.46 corresponds to the behavior of the  $Q_2 - P_1$  elements [Sussman and Bathe, 1987], and excellent predictive capability of the MITC9 element can be expected.

### 2.2.4 The MITC12 Element

The 12-node triangular element is an extension of the MITC7<sup>I</sup> element. Here,

$$\underline{\varrho}_h = \{\underline{\eta} \mid \underline{\eta} \in (H_0^1(\Omega))^2, \underline{\eta}|_T \in (S_{12}(T))^2 \quad \forall T\}\tag{2.47}$$

$$W_h = \{\zeta \mid \zeta \in H_0^1(\Omega), \zeta|_T \in P_3 \quad \forall T\} \quad (2.48)$$

are used where  $T$  is the triangular element in the discretization and  $S_{12}$  is

$$S_{12}(T) = \{\varphi \mid \varphi \in P_4, \varphi|_e \in P_3 \text{ on each edge } e \text{ of } T\} \quad (2.49)$$

where  $P_4$  is the space of complete fourth-order polynomials. The space  $\underline{\Gamma}_h$  is given by

$$\underline{\Gamma}_h = \{\underline{\delta} \mid \underline{\delta}|_T \in TR_2(T) \quad \forall T, \underline{\delta} \cdot \underline{\tau} \text{ continuous at the interelement boundaries}\} \quad (2.50)$$

where

$$TR_2(T) = \{\underline{\delta} \mid \begin{aligned} \delta_1 &= P_2 + y(ax^2 + bxy + cy^2); \\ \delta_2 &= P_2 - x(ax^2 + bxy + cy^2). \end{aligned}\}. \quad (2.51)$$

The space  $TR_2(T)$  is a kind of “rotated Raviart-Thomas” space of order two [Raviart and Thomas, 1975]. The reduction operator  $R$  is given by

$$\int_e (\underline{\eta} - R\underline{\eta}) \cdot \underline{\tau} p_2(s) ds = 0 \quad \forall e \text{ edge of } T, \quad \forall p_2(s) \in P_2(e) \quad (2.52)$$

$$\int_T (\underline{\eta} - R\underline{\eta}) \cdot p_1 dx dy = 0 \quad \forall p_1 \in (P_1(T))^2. \quad (2.53)$$

So far, only the integral tying of Eq. 2.53 has been used for the element; therefore, the element is referred to as the MITC12<sup>I</sup> element.

### 2.2.5 The MITC16 Element

The 16-node element is an extension of the MITC9<sup>I</sup> element. Here,

$$\underline{\Theta}_h = \{\underline{\eta} \mid \underline{\eta} \in (H_0^1(\Omega))^2, \underline{\eta}|_K \in (Q_3)^2 \quad \forall K\} \quad (2.54)$$

$$W_h = \{\zeta \mid \zeta \in H_0^1(\Omega), \zeta|_K \in Q_3 \cap P_4 \quad \forall K\} \quad (2.55)$$

are used where  $Q_3$  is the space of polynomials of degree  $\leq 3$  in each variable corresponding to a 16-node element. The space  $\underline{\Gamma}_h$  is given by

$$\underline{\Gamma}_h = \{\underline{\delta} \mid \underline{\delta}|_K \in G_2(K) \quad \forall K, \quad \underline{\delta} \cdot \underline{\tau} \text{ continuous at the interelement boundaries}\} \quad (2.56)$$

where

$$G_2(K) = \{\underline{\delta} \mid \begin{aligned} \delta_1 &= P_2 + a_1 x^2 y + b_1 x y^2 + c_1 y^3; \\ \delta_2 &= P_2 + a_2 x^2 y + b_2 x y^2 + c_2 x^3 \end{aligned}\}. \quad (2.57)$$

The space  $G_2$  is some kind of rotated Brezzi-Douglas-Fortin-Marini space [Brezzi *et al.*, 1987]. The reduction operator  $R$  is given by

$$\int_e (\underline{\eta} - R\underline{\eta}) \cdot \underline{\tau} p_2(s) ds = 0 \quad \forall e \text{ edge of } K, \quad \forall p_2(s) \in P_2(e) \quad (2.58)$$

$$\int_K (\underline{\eta} - R\underline{\eta}) \cdot p_1 dx dy = \underline{0} \quad \forall p_1 \in (P_1(K))^2. \quad (2.59)$$

As in the MITC12<sup>I</sup> element, only the integral tying of Eq. 2.59 has been used; therefore, the element is referred to as the MITC16<sup>I</sup> element.

## 2.2.6 The MITC8 Element

The MITC8 element is given here for comparison purposes only. Since the element is constructed directly as a general shell element, the interpolation of the covariant shear strain tensor components and the contravariant base vectors are used in the formulation. The MITC8 element in a flat plate condition, as a special case, is described below. For the 8-node element, the following space is used [Bathe and Dvorkin, 1986]:

$$\underline{\Theta}_h = \{\underline{\eta} \mid \underline{\eta} \in (H_0^1(\Omega))^2, \underline{\eta}|_K \in (Q_2^r)^2 \quad \forall K\} \quad (2.60)$$

$$W_h = \{\zeta \mid \zeta \in H_0^1(\Omega), \zeta|_K \in Q_2^r \quad \forall K\}. \quad (2.61)$$



The space  $\underline{\Gamma}_h$  is given by

$$\underline{\Gamma}_h = \{\underline{\delta} \mid \underline{\delta}|_K \in F(K) \quad \forall K, \underline{\delta} \cdot \underline{\tau} \text{ continuous at the interelement boundaries}\} \quad (2.62)$$

where  $F$  is the following space

$$F(K) = \{\underline{\delta} \mid \delta_1, \delta_2 = Q_1 \oplus \{x^2y^2\}\}. \quad (2.63)$$

The tying is achieved by point-tying along the edges and in the interior as described in [Bathe and Dvorkin, 1986].

## 2.3 Reliability of the Elements

The objective of this section is to present some numerical results of plate analyses obtained using the MITC plate elements. These results demonstrate the excellent predictive capabilities of the elements.

Also some comparisons with the results obtained with the MITC4 [Bathe and Dvorkin, 1985] and MITC8 [Bathe and Dvorkin, 1986] elements are presented. Note that all the MITC element stiffness matrices are evaluated using “full” numerical integration and that these elements (and the MITC4 and MITC8 elements) do not contain any spurious zero energy modes.

Mathematical analyses are presented in [Bathe and Brezzi, 1985; Bathe and Brezzi, 1987; Brezzi *et al.*, 1989] for the MITC4, MITC7<sup>I</sup>, MITC9<sup>I</sup>, MITC12<sup>I</sup> and MITC16<sup>I</sup> elements that prove the convergence of discretization based on these elements to the analytical plate theory solutions.

Theoretical analyses do not consider the MITC8, MITC7 and MITC9 elements. However, the MITC7 and MITC9 elements constructions are very close to those using the integral tying, and all three elements pass the patch test and have shown excellent convergence characteristics in numerical experiments [Bathe *et al.*, 1989a; Bathe *et al.*, 1989b].

### 2.3.1 Patch Test

Figure 2-3 shows the patch of elements considered. For the patch test, only the minimum number of degrees of freedom are deleted to eliminate the physical rigid body modes [Dvorkin and Bathe, 1984]. Recall that the MITC4 and MITC8 elements passed the patch test.

The MITC7<sup>I</sup>, MITC7, MITC9, MITC12<sup>I</sup> and MITC16<sup>I</sup> elements pass the patch test as well. It is interesting to note that the MITC9 element passes the patch test, whereas the MITC9<sup>I</sup> element does not; however, the degree of failure is not severe. Figure 2-4 shows the stress distributions obtained when the patch of MITC9<sup>I</sup> elements is subjected to a constant bending moment. The predicted stresses do not vary from the analytical solution by a large amount; hence, it practically passes the patch test.

Although this simple patch test does not display the complete convergence characteristics of an element, the test is a condition for a reliable finite element and it is an indication of the element's sensitivity to geometric distortions [Bathe and Dvorkin, 1986].

### 2.3.2 Analysis of a Square Plate

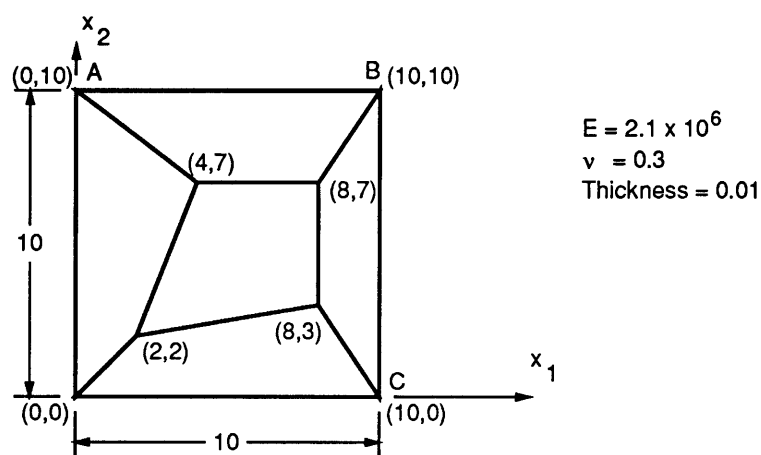
Figure 2-5 shows the plate problems considered and the meshes used in the analyses. Table 2-1 summarizes the displacement results obtained, including those using the MITC4, MITC8 and 16-node cubic shell (referred to as DISP16 element) elements.

Note that in these analyses, the finite element imposed boundary conditions correspond to the "soft" conditions for the problem considered [Hägglad and Bathe, 1990].

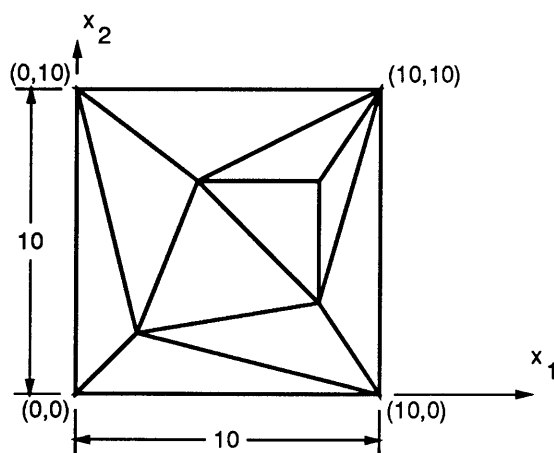
The meshes distort-1 and distort-2 have of course only been included in the tests in order to identify the distortion sensitivity of the elements [Bathe and Dvorkin, 1986].

As shown in Table 2-1, the MITC of plate elements performs very well. Notice that 9-node MITC9 element performs much better than 16-node cubic shell element.

Figure 2-6 shows the displacement convergence solutions obtained with the new MITC elements. Here, the problem of a clamped square plate subjected to distributed pressure

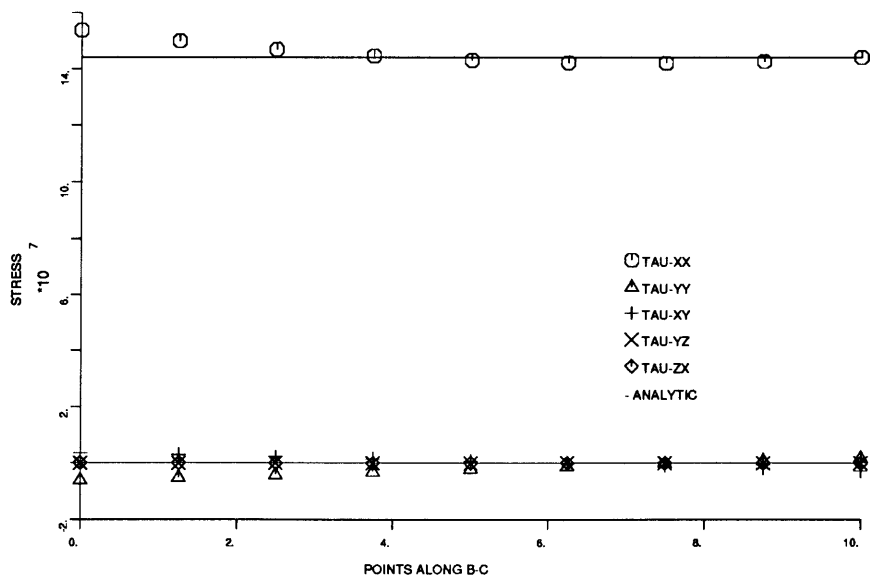
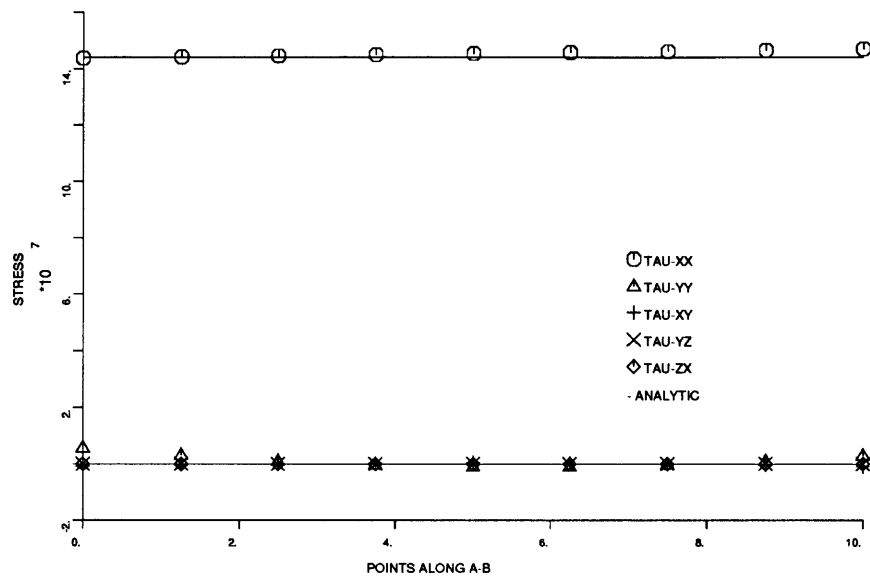


(a) Patch test mesh layout for rectangular elements



(b) Patch test mesh layout for triangular elements

Figure 2-3: Patch of the elements used in a patch test.

Figure 2-4: Stress distribution in the patch using the MITC9<sup>I</sup> elements.

was selected because the solution is smooth. Hence, the finite element solution for the center displacement, for a small thickness to length ratio, (e.g.  $h/L = 1/1000$ ) is comparable to the Kirchhoff plate theory solution.

For the quadrilateral elements, regular meshes have been used with  $N \times N$  elements for a quarter of the plate. The regular triangular element meshes were then obtained by representing each square element by two triangular elements, the subdividing line of the corner element bisecting the corner of the quarter plate. Figure 2-6 shows the excellent predictive behavior of the elements.

Figure 2-7 shows displacement and stress distributions calculated using the MITC7 and MITC9 elements compared to the analytical solution [Timoshenko and Woinowsky-Krieger, 1959].

The stresses have been calculated at the nodal points from the element displacements, and thus, stress jumps can be observed. However, the stress jumps are small for the fine mesh results and are largely confined to the area of the stress singularity (the center of the plate when subjected to the concentrated load).

Next, prediction of edge shear stress in a simply-supported square plate subjected to uniformly distributed pressure is studied. The analysis of a simply-supported square plate is suitable to study the capability of the elements to predict transverse shear stresses. In this analysis, the boundary layer of the transverse shear stresses near a corner was considered [Hägglad and Bathe, 1990].

To obtain a reference solution the 16-node displacement-based element was used (in undistorted form), and two graded meshes were used for a quarter of the plate. The  $10 \times 10$  mesh is shown in Fig. 2-8, and the  $20 \times 20$  mesh was obtained by subdividing each element of the  $10 \times 10$  mesh into four new elements. The two solutions obtained with these meshes show negligible differences.

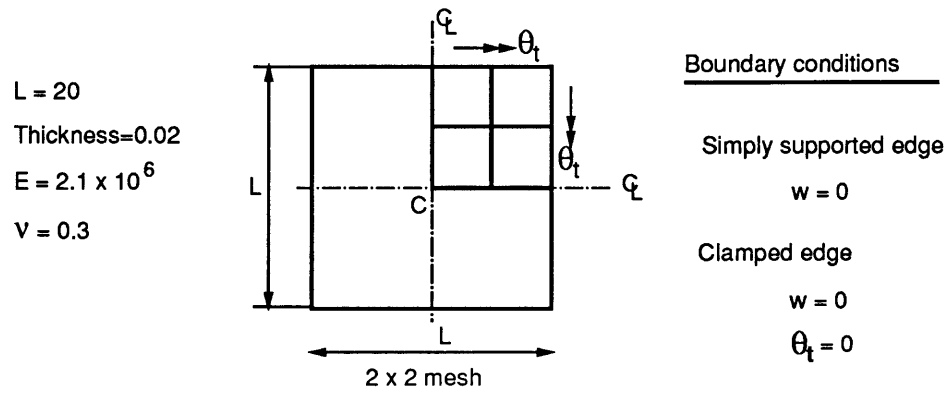
Figure 2-9 shows the shear stress predictions obtained using lower-order MITC elements, i.e., the MITC4, MITC8 and MITC9 elements, in comparison to the reference solution. Note that, at a sufficient distance from the corner, the reference solution cor-

responds to the Kirchhoff analytical solution.

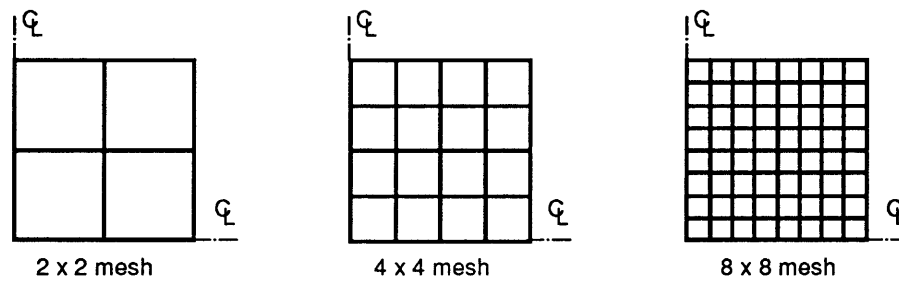
The stresses shown in Fig. 2-9 have been directly calculated at the corner nodes of the elements using the  $\underline{\Gamma}_h$  spaces. Good convergence to the reference solution is observed, and the MITC9 element solutions shown correspond to the MITC9<sup>I</sup> element solutions (since only rectangular elements have been used). Note also that the grading of the mesh in this analysis has an important effect.

Regarding the shear stress predictions, recall that the mathematical theory does not give the rate of convergence of these stress components. However, a particularly good convergence behavior for the MITC9<sup>I</sup> element is expected because this element corresponds to the  $Q_2 - P_1$  element (the 9/3 element) used in incompressible analysis [Brezzi and Bathe, 1986; Brezzi *et al.*, 1989] (see Fig. 2-9). (In general, the MITC elements are expected to be as effective in shear stress predictions as their counterparts are in predicting the pressure in incompressible analysis.)

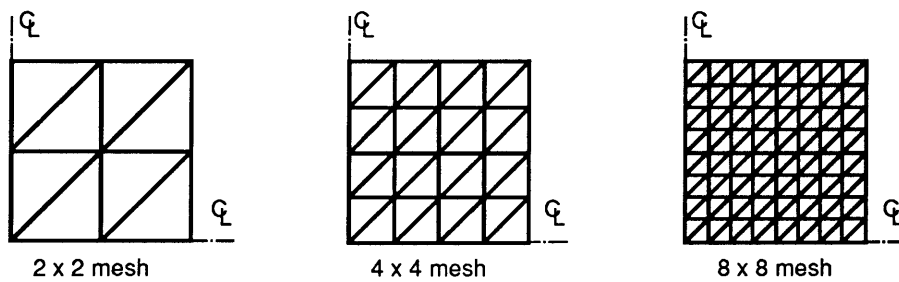
Considering these results, note that the predictive capabilities of the MITC elements are excellent, and that there is little difference between the results of the MITC7<sup>I</sup> and MITC7 elements, and the MITC9<sup>I</sup> and MITC9 elements, respectively.



(a) Physical model

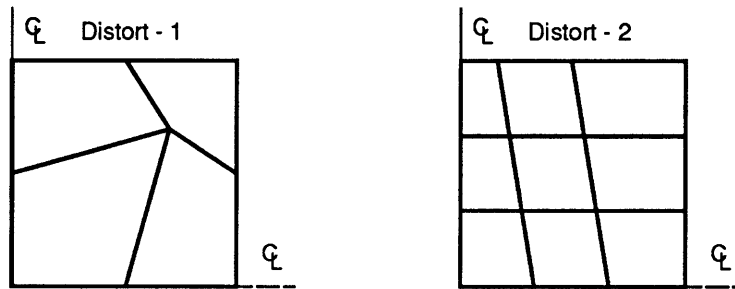


(b) Rectangular mesh layout

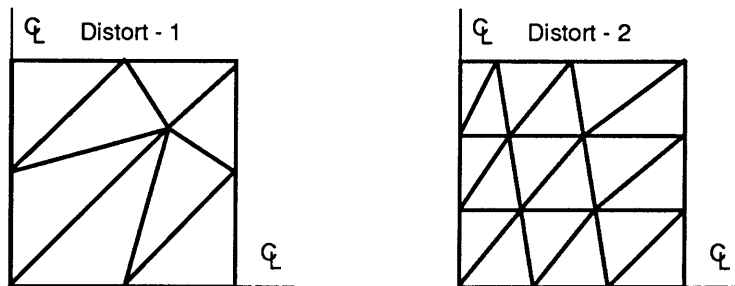


(c) Triangular mesh layout

Figure 2-5: Analysis of a square plate.



(d) Distorted mesh layout for rectangular elements



(e) Distorted mesh layout for triangular elements

Figure 2-5 Continued.



Table 2-1: Analysis of a square plate.

- (a) Response for various plate thicknesses for concentrated load at the center of the plate,  $2 \times 2$  mesh.
- The analytical solution used as reference is the Kirchhoff plate theory solution of Ref. [Timoshenko and Woinowsky-Krieger, 1959].

Element	Thickness	$\alpha$ : simply supported edge	$\alpha$ : clamped edge
MITC4	0.2	0.996	0.869
	0.02	0.995	0.867
	0.002	0.995	0.867
MITC8	0.2	1.000	1.004
	0.02	0.998	1.001
	0.002	0.998	1.001
MITC7 <sup>I</sup>	0.2	0.982	0.918
	0.02	0.980	0.907
	0.002	0.980	0.907
MITC9 <sup>I</sup>	0.2	1.000	1.010
	0.02	0.998	1.006
	0.002	0.998	1.006
MITC7	0.2	0.982	0.929
	0.02	0.979	0.918
	0.002	0.979	0.918
MITC9	0.2	1.000	1.010
	0.02	0.998	1.006
	0.002	0.998	1.006
MITC12 <sup>I</sup>	0.2	0.999	0.998
	0.02	0.996	0.994
	0.002	0.996	0.994
MITC12	0.2	1.003	1.010
	0.02	1.000	1.006
	0.002	1.000	1.006
MITC16 <sup>I</sup>	0.2	1.009	1.017
	0.02	1.006	1.014
	0.002	1.006	1.014

$$\frac{w_{\text{fem}}}{w_{\text{analyt.}}} \quad \text{at center of the plate}$$

Table 2-1 Continued.

(b) Response for various mesh layouts. (thickness = 0.02)

Element	Mesh	Concentrated Load		Uniform Pressure	
		$\alpha$ : simply supported edge	$\alpha$ : clamped edge	$\alpha$ : simply supported edge	$\alpha$ : clamped edge
MITC4	2 × 2	0.995	0.867	0.981	0.963
	4 × 4	0.995	0.965	0.996	0.993
	8 × 8	0.998	0.992	0.999	1.001
MITC8	2 × 2	0.998	1.001	1.000	1.006
	4 × 4	1.000	1.001	1.001	1.005
	8 × 8	1.000	1.002	1.001	1.004
MITC7 <sup>I</sup>	2 × 2	0.980	0.907	1.003	0.965
	4 × 4	0.994	0.985	1.000	1.001
	8 × 8	0.999	0.999	1.000	1.004
MITC9 <sup>I</sup>	2 × 2	0.998	1.006	0.999	1.025
	4 × 4	1.000	1.001	1.000	1.005
	8 × 8	1.000	1.002	1.000	1.004
MITC7	2 × 2	0.979	0.918	1.003	0.977
	4 × 4	0.994	0.987	1.001	1.003
	8 × 8	0.999	0.999	1.000	1.004
MITC9	2 × 2	0.998	1.006	0.999	1.025
	4 × 4	1.000	1.001	1.000	1.005
	8 × 8	1.000	1.002	1.000	1.004
MITC12 <sup>I</sup>	2 × 2	0.996	0.994	1.000	1.005
	4 × 4	0.999	1.000	1.000	1.004
	8 × 8	1.000	1.002	1.000	1.004
MITC12	2 × 2	1.000	1.006	0.999	1.004
	4 × 4	1.000	1.003	1.000	1.004
	8 × 8	1.000	1.002	1.000	1.004
MITC16 <sup>I</sup>	2 × 2	1.006	1.014	1.000	1.003
	4 × 4	1.002	1.005	1.000	1.004
	8 × 8	1.000	1.003	1.000	1.004
DISP16	1 × 1	0.955	0.946	1.016	1.052
	2 × 2	0.989	0.979	1.001	1.004
	3 × 3	0.995	0.992	1.001	1.004

$$\alpha = \frac{w^{\text{fem}}}{w^{\text{analyt.}}} \quad \text{at center of the plate}$$

Table 2-1 Continued.

(c) Response for distorted mesh layouts under concentrated load at the center of the plate (thickness = 0.02).

Element	Mesh	$\alpha$ : simply supported edge	$\alpha$ : clamped edge
MITC4	distort-1	0.986	0.807
	distort-2	0.984	0.922
MITC8	distort-1	1.002	0.975
	distort-2	0.999	0.994
MITC7 <sup>I</sup>	distort-1	0.966	0.827
	distort-2	0.991	0.975
MITC9 <sup>I</sup>	distort-1	1.011	1.025
	distort-2	0.999	1.001
MITC7	distort-1	0.965	0.844
	distort-2	0.991	0.978
MITC9	distort-1	1.002	1.015
	distort-2	0.999	1.001
MITC12 <sup>I</sup>	distort-1	0.992	0.988
	distort-2	0.999	0.999
MITC12	distort-1	0.997	1.004
	distort-2	1.001	1.004
MITC16 <sup>I</sup>	distort-1	1.006	1.014
	distort-2	1.003	1.008
DISP16	distort-1	0.975	0.918
	distort-2	0.995	0.990

$$\alpha = \frac{w_{\text{fem}}}{w_{\text{analyt.}}} \quad \text{at center of the plate.}$$

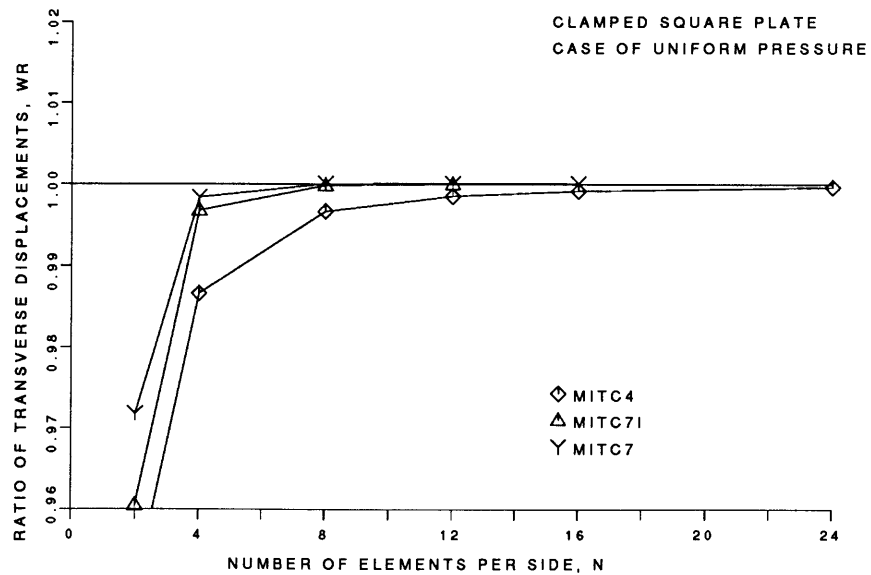
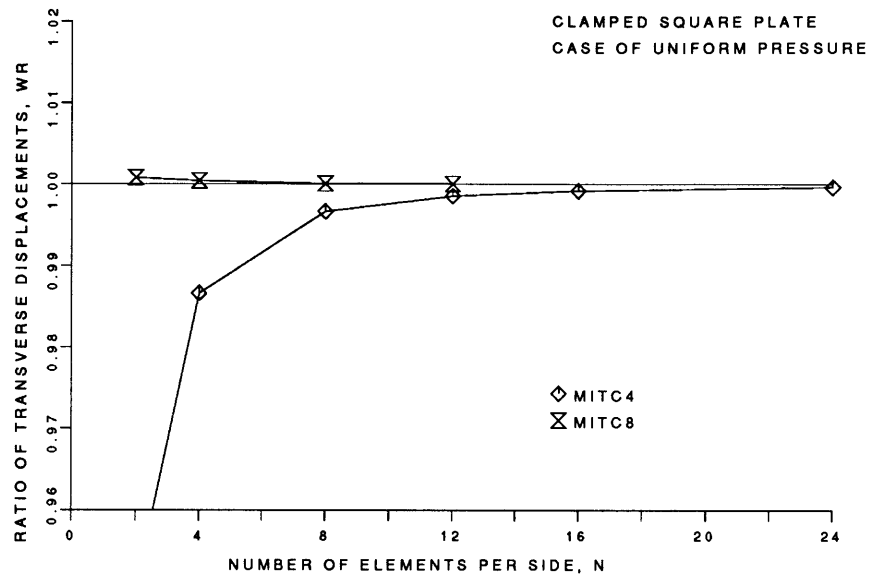


Figure 2-6: Convergence of center displacement of a clamped square plate, compared to the Kirchhoff plate theory solution, thickness/length = 1/1000, WR = ratio of finite element solution to analytical result.

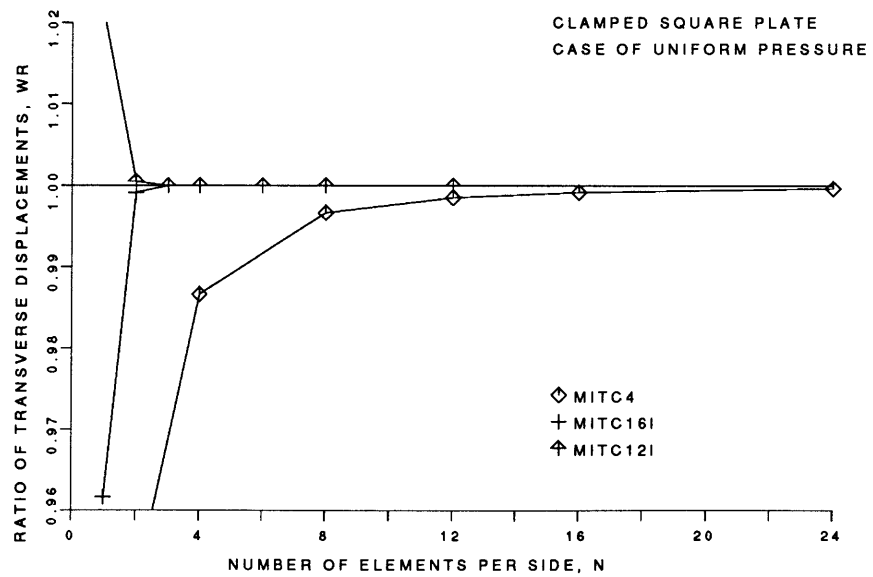
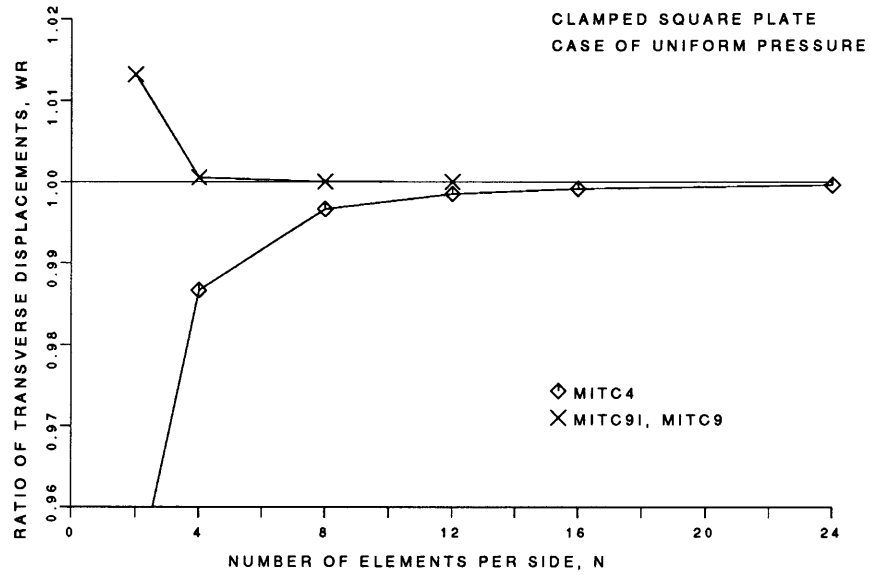


Figure 2-6 Continued.

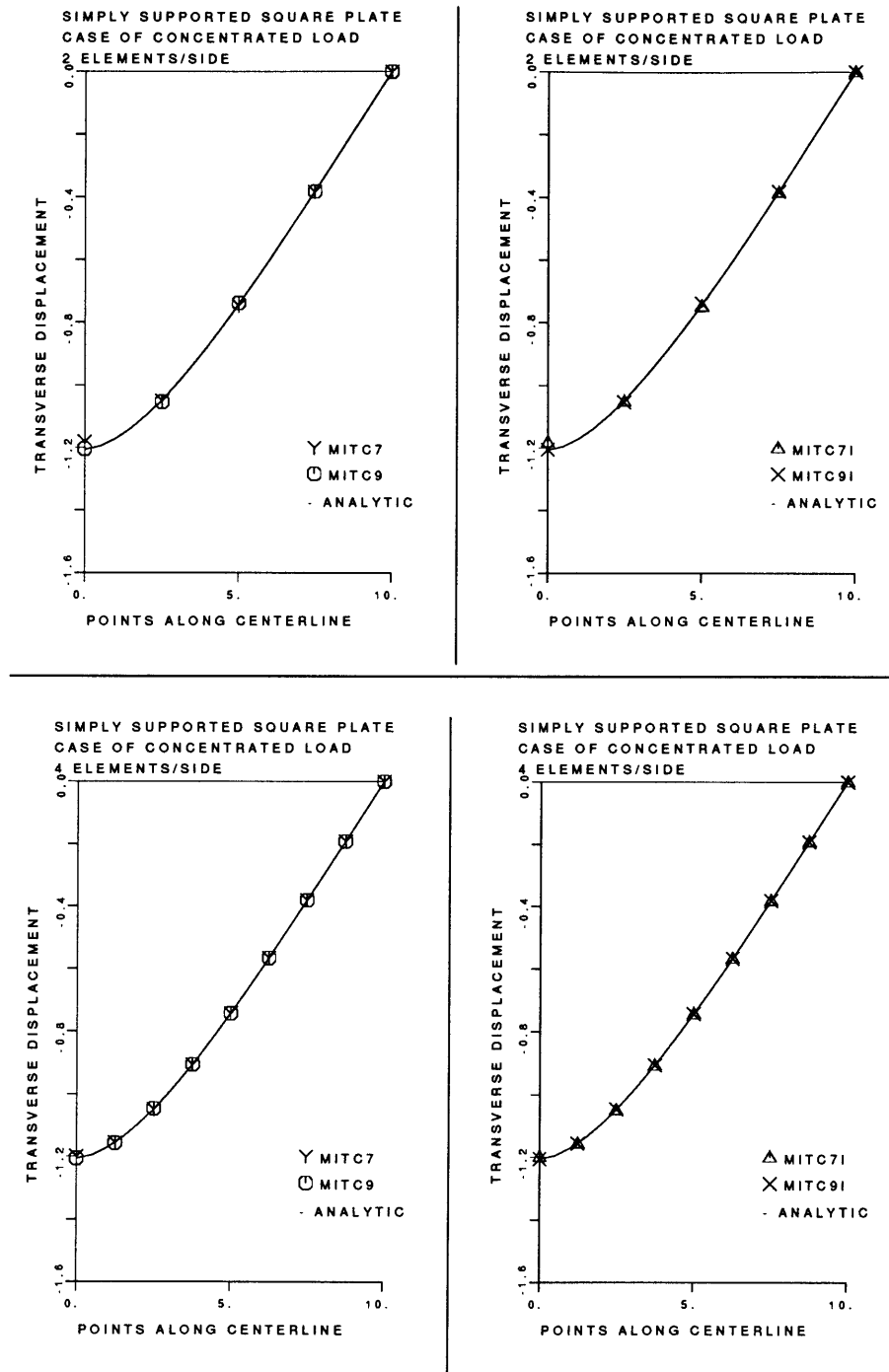


Figure 2-7: Displacement/stress response of a simply supported square plate using meshes of Fig. 2-5. Transverse displacement and in-plane stress along center line of the plate are shown for the case of concentrated load and uniform pressure loading.

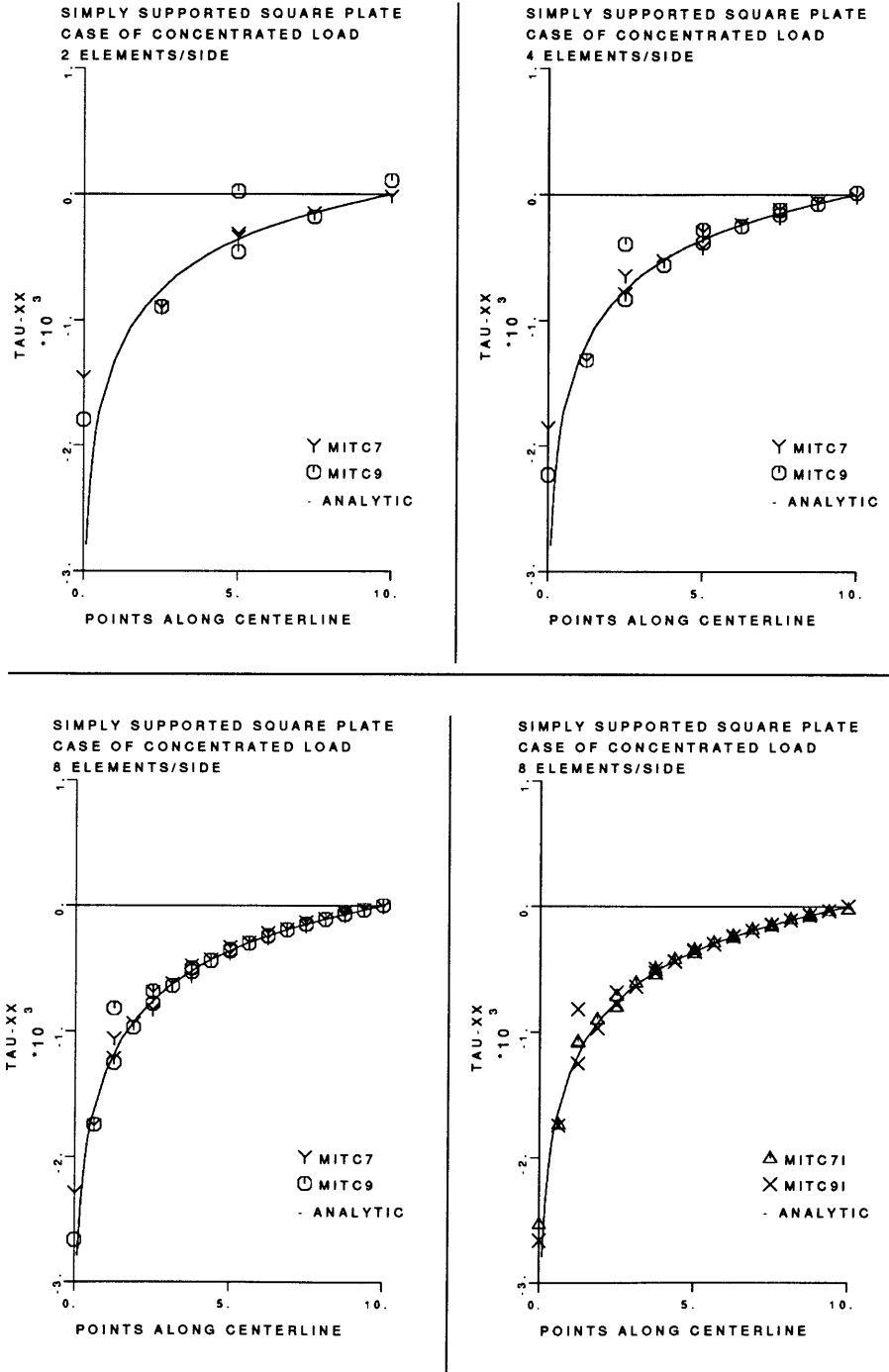


Figure 2-7 Continued.

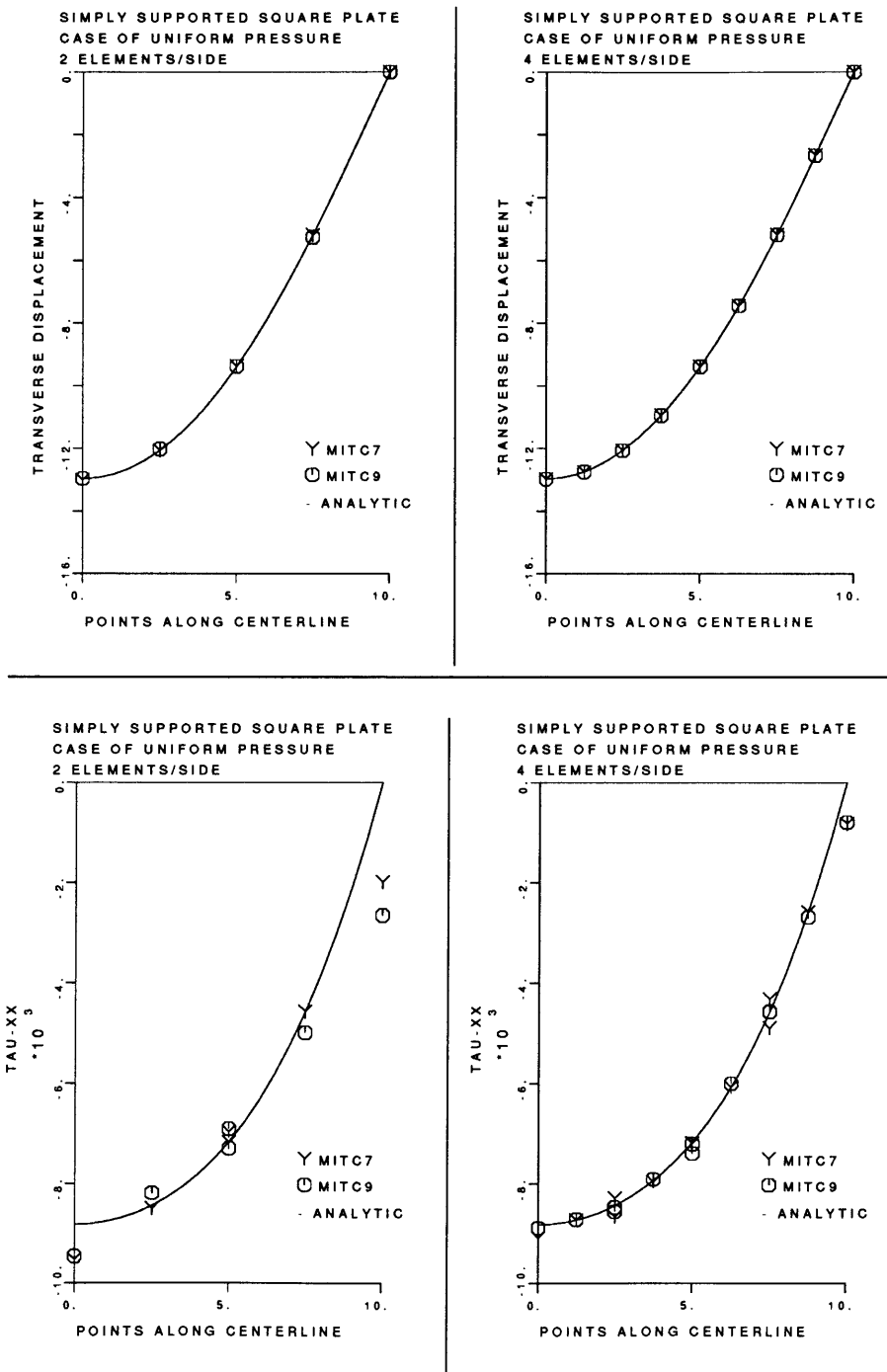


Figure 2-7 Continued.



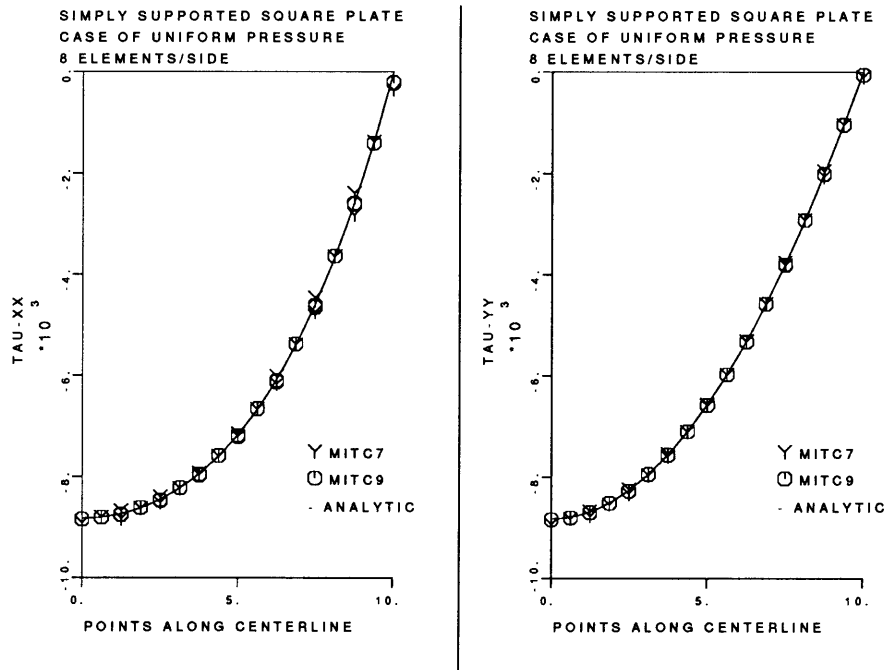


Figure 2-7 Continued.

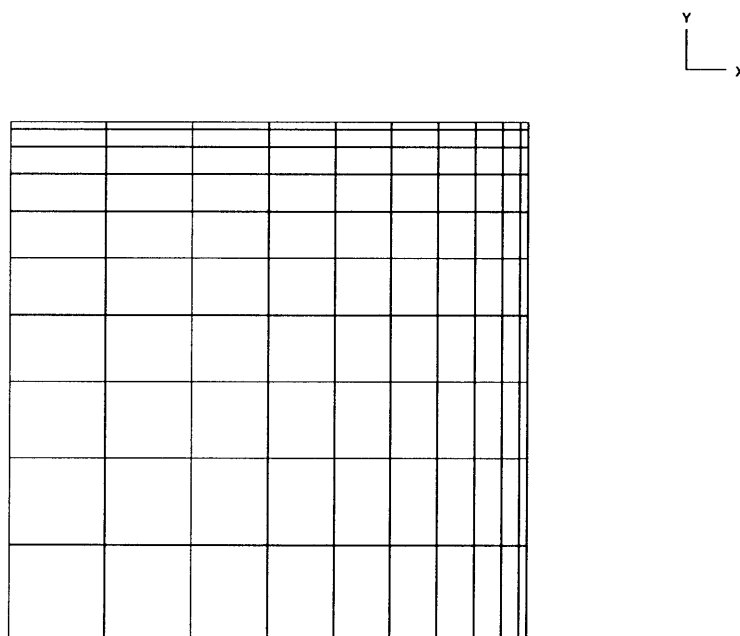


Figure 2-8:  $10 \times 10$  graded mesh used in a simply-supported plate, thickness/length =  $1/100$ .

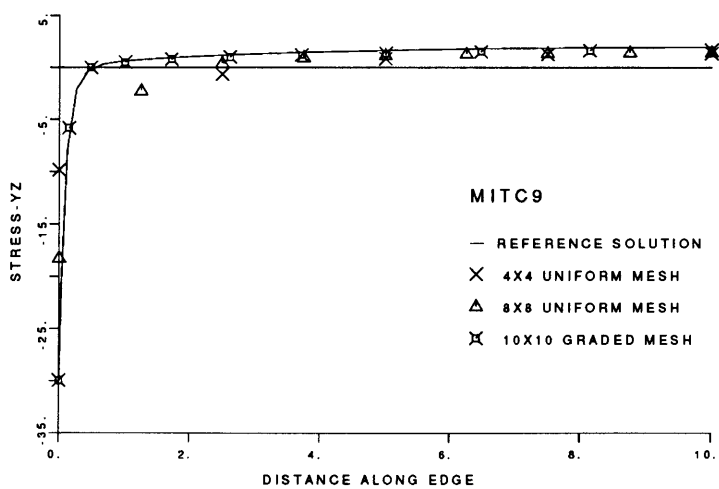
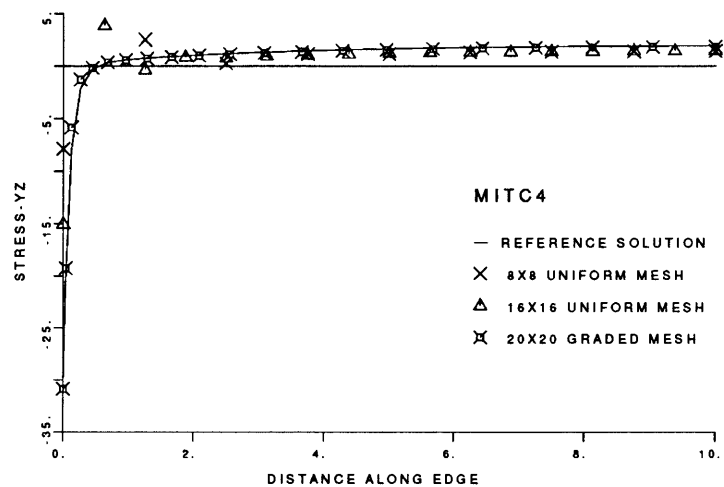


Figure 2-9: Shear stress predictions near corner of a simply-supported plate subjected to pressure loading.

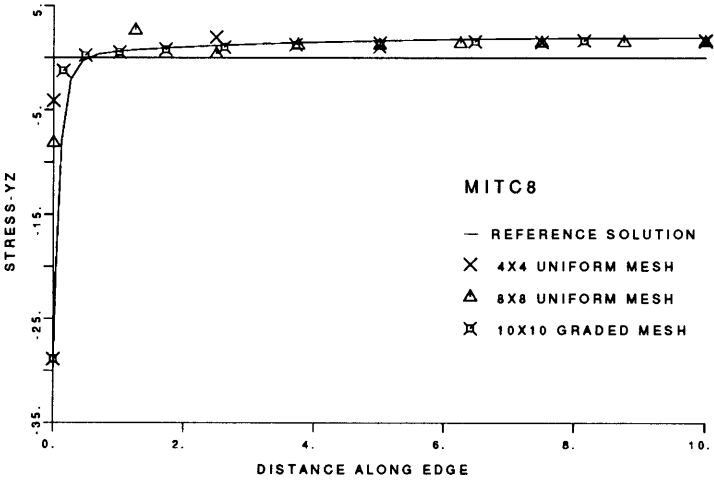


Figure 2-9 Continued.

### 2.3.3 Analysis of a Circular Plate

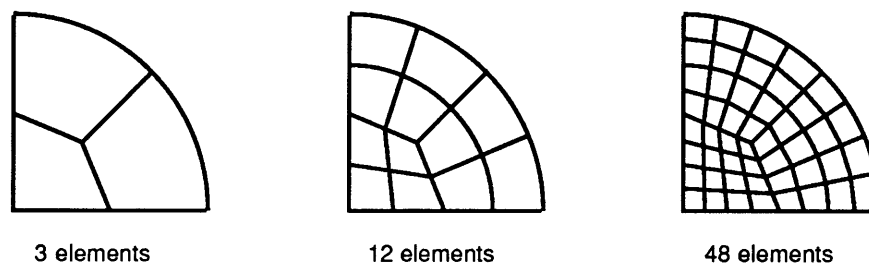
The analysis of a circular plate requires the use of non-rectangular elements, and thus the solution will display the predictive capabilities of the elements when they are geometrically distorted.

Figure 2-10 shows the circular plate problem considered and the meshes used. Table 2-2 compares the displacement results obtained and Figure 2-11 shows the displacement and stress distributions calculated using the MITC7 and MITC9 elements. Note that as in the analysis of the square plate, the stress jumps at the nodal points are less severe for the fine meshes, and are confined to the area of the stress singularity, *i.e.* the center of the plate.

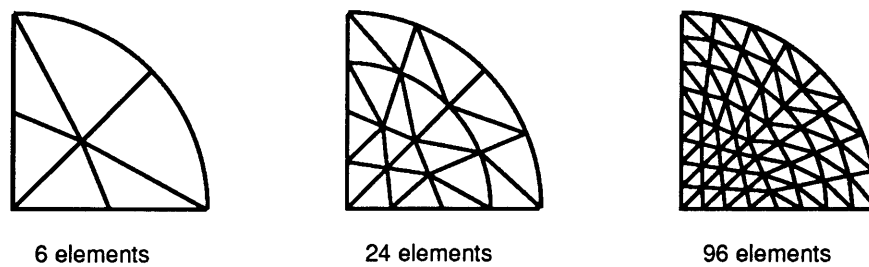
Furthermore, as in the analysis of the square plate, there is a little difference between the results obtained with the MITC7<sup>I</sup> and MITC7 elements, and the MITC9<sup>I</sup> and MITC9 elements, respectively.

Next, the prediction of shear stress along the radial line in a clamped square plate subjected to uniformly distributed pressure is studied. Figures 2-12 and 2-13 show the meshes used in this analysis. Figures 2-14 and 2-15 give the bending and transverse shear stresses predicted when the MITC4, MITC8, MITC9, MITC9<sup>I</sup> and MITC16<sup>I</sup> elements are employed in the solution. In Fig. 2-14 the results obtained with mesh A are shown whereas the results using mesh B are shown in Fig. 2-15. The reason is that the bending stresses are already quite well predicted in Fig. 2-14 with relatively coarse meshes (mesh A). Since the stresses have been calculated directly at the element nodes using the spaces  $\underline{Q}_h$  and  $\underline{L}_h$ , the stress jumps in Figs. 2-14 and 2-15.

To study the sensitivity of the elements due to geometric distortions a large artificial mesh distortion as shown in Fig. 2-13 (node A and the adjacent nodes were relocated) was applied. Figure 2-16 shows the shear stresses predicted when using the mesh of Fig. 2-13. The calculated shear stresses changed very little from the solutions given in Fig. 2-15.



(a) Rectangular mesh layout



(b) Triangular mesh layout

Figure 2-10: Finite element meshes used for the analysis of a circular plate. Diameter = 20, thickness = 0.02,  $E = 2.1 \times 10^6$ ,  $\nu = 0.3$ . Due to symmetry only one quarter of the plate is discretized.

Table 2-2: Analysis of a circular plate subjected to concentrated load at the center of the plate.

- The analytical solution used as reference is the Kirchhoff plate theory solution Ref. [Timoshenko and Woinowsky-Krieger, 1959].

Element	Mesh	$\alpha$ : simply supported edge	$\alpha$ : clamped edge
MITC4	3 elements	0.983	0.786
	12 elements	0.995	0.948
	48 elements	0.998	0.986
MITC8	3 elements	0.990	0.984
	12 elements	0.999	0.997
	48 elements	1.000	0.997
MITC7 <sup>I</sup>	6 elements	1.006	0.965
	24 elements	1.000	0.990
	96 elements	1.000	0.997
MITC9 <sup>I</sup>	3 elements	0.992	0.973
	12 elements	0.998	0.997
	48 elements	1.000	1.000
MITC7	6 elements	0.987	0.980
	24 elements	0.996	0.992
	96 elements	0.999	0.998
MITC9	3 elements	0.997	0.991
	12 elements	0.999	0.998
	48 elements	1.000	1.000
MITC12 <sup>I</sup>	3 elements	0.998	0.996
	12 elements	0.999	0.998
	48 elements	1.000	1.000
MITC12	3 elements	1.002	1.008
	12 elements	1.000	1.002
	48 elements	1.000	1.001
MITC16 <sup>I</sup>	3 elements	1.005	1.014
	12 elements	1.001	1.003
	48 elements	1.000	1.001

$$\alpha = \frac{w^{\text{fem}}}{w^{\text{analyt.}}} \quad \text{at center of the plate (thickness=0.02)}$$

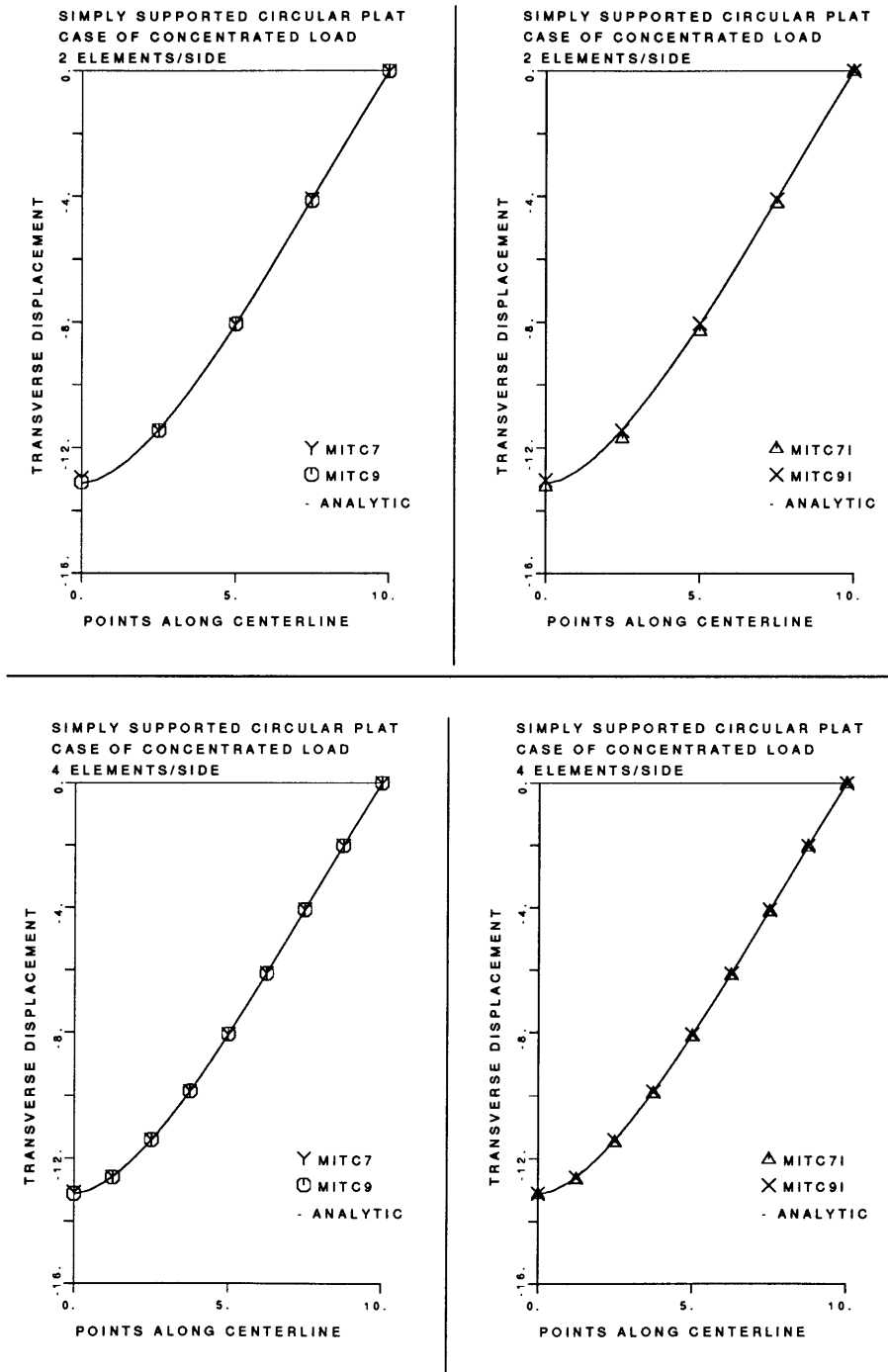


Figure 2-11: Displacement/stress response of a circular using meshes of Fig. 2-10. Transverse displacement and in-plane stress along radial line of the plate are shown for the case of concentrated load.



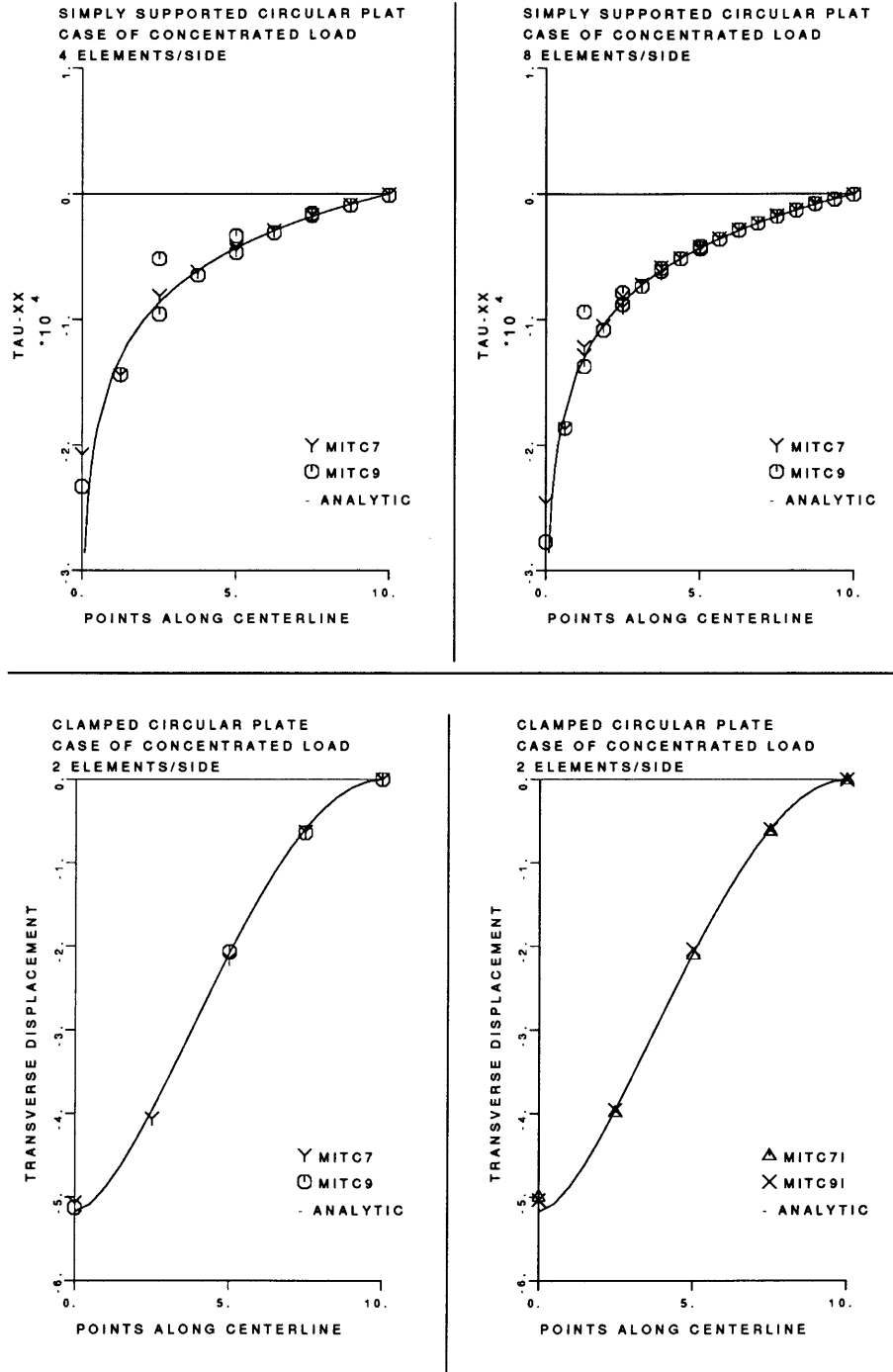


Figure 2-11 Continued.

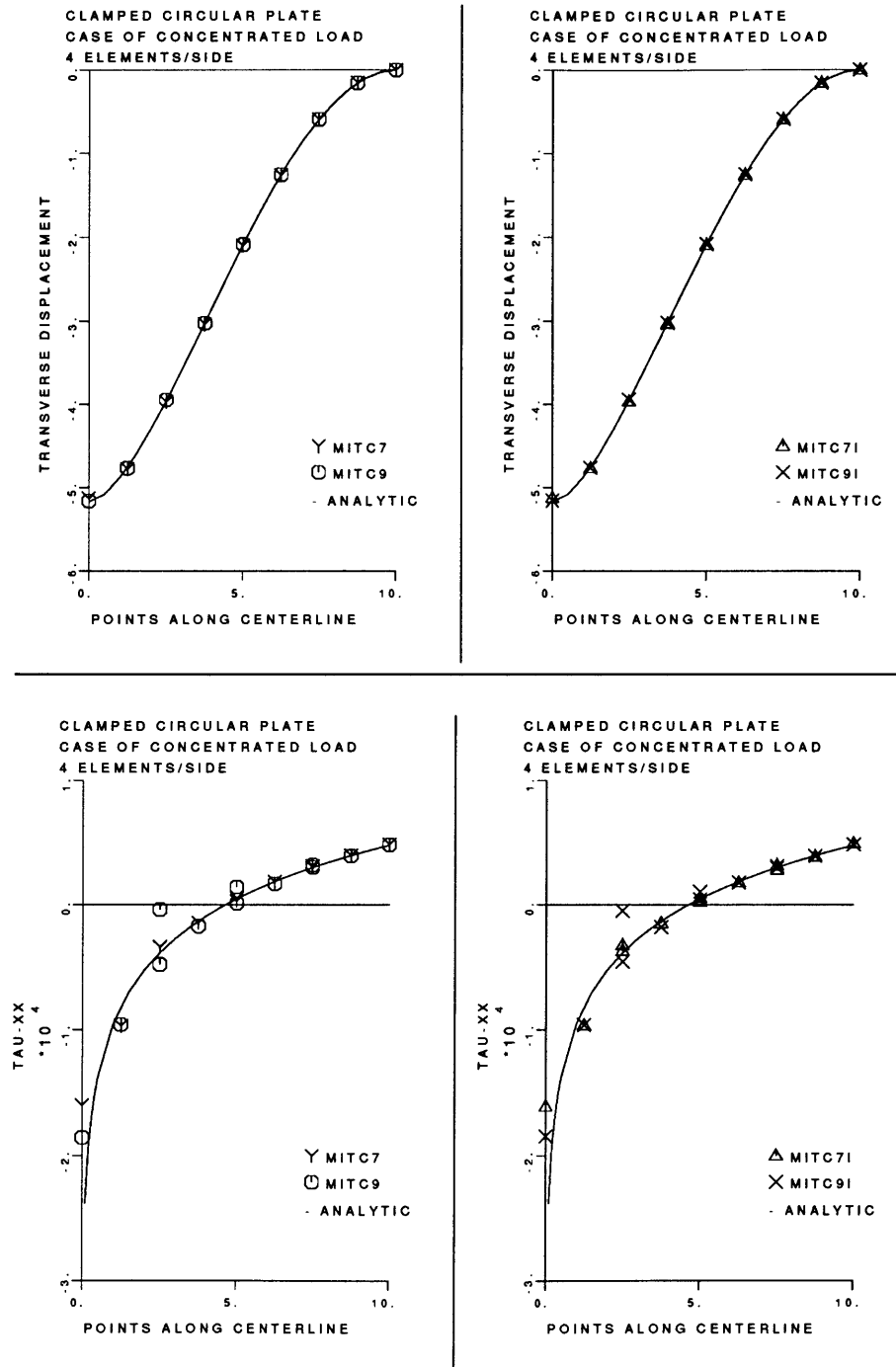


Figure 2-11 Continued.

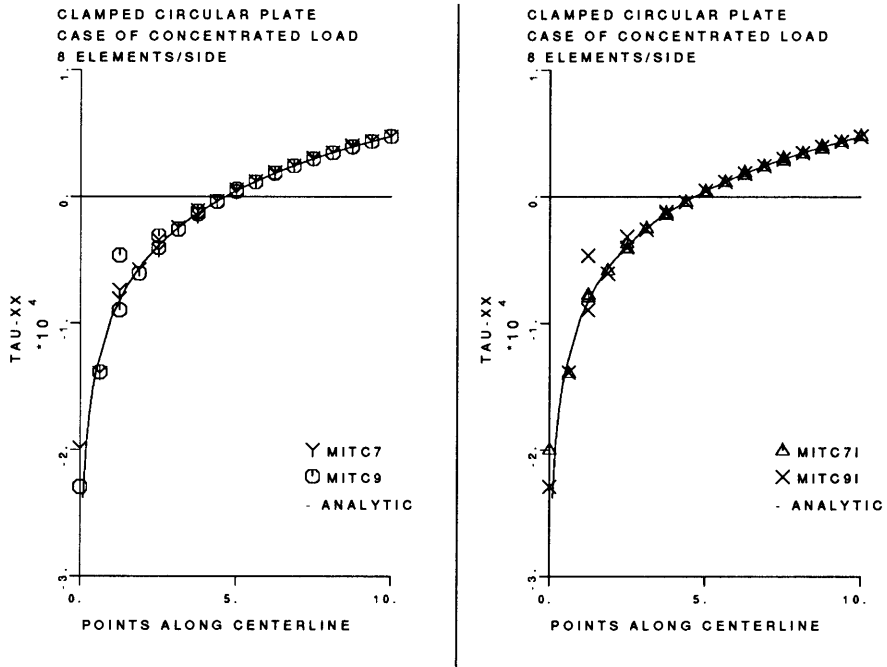


Figure 2-11 Continued.

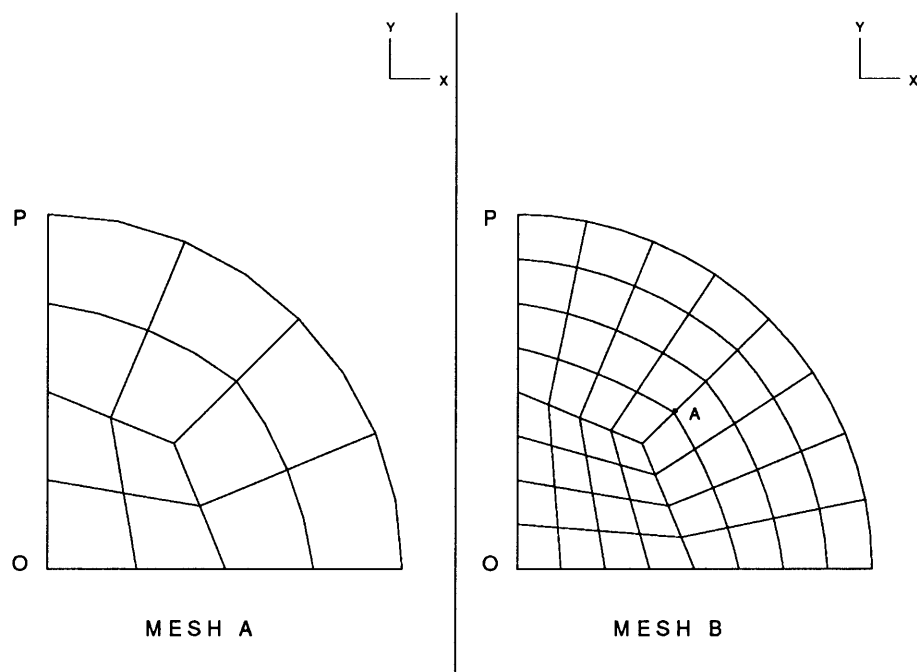


Figure 2-12: Finite element meshes used for the analysis of clamped circular plate, thickness/diameter = 1/100.

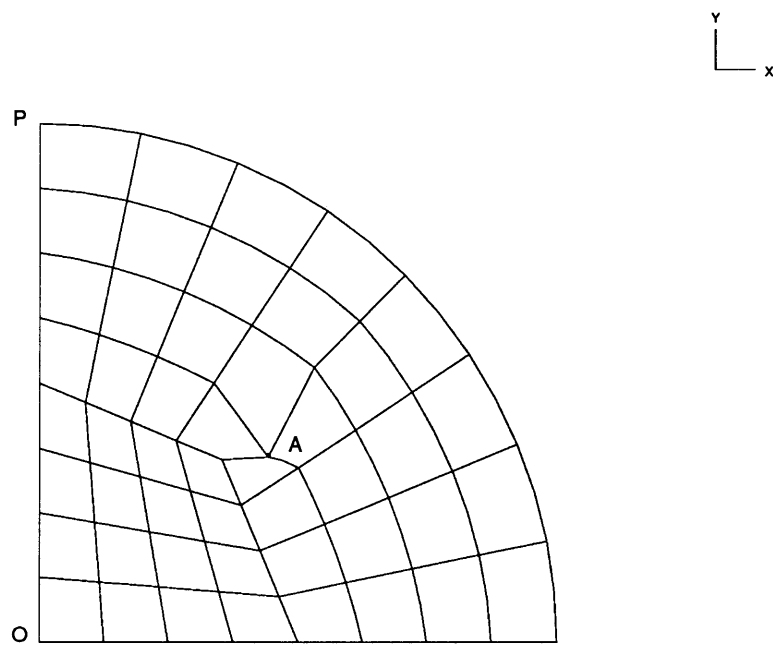


Figure 2-13: Distorted mesh B of Fig. 2-12 used in the analysis of a clamped circular plate,  
thickness/diameter = 1/100.

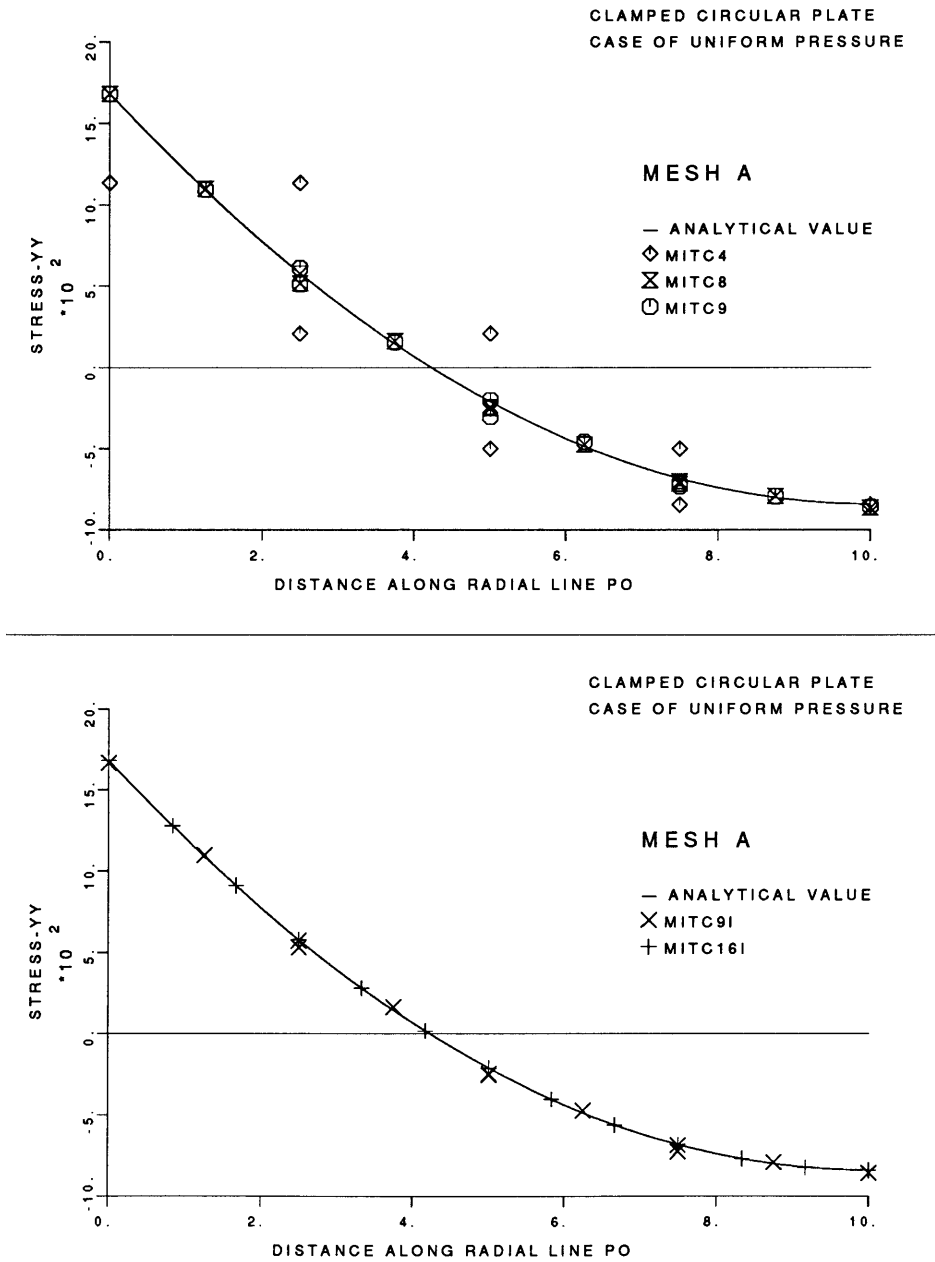


Figure 2-14: Radial bending stress prediction in a clamped circular plate, Mesh A.

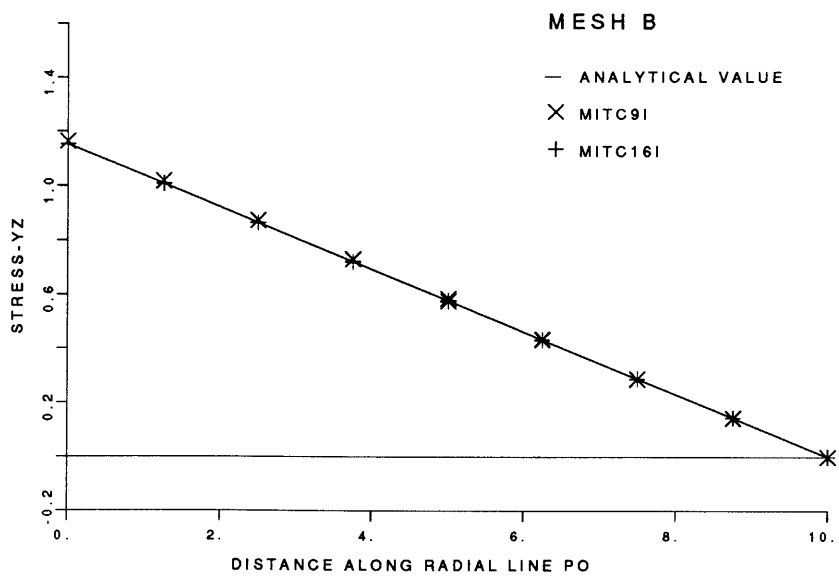
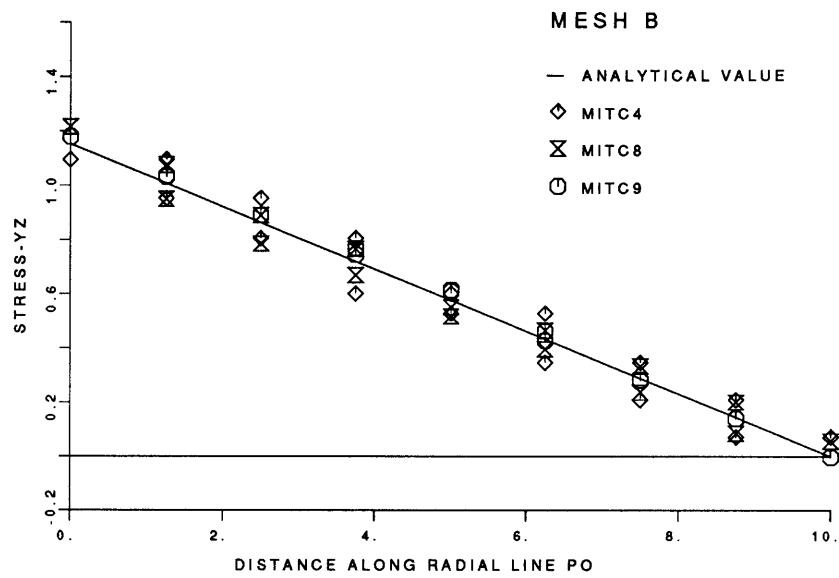


Figure 2-15: Transverse shear stress predictions obtained at element corner nodes in analysis of a clamped circular plate.

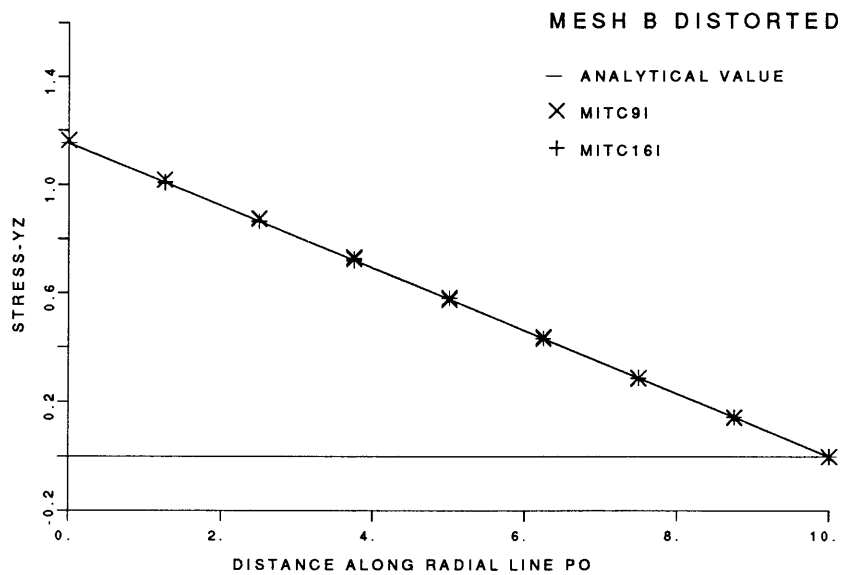
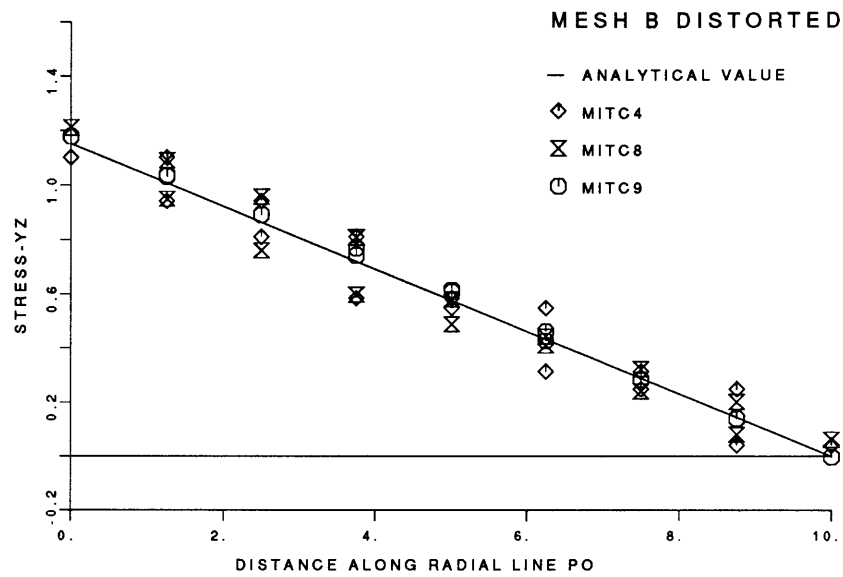


Figure 2-16: Transverse shear stress predictions obtained at element corner nodes in analysis of a clamped circular plate when using the distorted mesh of Fig 2-13.



# Chapter 3

## Formulation of the Mixed-Interpolated Nine-Node Shell Element

In this chapter, the mixed-interpolated plate element is extended to a general shell element. Since the MITC9 plate element shows excellent predictive capabilities, a MITC9 general shell element is proposed. The MITC8 shell element [Bathe and Dvorkin, 1986] is also discussed for comparison, and a suggestion for an improved MITC8 element is presented. Since the general shell element has a curved geometry, membrane strains need to be interpolated in addition to the shear strains to avoid membrane locking. The formulation consists of three phases: the displacement-based formulation of strains, the interpolation of the assumed strains (both membrane and shear strains), and the tying of the displacement assumptions to the strain assumptions. In the displacement formulation Reissner/Mindlin kinematics is assumed, and the standard procedure for establishing shell element from the 3-D continuum element is used.

For geometrically nonlinear analysis an incremental total Lagrangian formulation is used for the assumed strain-based curved shell element. In the construction of the element matrices for nonlinear analysis, the consideration of large rotations introduces difficul-

ties due to the non-vectorial nature of finite rotations. The consideration of the strain interpolations in the assumed strain-based element introduces additional difficulties due to the complexities arising from the construction of the strain matrices.

A derivation of the displacement-based shell finite element is presented by Bathe, and an extensive derivation of the kinematics of large rotations is presented by Argyris [Bathe, 1982; Argyris, 1982]. The formulation presented here includes all the terms in the linearized equations of motion that can be considered in a tangent stiffness formulation, as well as the exact assumed strain field treatment. Thus quadratic convergence can be achieved in the full Newton iteration.

### 3.1 Kinematics

The assumptions used for the shell kinematic and stress conditions are a generalization of Reissner/Mindlin plate theory. Figure 3-1 shows a typical shell to be analyzed. The kinematics of the shell are described by the motion of the shell mid-surface and the motion of the director vector  ${}^t\mathbf{V}_n$  which is defined for each material point of the mid-surface: the origin of the director vector is at the mid-surface of the shell and usually the vector is initially normal to the mid-surface. During the shell deformations the director vector translates and rotates, and if initially normal to the shell mid-surface it may not necessarily remain so (shear deformations are considered). To describe the motion of the director vector the three Cartesian displacements of the vector origin and the direction cosines of the vector are used. Note that the fundamental assumption is that the particle lying originally on the director vector will continue to lie on that vector throughout the motion.

Regarding the stress conditions it is assumed that the Cauchy stresses in the direction of the director vector are initially zero and remain zero throughout the motion of the shell. Hence, plane stress conditions with the direction “normal to the plane” defined by the director vector are assumed.

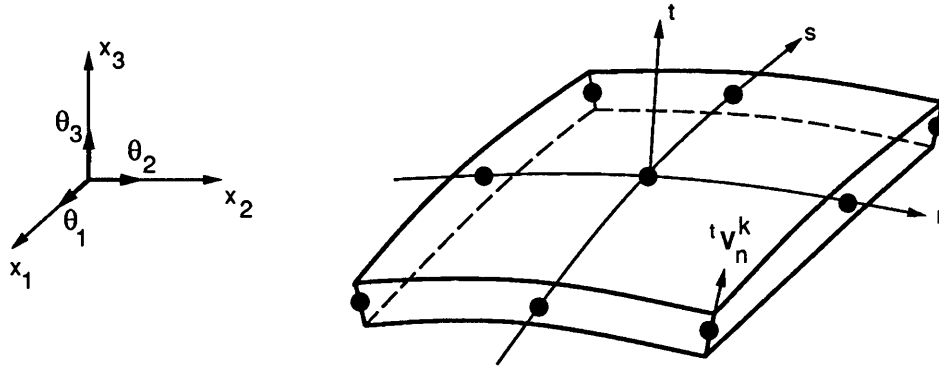


Figure 3-1: The geometry of the typical shell element. The direction of the isoparametric coordinate  $t$  is given by the director vector  ${}^t\mathbf{V}_n(r, s)$ .

### 3.2 Displacement-Based Shell Element

Figure 3-2 shows the orientation of the director vector  ${}^t\mathbf{V}_n$  and the directions of the rotational degrees of freedom  $\alpha_k$  and  $\beta_k$ . Defining the natural co-ordinate system  $(r, s, t)$  the position vector of any point inside the shell element is

$${}^0\mathbf{x}(r, s, t) = \sum_{k=1}^N h_k(r, s) {}^0\mathbf{x}_k + \frac{t}{2} \sum_{k=1}^N a_k h_k {}^0\mathbf{V}_n^k. \quad (3.1)$$

At any time  $t$ , the position vector of the  $(r, s, t)$  point in the degenerated shell element is,

$${}^t\mathbf{x}(r, s, t) = \sum_{k=1}^N h_k(r, s) {}^t\mathbf{x}_k + \frac{t}{2} \sum_{k=1}^N a_k h_k {}^t\mathbf{V}_n^k. \quad (3.2)$$

The displacement vector of the same point, corresponding to the configuration at time  $t$  is,

$${}^t\mathbf{u} = {}^t\mathbf{x} - {}^0\mathbf{x}. \quad (3.3)$$

Using Eqs. 3.1 and 3.2 in 3.3 the following equation can be obtained

$${}^t\mathbf{u} = \sum_{k=1}^N h_k {}^t\mathbf{u}_k + \frac{t}{2} \sum_{k=1}^N a_k h_k ({}^t\mathbf{V}_n^k - {}^0\mathbf{V}_n^k) \quad (3.4)$$

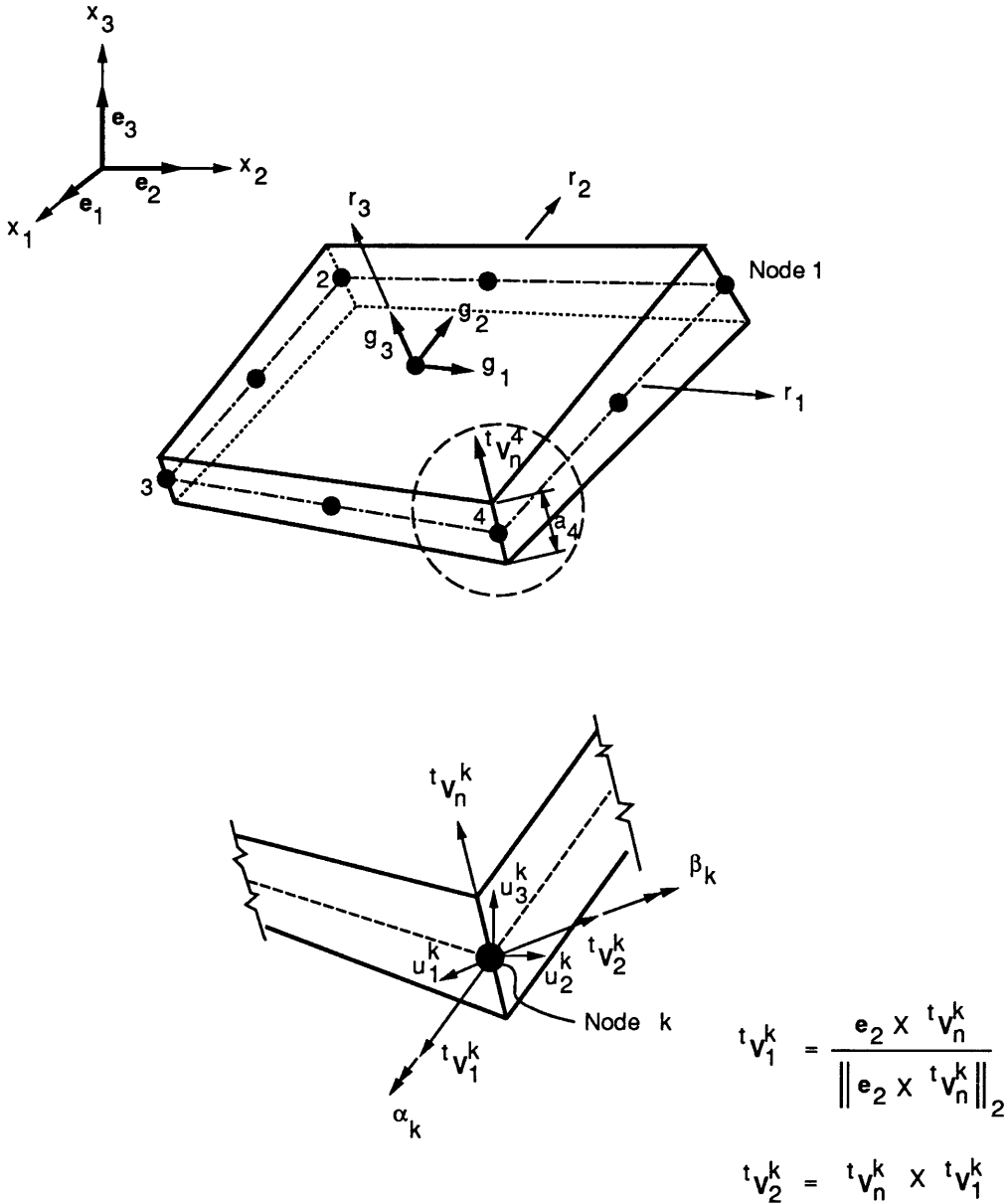


Figure 3-2: Definition of rotational degrees of freedom  $\alpha_k$  and  $\beta_k$ .

where  ${}^t\mathbf{u}_k$  is the displacement vector of node  $k$ , at time  $t$ .

Since the orthonormal system at node  $k$  rotates,

$${}^t\mathbf{V}_n^k = {}^t\mathbf{R}^k {}^0\mathbf{V}_n^k \quad (3.5)$$

where  ${}^t\mathbf{R}^k$  is the rotation matrix corresponding to node  $k$ , at time  $t$  and is referred to the initial configuration.

The rotation of the orthonormal system at node  $k$  can be described by a vector [Argyris, 1982],

$${}^t\underline{\theta}^k = {}^t\theta^k {}^t\mathbf{e}^k \quad (3.6a)$$

$${}^t\theta^k = \left[ \left( {}^t\theta_1^k \right)^2 + \left( {}^t\theta_2^k \right)^2 + \left( {}^t\theta_3^k \right)^2 \right] \quad (3.6b)$$

where  ${}^t\mathbf{e}^k$  is a unit vector in the direction of the rotation axis.

Studying this rotation, Argyris arrived at [Argyris, 1982]

$${}^t\mathbf{R}^k = \mathbf{I}_3 + \frac{\sin {}^t\theta^k}{{}^t\theta^k} {}^t\underline{\Theta}^k + \frac{1}{2} \left[ \frac{\sin \left( {}^t\theta^k / 2 \right)}{\left( {}^t\theta^k / 2 \right)} \right]^2 \left( {}^t\underline{\Theta}^k \right)^2 \quad (3.7)$$

where

$${}^t\underline{\Theta}^k = \begin{bmatrix} 0 & -{}^t\theta_3^k & {}^t\theta_2^k \\ {}^t\theta_3^k & 0 & -{}^t\theta_1^k \\ -{}^t\theta_2^k & {}^t\theta_1^k & 0 \end{bmatrix}. \quad (3.8)$$

Note that the  ${}^t\theta_i^k$  are not independent rotations around the global axes but are the components of the matrix defined in Eq. 3.8, which characterizes a rotation around the axis  ${}^t\mathbf{e}^k$ .

Argyris elegantly proved that Eq. 3.7 can be rewritten as,

$${}^t\mathbf{R}^k = \mathbf{I}_3 + {}^t\underline{\Theta}^k + \frac{1}{2!} \left( {}^t\underline{\Theta}^k \right)^2 + \frac{1}{3!} \left( {}^t\underline{\Theta}^k \right)^3 + \dots \quad (3.9)$$

where  $\mathbf{I}_3$  is a  $(3 \times 3)$  unit matrix.

The incremental displacement from the configuration at time  $t$  to the configuration at time  $t + \Delta t$  is,

$$\mathbf{u} = {}^{t+\Delta t}\mathbf{x} - {}^t\mathbf{x}. \quad (3.10)$$

Therefore,

$$\mathbf{u} = \sum_{k=1}^N h_k \mathbf{u}^k + \frac{t}{2} \sum_{k=1}^N a_k h_k ({}^{t+\Delta t}\mathbf{V}_n^k - {}^t\mathbf{V}_n^k). \quad (3.11)$$

To go from the configuration at time  $t$  to the configuration at time  $t + \Delta t$ , the orthogonal system at node  $k$  is only rotated; therefore,

$${}^{t+\Delta t}\mathbf{V}_n^k = {}^{t+\Delta t}{}_t\mathbf{R}^k {}^t\mathbf{V}_n^k. \quad (3.12)$$

Using Eq. 3.9,

$${}^{t+\Delta t}{}_t\mathbf{R}^k = \mathbf{I}_3 + \underline{\Theta}^k + \frac{1}{2!} (\underline{\Theta}^k)^2 + \frac{1}{3!} (\underline{\Theta}^k)^3 + \dots \quad (3.13)$$

where

$$\underline{\Theta}^k = \begin{bmatrix} 0 & -\theta_3^k & \theta_2^k \\ \theta_3^k & 0 & -\theta_1^k \\ -\theta_2^k & \theta_1^k & 0 \end{bmatrix}. \quad (3.14)$$

Again, the  $\theta_i^k$  are not independent incremental rotations around the global axes, but they are the components of the matrix defined in Eq. 3.14 which characterizes via Eq. 3.13 the incremental rotations at node  $k$ .

Note, that if the incremental rotations are infinitesimal, keeping only the linear terms in Eq. 3.13, Eqs. 3.12 through 3.14 produce,

$${}^{t+\Delta t}\mathbf{V}_n^k - {}^t\mathbf{V}_n^k = \underline{\theta}^k \times {}^t\mathbf{V}_n^k \quad (3.15)$$

where  $[\underline{\theta}^k]^T = [\theta_1^k, \theta_2^k, \theta_3^k]$ . In this case the  $\theta_i^k$  are independent infinitesimal incremental rotations around the three global axes.

Because the incremental rotations are finite we keep the linear and the quadratic

terms in Eq. 3.13.

Therefore,

$${}^{t+\Delta t}\mathbf{V}_n^k - {}^t\mathbf{V}_n^k = \underline{\Theta}^k {}^t\mathbf{V}_n^k + \frac{1}{2}\underline{\Theta}^k \underline{\Theta}^k {}^t\mathbf{V}_n^k \quad (3.16)$$

can be rewritten as

$${}^{t+\Delta t}\mathbf{V}_n^k - {}^t\mathbf{V}_n^k = \underline{\theta}^k \times {}^t\mathbf{V}_n^k + \frac{1}{2}\underline{\theta}^k \times (\underline{\theta}^k \times {}^t\mathbf{V}_n^k) \quad (3.17)$$

Since the incremental rotations  $\alpha_k$  and  $\beta_k$  in the shell element are given with respect to the  ${}^t\mathbf{V}_1^k$ - ${}^t\mathbf{V}_2^k$ - ${}^t\mathbf{V}_n^k$  frame, the vector crossproduct in Eq. 3.17 can be effectively evaluated in the  ${}^t\mathbf{V}_1^k$ - ${}^t\mathbf{V}_2^k$ - ${}^t\mathbf{V}_n^k$  frame to get

$${}^{t+\Delta t}\mathbf{V}_n^k - {}^t\mathbf{V}_n^k = -\alpha_k {}^t\mathbf{V}_2^k + \beta_k {}^t\mathbf{V}_1^k - \frac{1}{2}(\alpha_k^2 + \beta_k^2) {}^t\mathbf{V}_n^k. \quad (3.18)$$

Using Eq. 3.18 in 3.11,

$$\mathbf{u} = \sum_{k=1}^N h_k \mathbf{u}^k + \frac{t}{2} \sum_{k=1}^N a_k h_k \left[ -\alpha_k {}^t\mathbf{V}_2^k + \beta_k {}^t\mathbf{V}_1^k - \frac{1}{2}(\alpha_k^2 + \beta_k^2) {}^t\mathbf{V}_n^k \right] \quad (3.19)$$

and,

$$\mathbf{u} = \mathbf{u}_L + \mathbf{u}_Q \quad (3.20)$$

where  $\mathbf{u}_L$  is the term obtained considering only the infinitesimal rotation increments, (i.e. using Eq. 3.15) and  $\mathbf{u}_Q$  is the extra term obtained using Eq. 3.18.

Hence,

$$\mathbf{u}_L = \sum_{k=1}^N h_k \mathbf{u}^k + \frac{t}{2} \sum_{k=1}^N a_k h_k \left[ -\alpha_k {}^t\mathbf{V}_2^k + \beta_k {}^t\mathbf{V}_1^k \right] \quad (3.21)$$

and

$$\mathbf{u}_Q = \frac{t}{2} \sum_{k=1}^N a_k h_k \left[ -\frac{1}{2}(\alpha_k^2 + \beta_k^2) {}^t\mathbf{V}_n^k \right]. \quad (3.22)$$

At any time  $t$ , the covariant base vectors of the convected systems  $(r, s, t)$  are [Green and

Zerna, 1968]

$${}^t\mathbf{g}_r = \frac{\partial {}^t\mathbf{x}}{\partial r} = {}^0\mathbf{g}_r + \frac{\partial {}^t\mathbf{u}}{\partial r} \quad (3.23a)$$

$${}^t\mathbf{g}_s = \frac{\partial {}^t\mathbf{x}}{\partial s} = {}^0\mathbf{g}_s + \frac{\partial {}^t\mathbf{u}}{\partial s} \quad (3.23b)$$

$${}^t\mathbf{g}_t = \frac{\partial {}^t\mathbf{x}}{\partial t} = {}^0\mathbf{g}_t + \frac{\partial {}^t\mathbf{u}}{\partial t}. \quad (3.23c)$$

Similarly, in the incremental step from time  $t$  to  $t + \Delta t$ ,

$${}^{t+\Delta t}\mathbf{g}_r = \frac{\partial {}^{t+\Delta t}\mathbf{x}}{\partial r} = {}^t\mathbf{g}_r + \frac{\partial \mathbf{u}}{\partial r} \quad (3.24a)$$

$${}^{t+\Delta t}\mathbf{g}_s = \frac{\partial {}^{t+\Delta t}\mathbf{x}}{\partial s} = {}^t\mathbf{g}_s + \frac{\partial \mathbf{u}}{\partial s} \quad (3.24b)$$

$${}^{t+\Delta t}\mathbf{g}_t = \frac{\partial {}^{t+\Delta t}\mathbf{x}}{\partial t} = {}^t\mathbf{g}_t + \frac{\partial \mathbf{u}}{\partial t}. \quad (3.24c)$$

The covariant components of the Green-Lagrange deformation tensor in the configuration at times  $t$  and  $t + \Delta t$ , referred to the configuration at time  $t = 0$  and measured in the convected system are [Green and Zerna, 1968]

$${}^t_0\varepsilon = {}^t_0\tilde{\varepsilon}_{ij} {}^0\mathbf{g}_i \cdot {}^0\mathbf{g}_j = \frac{1}{2} \left( {}^t\mathbf{g}_i \cdot {}^t\mathbf{g}_j - {}^0\mathbf{g}_i \cdot {}^0\mathbf{g}_j \right) {}^0\mathbf{g}^i \cdot {}^0\mathbf{g}^j \quad (3.25)$$

$${}^{t+\Delta t}_0\varepsilon = {}^{t+\Delta t}_0\tilde{\varepsilon}_{ij} {}^0\mathbf{g}_i \cdot {}^0\mathbf{g}_j = \frac{1}{2} \left( {}^{t+\Delta t}\mathbf{g}_i \cdot {}^{t+\Delta t}\mathbf{g}_j - {}^0\mathbf{g}_i \cdot {}^0\mathbf{g}_j \right) {}^0\mathbf{g}^i \cdot {}^0\mathbf{g}^j. \quad (3.26)$$

Therefore, using Eqs. 3.23 and 3.24 in Eqs. 3.25 and 3.26, the incremental Green-Lagrange strain is expressed as,

$$\begin{aligned} {}_0\varepsilon &= \left[ {}^{t+\Delta t}_0\tilde{\varepsilon}_{ij} - {}^t_0\tilde{\varepsilon}_{ij} \right] {}^0\mathbf{g}^i \cdot {}^0\mathbf{g}^j \\ &= \frac{1}{2} \left[ {}^{t+\Delta t}\mathbf{g}_i \cdot {}^{t+\Delta t}\mathbf{g}_j - {}^t\mathbf{g}_i \cdot {}^t\mathbf{g}_j \right] {}^0\mathbf{g}^i \cdot {}^0\mathbf{g}^j \\ &= \frac{1}{2} \left[ \frac{\partial \mathbf{u}}{\partial r_i} \cdot {}^t\mathbf{g}_j + {}^t\mathbf{g}_i \cdot \frac{\partial \mathbf{u}}{\partial r_j} + \frac{\partial \mathbf{u}}{\partial r_i} \cdot \frac{\partial \mathbf{u}}{\partial r_j} \right] {}^0\mathbf{g}^i \cdot {}^0\mathbf{g}^j. \end{aligned} \quad (3.27)$$

The strain increment ( ${}_0\tilde{\varepsilon}_{ij}$ ) can be decomposed into two parts: One part has all the



linear terms in generalized displacements ( ${}^0\tilde{\epsilon}_{ij}$ ); and the other has all the quadratic terms in generalized displacements ( ${}^0\tilde{\eta}_{ij}$ ) [Bathe, 1982]. Therefore,

$${}^0\tilde{\epsilon}_{ij} = {}^0\tilde{\epsilon}_{ij} + {}^0\tilde{\eta}_{ij}. \quad (3.28)$$

Note that:

- In elements with no rotational degrees of freedom (e.g. 2-D and 3-D continuum elements) Eq. 3.28 represents exactly the total strain increments. In the present case, Eq. 3.28 represents only an approximation to the strain increments, because in the derivation of Eq. 3.27 the terms of order higher than two in generalized displacement increments are neglected [Bathe, 1986].
- Equation 3.27 contains all the terms up to the second order in generalized displacement increments. This guarantees a complete quadratic form of the incremental energy, thus leading to a complete expression of the tangent stiffness matrix.

Using Eq. 3.20 in Eq. 3.27, the terms in Eq. 3.28 can be expressed as:

$${}^0\tilde{\epsilon}_{ij} = \frac{1}{2} \left[ \frac{\partial \mathbf{u}_L}{\partial r_i} \cdot {}^t\mathbf{g}_j + {}^t\mathbf{g}_i \cdot \frac{\partial \mathbf{u}_L}{\partial r_j} \right] \quad (3.29)$$

$${}^0\tilde{\eta}_{ij} = \frac{1}{2} \left[ \frac{\partial \mathbf{u}_L}{\partial r_i} \cdot \frac{\partial \mathbf{u}_L}{\partial r_j} \right] + \frac{1}{2} \left[ \frac{\partial \mathbf{u}_Q}{\partial r_i} \cdot {}^t\mathbf{g}_j + {}^t\mathbf{g}_i \cdot \frac{\partial \mathbf{u}_Q}{\partial r_j} \right]. \quad (3.30)$$

Writing Eq. 3.29 and 3.30 for each component:

$${}^0\tilde{\epsilon}_{rr} = \sum_{k=1}^N {}^t\mathbf{g}_r \cdot (h_{k,r} \mathbf{u}_k) + \sum_{k=1}^N {}^t\mathbf{g}_r \cdot \left[ \frac{t}{2} a_k h_{k,r} (-\alpha_k {}^t\mathbf{V}_2^k + \beta_k {}^t\mathbf{V}_1^k) \right] \quad (3.31a)$$

$${}^0\tilde{\epsilon}_{ss} = \sum_{k=1}^N {}^t\mathbf{g}_s \cdot (h_{k,s} \mathbf{u}_k) + \sum_{k=1}^N {}^t\mathbf{g}_s \cdot \left[ \frac{t}{2} a_k h_{k,s} (-\alpha_k {}^t\mathbf{V}_2^k + \beta_k {}^t\mathbf{V}_1^k) \right] \quad (3.31b)$$

$$2 {}^0\tilde{\epsilon}_{rs} = \sum_{k=1}^N {}^t\mathbf{g}_r \cdot (h_{k,s} \mathbf{u}_k) + \sum_{k=1}^N {}^t\mathbf{g}_r \cdot \left[ \frac{t}{2} a_k h_{k,s} (-\alpha_k {}^t\mathbf{V}_2^k + \beta_k {}^t\mathbf{V}_1^k) \right]$$

$$+ \sum_{k=1}^N {}^t\mathbf{g}_s \cdot (h_{k,r} \mathbf{u}_k) + \sum_{k=1}^N {}^t\mathbf{g}_s \cdot \left[ \frac{t}{2} a_k h_{k,r} (-\alpha_k {}^t\mathbf{V}_2^k + \beta_k {}^t\mathbf{V}_1^k) \right] \quad (3.31c)$$

$$2 {}_0\tilde{\epsilon}_{rt} = \sum_{k=1}^N {}^t\mathbf{g}_t \cdot (h_{k,r} \mathbf{u}_k) + \sum_{k=1}^N {}^t\mathbf{g}_r \cdot \left[ \frac{1}{2} a_k h_k (-\alpha_k {}^t\mathbf{V}_2^k + \beta_k {}^t\mathbf{V}_1^k) \right] \quad (3.31d)$$

$$2 {}_0\tilde{\epsilon}_{st} = \sum_{k=1}^N {}^t\mathbf{g}_t \cdot (h_{k,s} \mathbf{u}_k) + \sum_{k=1}^N {}^t\mathbf{g}_s \cdot \left[ \frac{1}{2} a_k h_k (-\alpha_k {}^t\mathbf{V}_2^k + \beta_k {}^t\mathbf{V}_1^k) \right]. \quad (3.31e)$$

Equation 3.31 is used to construct the linear incremental strains at the sampling points in the assumed strain formulation.

Now define the following matrices:

$$\frac{\partial \mathbf{u}_L}{\partial r} = \begin{bmatrix} h_{k,r} & 0 & 0 & -\frac{t}{2} a_k h_{k,r} {}^tV_{2x} & \frac{t}{2} a_k h_{k,r} {}^tV_{1x} \\ \dots & 0 & h_{k,r} & 0 & -\frac{t}{2} a_k h_{k,r} {}^tV_{2y} & \frac{t}{2} a_k h_{k,r} {}^tV_{1y} & \dots \\ 0 & 0 & h_{k,r} & -\frac{t}{2} a_k h_{k,r} {}^tV_{2z} & \frac{t}{2} a_k h_{k,r} {}^tV_{1z} \end{bmatrix} \mathbf{U} \equiv \tilde{\mathbf{B}}_r \mathbf{U} \quad (3.32a)$$

$$\frac{\partial \mathbf{u}_L}{\partial s} = \begin{bmatrix} h_{k,s} & 0 & 0 & -\frac{t}{2} a_k h_{k,s} {}^tV_{2x} & \frac{t}{2} a_k h_{k,s} {}^tV_{1x} \\ \dots & 0 & h_{k,s} & 0 & -\frac{t}{2} a_k h_{k,s} {}^tV_{2y} & \frac{t}{2} a_k h_{k,s} {}^tV_{1y} & \dots \\ 0 & 0 & h_{k,s} & -\frac{t}{2} a_k h_{k,s} {}^tV_{2z} & \frac{t}{2} a_k h_{k,s} {}^tV_{1z} \end{bmatrix} \mathbf{U} \equiv \tilde{\mathbf{B}}_s \mathbf{U} \quad (3.32b)$$

$$\frac{\partial \mathbf{u}_L}{\partial t} = \begin{bmatrix} 0 & 0 & 0 & -\frac{1}{2} a_k h_k {}^tV_{2x} & \frac{1}{2} a_k h_k {}^tV_{1x} \\ \dots & 0 & 0 & 0 & -\frac{1}{2} a_k h_k {}^tV_{2y} & \frac{1}{2} a_k h_k {}^tV_{1y} & \dots \\ 0 & 0 & 0 & -\frac{1}{2} a_k h_k {}^tV_{2z} & \frac{1}{2} a_k h_k {}^tV_{1z} \end{bmatrix} \mathbf{U} \equiv \tilde{\mathbf{B}}_t \mathbf{U} \quad (3.32c)$$

and for in-layer strains,

$${}^t\mathbf{g}_r \cdot \frac{\partial \mathbf{u}_Q}{\partial r} \equiv \mathbf{U}^T \tilde{\mathbf{B}}_{rr}^2 \mathbf{U} \quad (3.33a)$$

$${}^t\mathbf{g}_s \cdot \frac{\partial \mathbf{u}_Q}{\partial s} \equiv \mathbf{U}^T \tilde{\mathbf{B}}_{ss}^2 \mathbf{U} \quad (3.33b)$$

$${}^t\mathbf{g}_r \cdot \frac{\partial \mathbf{u}_Q}{\partial s} \equiv \mathbf{U}^T \tilde{\mathbf{B}}_{rs}^2 \mathbf{U} \quad (3.33c)$$

$${}^t\mathbf{g}_s \cdot \frac{\partial \mathbf{u}_Q}{\partial r} \equiv \mathbf{U}^T \tilde{\mathbf{B}}_{sr}^2 \mathbf{U} \quad (3.33d)$$

where the matrices  $\tilde{\mathbf{B}}_{r_i r_j}^2$  in Eq. 3.33 are the diagonal matrices whose values are given as,

$$\tilde{B}_{r_i r_j}^2 \left[ 2(k-1) + m, 2(k-1) + m \right] = \begin{cases} 0 & \text{for } m = 1, 2, 3 \\ -\frac{t}{4} a_k h_{k, r_j} {}^t \mathbf{g}_{r_i} \cdot \mathbf{V}_n^k & \text{for } m = 4, 5 \end{cases} \quad (3.34)$$

where  $k$  is a node number. In other words, the diagonal terms in matrices  $\tilde{\mathbf{B}}_{r_i r_j}^2$  in Eq. 3.33 have zero values for the terms corresponding to the displacement degrees of freedom, and they have the value given in Eq. 3.34 for the terms corresponding to the rotational degrees of freedom.

For shear strains,

$${}^t \mathbf{g}_r \cdot \frac{\partial \mathbf{u}_Q}{\partial t} \equiv \mathbf{U}^T \tilde{\mathbf{B}}_{rt}^2 \mathbf{U} \quad (3.35a)$$

$${}^t \mathbf{g}_t \cdot \frac{\partial \mathbf{u}_Q}{\partial r} \equiv \mathbf{U}^T \tilde{\mathbf{B}}_{tr}^2 \mathbf{U} \quad (3.35b)$$

$${}^t \mathbf{g}_s \cdot \frac{\partial \mathbf{u}_Q}{\partial t} \equiv \mathbf{U}^T \tilde{\mathbf{B}}_{st}^2 \mathbf{U} \quad (3.35c)$$

$${}^t \mathbf{g}_t \cdot \frac{\partial \mathbf{u}_Q}{\partial s} \equiv \mathbf{U}^T \tilde{\mathbf{B}}_{ts}^2 \mathbf{U} \quad (3.35d)$$

where the matrices  $\tilde{\mathbf{B}}_{r_i r_j}^2$  in Eq. 3.35 are the diagonal matrices whose values are given as,

$$\tilde{B}_{r_i r_j}^2 \left[ 2(k-1) + m, 2(k-1) + m \right] = \begin{cases} 0 & \text{for } m = 1, 2, 3 \\ -\frac{1}{4} a_k h_k {}^t \mathbf{g}_{r_i} \cdot \mathbf{V}_n^k & \text{for } m = 4, 5 \text{ and } \tilde{\mathbf{B}}_{rt}^2, \tilde{\mathbf{B}}_{st}^2 \\ -\frac{t}{4} a_k h_{k, r_j} {}^t \mathbf{g}_{r_i} \cdot \mathbf{V}_n^k & \text{for } m = 4, 5 \text{ and } \tilde{\mathbf{B}}_{tr}^2, \tilde{\mathbf{B}}_{ts}^2 \end{cases} \quad (3.36)$$

where  $k$  is a node number. In other words, the diagonal terms in matrices  $\tilde{\mathbf{B}}_{r_i r_j}^2$  in Eq. 3.35 have zero values for the terms corresponding to the displacement degrees of freedom and they have the value given in Eq. 3.36 for the terms corresponding to the rotational degrees of freedom.

Finally, using Eqs. 3.32, 3.33 and 3.35 in Eq. 3.30 a matrix expression for the directly interpolated nonlinear incremental strains can be obtained. Hence, the variation of the

nonlinear incremental strains are,

$$\delta {}_0\tilde{\eta}_{rr} = \delta \mathbf{U}^T [\tilde{\mathbf{B}}_r^T \tilde{\mathbf{B}}_r + 2\tilde{\mathbf{B}}_{rr}^2] \mathbf{U} \quad (3.37a)$$

$$\delta {}_0\tilde{\eta}_{ss} = \delta \mathbf{U}^T [\tilde{\mathbf{B}}_s^T \tilde{\mathbf{B}}_s + 2\tilde{\mathbf{B}}_{ss}^2] \mathbf{U} \quad (3.37b)$$

$$\delta {}_0\tilde{\eta}_{rs} = \delta \mathbf{U}^T [\frac{1}{2}\tilde{\mathbf{B}}_r^T \tilde{\mathbf{B}}_s + \frac{1}{2}\tilde{\mathbf{B}}_s^T \tilde{\mathbf{B}}_r + \tilde{\mathbf{B}}_{rs}^2 + \tilde{\mathbf{B}}_{sr}^2] \mathbf{U} \quad (3.37c)$$

$$\delta {}_0\tilde{\eta}_{rt} = \delta \mathbf{U}^T [\frac{1}{2}\tilde{\mathbf{B}}_r^T \tilde{\mathbf{B}}_t + \frac{1}{2}\tilde{\mathbf{B}}_t^T \tilde{\mathbf{B}}_r + \tilde{\mathbf{B}}_{rt}^2 + \tilde{\mathbf{B}}_{tr}^2] \mathbf{U} \quad (3.37d)$$

$$\delta {}_0\tilde{\eta}_{st} = \delta \mathbf{U}^T [\frac{1}{2}\tilde{\mathbf{B}}_s^T \tilde{\mathbf{B}}_t + \frac{1}{2}\tilde{\mathbf{B}}_t^T \tilde{\mathbf{B}}_s + \tilde{\mathbf{B}}_{st}^2 + \tilde{\mathbf{B}}_{ts}^2] \mathbf{U}. \quad (3.37e)$$

Eq.3.37 is used to construct the nonlinear incremental strains at the sampling points in the assumed strain formulation.

### 3.3 Formulation of the Mixed-Interpolated Shell Element

To avoid membrane-locking problem in the case of the displacement-based shell element, a mixed-interpolated 9-node shell element based on the independent interpolation of strains is presented. The displacements are interpolated using 8-node interpolation functions, whereas the rotations are interpolated using 9-node interpolation functions where the interpolation functions,  $h_i$ , are:

$$\begin{aligned} h_1 &= \frac{1}{4}(1+r)(1+s) - \frac{1}{2}(h_5 + h_8) - \frac{1}{4}h_9 \\ h_2 &= \frac{1}{4}(1-r)(1+s) - \frac{1}{2}(h_5 + h_6) - \frac{1}{4}h_9 \\ h_3 &= \frac{1}{4}(1-r)(1-s) - \frac{1}{2}(h_6 + h_7) - \frac{1}{4}h_9 \\ h_4 &= \frac{1}{4}(1+r)(1-s) - \frac{1}{2}(h_7 + h_8) - \frac{1}{4}h_9 \\ h_5 &= \frac{1}{4}(1-r^2)(1+s) - \frac{1}{2}h_9 \\ h_6 &= \frac{1}{4}(1-s^2)(1-r) - \frac{1}{2}h_9 \end{aligned} \quad (3.38)$$

$$\begin{aligned}
h_7 &= \frac{1}{4}(1-r^2)(1-s) - \frac{1}{2}h_9 \\
h_8 &= \frac{1}{4}(1-s^2)(1+r) - \frac{1}{2}h_9 \\
h_9 &= (1-r^2)(1-s^2)
\end{aligned}$$

where the term  $h_9$  is included only when Eq. 3.38 is used for the nine node interpolation.

To avoid membrane and shear locking of the displacement-based shell element, the in-layer strains are interpolated in addition to the shear strains. Then, the coefficients in these interpolations are tied to the strain components evaluated directly from the displacement interpolations given in Eqs 3.31 and 3.37 at the sampling points. The in-layer strain interpolation yields the membrane and bending action of the element, and the transverse shear strain interpolation gives the transverse shear action. To obtain a general shell element, we interpolate the strain tensor expressed in terms of covariant components and contravariant base vectors.

In the following formulation of an assumed strain field, the element strain tensor at any time during the response history is considered; therefore, the left superscript denoting time is omitted for notational simplicity (e.g. henceforth  $\mathbf{g}_r \equiv {}^t\mathbf{g}_r$  in the case of a total Lagrangian formulation).

The strain tensor at any point in the element is,

$$\begin{aligned}
\boldsymbol{\varepsilon} &= \underbrace{\tilde{\varepsilon}_{rr}\mathbf{g}^r\mathbf{g}^r + \tilde{\varepsilon}_{ss}\mathbf{g}^s\mathbf{g}^s + \tilde{\varepsilon}_{rs}(\mathbf{g}^r\mathbf{g}^s + \mathbf{g}^s\mathbf{g}^r)}_{\text{in-layer strains}} \\
&+ \underbrace{\tilde{\varepsilon}_{rt}(\mathbf{g}^r\mathbf{g}^t + \mathbf{g}^t\mathbf{g}^r) + \tilde{\varepsilon}_{st}(\mathbf{g}^s\mathbf{g}^t + \mathbf{g}^t\mathbf{g}^s)}_{\text{transverse shear strains}}. \tag{3.39}
\end{aligned}$$

The key aspect of this element formulation is the appropriate interpolation of the in-layer strains and the transverse shear strains to satisfy basic shell element requirements as closely as possible.

### 3.3.1 In-Layer Strain Interpolation

To avoid membrane locking and to have no spurious zero energy modes, the following in-layer strain interpolation is used (see Fig. 3-3),

$$\underline{\varepsilon} = \sum_{i=1}^8 h_i^{IS} \underline{\varepsilon}|_i \quad (3.40)$$

where the  $h_i^{IS}$  are obtained from the  $h_i$  in Eq. 3.38 for the 8-node interpolation by replacing the variable  $r$  with  $r/a$ , and the variable  $s$  with  $s/a$ ,  $a = 1/\sqrt{3}$ . Also, for  $i = 1, 2, 3$  and 4 (see Fig. 3-3a),

$$\underline{\varepsilon}|_i = \tilde{\varepsilon}_{rr} \mathbf{g}^r \mathbf{g}^r|_i^{DI} + \tilde{\varepsilon}_{ss} \mathbf{g}^s \mathbf{g}^s|_i^{DI} + \tilde{\varepsilon}_{rs} (\mathbf{g}^r \mathbf{g}^s + \mathbf{g}^s \mathbf{g}^r)|_i^{DI}. \quad (3.41)$$

For  $i = 5$  and 7,

$$\begin{aligned} \underline{\varepsilon}|_5 &= \tilde{\varepsilon}_{ss} \bar{\mathbf{g}}^s \bar{\mathbf{g}}^s|_5^{DI} + \frac{1}{2} [\bar{\mathbf{g}}_r \cdot \{\underline{\varepsilon}|_1^{DI} + \underline{\varepsilon}|_2^{DI}\} \cdot \bar{\mathbf{g}}_r] \bar{\mathbf{g}}^r \bar{\mathbf{g}}^r|_5^{DI} \\ &\quad + \frac{1}{2} [\bar{\mathbf{g}}_r \cdot \{\underline{\varepsilon}|_1^{DI} + \underline{\varepsilon}|_2^{DI}\} \cdot \bar{\mathbf{g}}_s] (\bar{\mathbf{g}}^r \bar{\mathbf{g}}^s + \bar{\mathbf{g}}^s \bar{\mathbf{g}}^r)|_5^{DI} \end{aligned} \quad (3.42)$$

$$\begin{aligned} \underline{\varepsilon}|_7 &= \tilde{\varepsilon}_{ss} \bar{\mathbf{g}}^s \bar{\mathbf{g}}^s|_7^{DI} + \frac{1}{2} [\bar{\mathbf{g}}_r \cdot \{\underline{\varepsilon}|_3^{DI} + \underline{\varepsilon}|_4^{DI}\} \cdot \bar{\mathbf{g}}_r] \bar{\mathbf{g}}^r \bar{\mathbf{g}}^r|_7^{DI} \\ &\quad + \frac{1}{2} [\bar{\mathbf{g}}_r \cdot \{\underline{\varepsilon}|_3^{DI} + \underline{\varepsilon}|_4^{DI}\} \cdot \bar{\mathbf{g}}_s] (\bar{\mathbf{g}}^r \bar{\mathbf{g}}^s + \bar{\mathbf{g}}^s \bar{\mathbf{g}}^r)|_7^{DI} \end{aligned} \quad (3.43)$$

where,

$$\bar{\mathbf{g}}_s \equiv \mathbf{g}_s \quad (3.44a)$$

$$\bar{\mathbf{g}}_t \equiv \mathbf{g}_t \quad (3.44b)$$

$$\bar{\mathbf{g}}_r = \mathbf{g}_r - \alpha \mathbf{g}_s; \quad \alpha = \frac{g_{rs}}{g_{ss}}. \quad (3.44c)$$

For  $i = 6$  and 8, in Eq. 3.40,

$$\underline{\varepsilon}|_6 = \tilde{\varepsilon}_{rr} \bar{\mathbf{g}}^r \bar{\mathbf{g}}^r|_6^{DI} + \frac{1}{2} [\bar{\mathbf{g}}_s \cdot \{\underline{\varepsilon}|_2^{DI} + \underline{\varepsilon}|_3^{DI}\} \cdot \bar{\mathbf{g}}_s] \bar{\mathbf{g}}^s \bar{\mathbf{g}}^s|_6^{DI}$$

$$+ \frac{1}{2} \left[ \bar{\mathbf{g}}_r \cdot \{ \underline{\varepsilon}|_2^{DI} + \underline{\varepsilon}|_3^{DI} \} \cdot \bar{\mathbf{g}}_s \right] (\bar{\mathbf{g}}^r \bar{\mathbf{g}}^s + \bar{\mathbf{g}}^s \bar{\mathbf{g}}^r)|_6^{DI} \quad (3.45)$$

$$\begin{aligned} \underline{\varepsilon}|_8 = \tilde{\varepsilon}_{rr} \bar{\mathbf{g}}^r \bar{\mathbf{g}}^r|_8^{DI} &+ \frac{1}{2} \left[ \bar{\mathbf{g}}_s \cdot \{ \underline{\varepsilon}|_1^{DI} + \underline{\varepsilon}|_4^{DI} \} \cdot \bar{\mathbf{g}}_s \right] \bar{\mathbf{g}}^s \bar{\mathbf{g}}^s|_8^{DI} \\ &+ \frac{1}{2} \left[ \bar{\mathbf{g}}_r \cdot \{ \underline{\varepsilon}|_1^{DI} + \underline{\varepsilon}|_4^{DI} \} \cdot \bar{\mathbf{g}}_s \right] (\bar{\mathbf{g}}^r \bar{\mathbf{g}}^s + \bar{\mathbf{g}}^s \bar{\mathbf{g}}^r)|_8^{DI} \end{aligned} \quad (3.46)$$

where

$$\bar{\mathbf{g}}_r \equiv \mathbf{g}_r \quad (3.47a)$$

$$\bar{\mathbf{g}}_t \equiv \mathbf{g}_t \quad (3.47b)$$

$$\bar{\mathbf{g}}_s = \mathbf{g}_s - \beta \mathbf{g}_r; \quad \beta = \frac{g_{rs}}{g_{rr}}. \quad (3.47c)$$

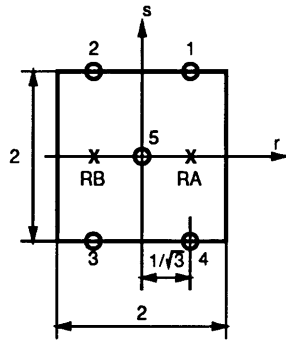
### 3.3.2 Transverse Shear Strain Interpolation

The transverse shear strain interpolation is selected to avoid shear locking and, as for the in-layer strain interpolation, no spurious zero energy mode must be introduced. The transverse shear strain interpolation selected for the shell is a generalization of the shear strain field used for the plate formulation using the covariant components and the contravariant base vectors. The following interpolation for  $\tilde{\varepsilon}_{rt} \mathbf{g}^r \mathbf{g}^t$  (see Fig. 3-3b) is used,

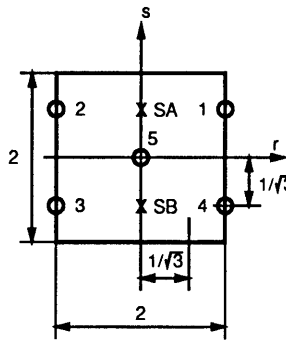
$$\tilde{\varepsilon}_{rt} \mathbf{g}^r \mathbf{g}^t = \sum_i^4 h_i^{RT} \tilde{\varepsilon}_{rt} \mathbf{g}^r \mathbf{g}^t|_i^{DI} + h_5^{RT} \left[ \frac{1}{2} (\tilde{\varepsilon}_{rt}|_{RA}^{DI} + \tilde{\varepsilon}_{rt}|_{RB}^{DI}) \right] \mathbf{g}^r \mathbf{g}^t|_5^{DI} \quad (3.48)$$

where,

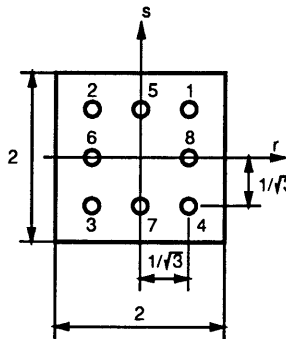
$$\begin{aligned} h_1^{RT} &= \frac{1}{4} \left( 1 + \frac{r}{a} \right) (1 + s) - \frac{1}{4} h_5^{RT} \\ h_2^{RT} &= \frac{1}{4} \left( 1 - \frac{r}{a} \right) (1 + s) - \frac{1}{4} h_5^{RT} \\ h_3^{RT} &= \frac{1}{4} \left( 1 - \frac{r}{a} \right) (1 - s) - \frac{1}{4} h_5^{RT} \\ h_4^{RT} &= \frac{1}{4} \left( 1 + \frac{r}{a} \right) (1 - s) - \frac{1}{4} h_5^{RT} \end{aligned} \quad (3.49)$$



(a) Points used for interpolation of transverse shear strain  $\tilde{\epsilon}_{rt}$



(b) Points used for interpolation of transverse shear strain  $\tilde{\epsilon}_{st}$



(c) Points used for interpolation of in-layer strains  $\tilde{\epsilon}_{rr}$ ,  $\tilde{\epsilon}_{ss}$ ,  $\tilde{\epsilon}_{rs}$

Figure 3-3: Sampling points used for the MITC9 and MITC8<sup>N</sup> shell elements.



$$h_5^{RT} = \begin{cases} (1 - (\frac{r}{a})^2)(1 - s^2) & \text{for the MITC8 element} \\ (1 - s^2) & \text{for the MITC8}^N \text{ and MITC9 elements} \end{cases}$$

where  $a = 1/\sqrt{3}$ . Here an improvement in the 8-node mixed-interpolated shell element (referred to as the MITC8<sup>N</sup> element) is introduced. The difference between the MITC8 and the MITC8<sup>N</sup> elements is in the choice of the assumed shear strain field. The differences are discussed in more detail in the next chapter. Note that in Eq. 3.48  $\tilde{\epsilon}_{rt}|_5^{DI}$  was replaced with the mean of the components at points  $RA$  and  $RB$ .

Similarly, the following interpolation for  $\tilde{\epsilon}_{st}\mathbf{g}^s\mathbf{g}^t$  (see Fig. 3-3c) is used,

$$\tilde{\epsilon}_{st}\mathbf{g}^s\mathbf{g}^t = \sum_i^4 h_i^{ST} \tilde{\epsilon}_{st}\mathbf{g}^s\mathbf{g}^t|_i^{DI} + h_5^{ST} \left[ \frac{1}{2}(\tilde{\epsilon}_{st}|_{SA}^{DI} + \tilde{\epsilon}_{st}|_{SB}^{DI}) \right] \mathbf{g}^s\mathbf{g}^t|_5^{DI} \quad (3.50)$$

where

$$\begin{aligned} h_1^{ST} &= \frac{1}{4}(1+r)(1+\frac{s}{a}) - \frac{1}{4}h_5^{ST} \\ h_2^{ST} &= \frac{1}{4}(1-r)(1+\frac{s}{a}) - \frac{1}{4}h_5^{ST} \\ h_3^{ST} &= \frac{1}{4}(1-r)(1-\frac{s}{a}) - \frac{1}{4}h_5^{ST} \\ h_4^{ST} &= \frac{1}{4}(1+r)(1-\frac{s}{a}) - \frac{1}{4}h_5^{ST} \\ h_5^{ST} &= \begin{cases} (1-r^2)(1-(\frac{s}{a})^2) & \text{for the MITC8 element} \\ (1-r^2) & \text{for the MITC8}^N \text{ and MITC9 elements} \end{cases} \end{aligned} \quad (3.51)$$

where  $a = 1/\sqrt{3}$ .

### 3.4 Tying Scheme for Shell Element

The tying of transverse shear strains used in Sec. 3.3 is based on the point tying at the center point. In this section, possible alternatives in the tying of transverse shear strains are suggested and discussed. In the discussion only the  $\tilde{\epsilon}_{rt}$  component of shear strains is considered since the strains  $\tilde{\epsilon}_{rt}$  and  $\tilde{\epsilon}_{st}$  are symmetric in  $r$  and  $s$ .

In the interpolation of shear strains, the relationship between  $\tilde{\varepsilon}_{rt}|^{DI}$  and  $\tilde{\varepsilon}_{rt}|^{AS}$  needs to be identified in terms of five unknown constants in  $\tilde{\varepsilon}_{rt}|^{AS}$ . Equation 2.43 is used in the shell element formulation as well to get four equations of tying. After imposition of the requirements for tying along the edges of the element, the  $\tilde{\varepsilon}_{rt}|^{AS}$  term is expressed as,

$$\tilde{\varepsilon}_{rt}(\mathbf{g}^r \mathbf{g}^t + \mathbf{g}^t \mathbf{g}^r)|^{AS} = \sum_{i=1}^4 h_i^{RT} (\mathbf{g}^r \mathbf{g}^t + \mathbf{g}^t \mathbf{g}^r)|_i + h_5^{RT} \underline{\varepsilon}|^I \quad (3.52)$$

where  $\underline{\varepsilon}|^I$  is an unknown constant tensor to be determined. It is desirable to construct the tying scheme for the shell element which reduces to Eq. 2.44 when the element is in the flat plate condition. Hence as a first attempt, Eq. 3.52 may be numerically integrated and equated with the integral of the directly interpolated strains. Namely,

$$\int_V \underline{\varepsilon}|^{AS} dV = \int_V \underline{\varepsilon}|^{DI} dV \quad (3.53)$$

or using Eq. 3.52,

$$\int_V \sum_{i=1}^4 h_i^{RT} \tilde{\varepsilon}_{rt}(\mathbf{g}^r \mathbf{g}^t + \mathbf{g}^t \mathbf{g}^r)|_i + \int_V h_5^{RT} \underline{\varepsilon}|^I = \int_V \tilde{\varepsilon}_{rt} \mathbf{g}^r \mathbf{g}^t + \mathbf{g}^t \mathbf{g}^r |^{DI} dV. \quad (3.54)$$

Solving Eq. 3.54 for  $\underline{\varepsilon}|^I$ ,

$$\underline{\varepsilon}|^I = \frac{1}{\int_V h_5^{RT} dV} \left[ \sum_{j=1}^{ipt} \tilde{\varepsilon}_{rt}(\mathbf{g}^r \mathbf{g}^t + \mathbf{g}^t \mathbf{g}^r)|_j^{DI} - \sum_{i=1}^4 \left\{ \int_V h_i^{RT} dV \right\} \tilde{\varepsilon}_{rt}(\mathbf{g}^r \mathbf{g}^t + \mathbf{g}^t \mathbf{g}^r)|_i \right] \quad (3.55)$$

is obtained where the first summation runs over the integration point (up to *ipt*) for numerical integration (See Fig. 3-4). For full integral tying, the strains in Eq. 3.55 need to be numerically integrated with  $3 \times 3$  Gauss points (See Fig. 3-4a). This formulation gives full integral tying and the scheme reduces precisely to Eq. 2.44 when the element is in the flat plate condition. Though full integral tying satisfies the mathematical requirement, the scheme requires additional nine points in the expression of assumed strain field which makes the practical implementations complicated and numerically inefficient in the shell

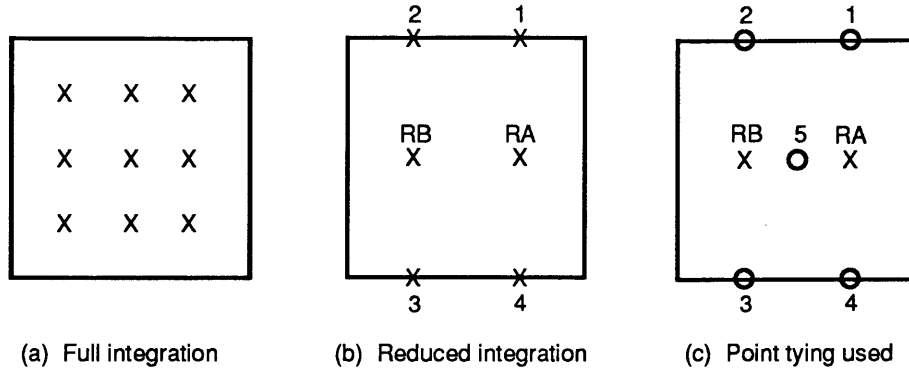


Figure 3-4: Reduced integration for integral tying.

element formulation. Recall also that the plate element using full integral tying does not pass the bending patch test exactly.

To simplify the numerical integration in Eq. 3.55 without loss of accuracy, a reduced integration can be used in Eq. 3.54 (*i.e.* use a reduced number of points in the first summation of Eq. 3.55). Since we are interested in reducing the number of additional sampling points, it is tempting to use the points illustrated in Fig. 3-4b. As shown in Fig. 3-4b, the reduced integral tying scheme uses

- 2-point Gauss integration in the  $r$  direction. (accuracy order 3)
- 3-point Newton-Cote integration in the  $s$  direction. (accuracy order 2)

In this case only two additional sampling points are needed since the value of the strains at points on the edges (points 1 through 4) are already evaluated for the imposition of Eq. 2.43. Using this reduced integral tying scheme, Eq. 3.55 can be rewritten,

$$\begin{aligned} \varepsilon|^{I} = \frac{1}{\int_V h_5^{RT} dV} & \left[ w_{RA} \tilde{\varepsilon}_{rt}(\mathbf{g}^r \mathbf{g}^t + \mathbf{g}^t \mathbf{g}^r)|^{RA} + w_{RB} \tilde{\varepsilon}_{rt}(\mathbf{g}^r \mathbf{g}^t + \mathbf{g}^t \mathbf{g}^r)|^{RB} \right. \\ & - \frac{1}{4} w_{RA} \left\{ \tilde{\varepsilon}_{rt}(\mathbf{g}^r \mathbf{g}^t + \mathbf{g}^t \mathbf{g}^r)|^1 - \tilde{\varepsilon}_{rt}(\mathbf{g}^r \mathbf{g}^t + \mathbf{g}^t \mathbf{g}^r)|^2 \right\} \\ & - \frac{1}{4} w_{RA} \left\{ \tilde{\varepsilon}_{rt}(\mathbf{g}^r \mathbf{g}^t + \mathbf{g}^t \mathbf{g}^r)|^4 - \tilde{\varepsilon}_{rt}(\mathbf{g}^r \mathbf{g}^t + \mathbf{g}^t \mathbf{g}^r)|^3 \right\} \\ & - \frac{1}{4} w_{RB} \left\{ \tilde{\varepsilon}_{rt}(\mathbf{g}^r \mathbf{g}^t + \mathbf{g}^t \mathbf{g}^r)|^2 - \tilde{\varepsilon}_{rt}(\mathbf{g}^r \mathbf{g}^t + \mathbf{g}^t \mathbf{g}^r)|^1 \right\} \end{aligned}$$

$$- \frac{1}{4} w_{RB} \left\{ \tilde{\varepsilon}_{rt}(\mathbf{g}^r \mathbf{g}^t + \mathbf{g}^t \mathbf{g}^r)|^3 - \tilde{\varepsilon}_{rt}(\mathbf{g}^r \mathbf{g}^t + \mathbf{g}^t \mathbf{g}^r)|^4 \right\} \quad (3.56)$$

where  $w_i$  is the weight of the numerical integration at integration point  $i$  multiplied by the value of the Jacobian determinant. The tying based on reduced integration simulates the full integral tying with only two additional sampling points. The numerical results obtained using the full integral tying and the reduced integral tying show very little difference in the case of the plate analysis. It is tempting to use the tying given in Eq. 3.56 for shell element formulation since the integral tying is one of the mathematical requirements in the plate formulation. However, as in the case of full integral tying, the element with reduced integral tying fails the bending patch test. Since the mathematical analysis for optimal convergence in Sec. 2.1 is for the limiting case when the thickness approaches zero, similar behavior for thin plate conditions can be expected.

From an engineering point of view it is desirable to design an element which passes the necessary patch tests. In order to design an element which passes the patch test, consider applying Eq. 3.56 to a case where the element is in flat rectangular shape. In this special geometry,

$$w_{RA} = w_{RB} \quad (3.57a)$$

$$\int_V h_5^{RT} dV = w_{RA} + w_{RB} \quad (3.57b)$$

$$\mathbf{g}^r \mathbf{g}^t|^{RA} = \mathbf{g}^r \mathbf{g}^t|^{RB} = \mathbf{g}^r \mathbf{g}^t|_5. \quad (3.57c)$$

Using Eq. 3.57 in 3.56,

$$\underline{\varepsilon}|^I = h_5^{RT} \left[ \frac{1}{2} (\tilde{\varepsilon}_{rt}|_{RA}^{DI} + \tilde{\varepsilon}_{rt}|_{RB}^{DI}) \right] \mathbf{g}^r \mathbf{g}^t|_5^{DI} \quad (3.58)$$

which is precisely the last term in Eq. 3.48. Hence the reduced integral tying in Eq. 3.56 reduces to point tying used in the MITC8<sup>N</sup> and MITC9 shell elements. Notice also that the full integral tying reduces to point tying for rectangular elements (See appendix A.1). In summary, full integral tying, reduced integral tying, and point tying are all identical

for the flat rectangular elements.

The point tying used in Eq. 3.48 is based on the conditions in Eq. 3.57. These conditions do not hold for the non-rectangular element. By assuming the condition in Eq. 3.57 for non-rectangular geometry as well (hence neglecting the geometry distortion effect in the reduced integration of tying constraint), the element using Eq. 3.48, which passes the bending patch test can be obtained. Notice that the point tying scheme is not totally new but it is derived from Eq. 3.56 with a further reduction in integration. Thus, one of the mathematical requirements is violated slightly to obtain the element which satisfies the engineering requirement (patch test).

### 3.5 Incremental Formulation

In general, a large deformation analysis requires a step-by-step incremental solution. The basic continuum mechanics equation in this solution is the linearized incremental form of the principle of virtual work. For the equilibrium configuration at time  $t + \Delta t$  (the one being sought), the principle of virtual work [Bathe, 1982] states that

$$\int_{^0V} {}^{t+\Delta t} \tilde{S}^{ij} \delta {}^{t+\Delta t} \tilde{\varepsilon}_{ij} {}^0 dV = {}^{t+\Delta t} \mathcal{R} \quad (3.59)$$

where  ${}^0V$  is the volume in the initial configuration ( $t = 0$ ),  ${}^{t+\Delta t} \tilde{S}^{ij}$  are the contravariant components of the 2nd Piola-Kirchhoff stress tensor measured in the convected system and  ${}^{t+\Delta t} \mathcal{R}$  is the virtual work of the external loads acting on the configuration at time  $t + \Delta t$ .

After the linearization of Eq. 3.59, and using the kinematic equations for strains, the incremental total Lagrangian Formulation for the shell element can be developed.

With the Newton-Raphson iteration scheme, the equations for the  $i$ -th iteration in a finite elements model are,

$$({}^{t+\Delta t} {}^0 \mathbf{K}_L + {}^{t+\Delta t} {}^0 \mathbf{K}_{NL})^{(i-1)} \Delta \mathbf{U}^{(i)} = {}^{t+\Delta t} \mathbf{P} - {}^t \mathbf{F}^{(i-1)}. \quad (3.60)$$

For the displacement,

$$\mathbf{U}^{(i)} = \mathbf{U}^{(i-1)} + \Delta\mathbf{U}^{(i)} \quad (3.61)$$

and for the rotations,

$$({}^{t+\Delta t}{}^i\mathbf{R}^k)^{(i)} = (\Delta {}^{t+\Delta t}{}^i\mathbf{R}^k)^i ({}^{t+\Delta t}{}^i\mathbf{R}^k)^{(i-1)}. \quad (3.62)$$

In the equations above,

${}^{t+\Delta t}{}^0\mathbf{K}_L$  is the linear part of the tangent stiffness matrix,

${}^{t+\Delta t}{}^0\mathbf{K}_{NL}$  is the nonlinear part of the tangent stiffness matrix,

$\mathbf{U}$  is the vector of generalized nodal incremental displacement,

${}^{t+\Delta t}\mathbf{P}$  is the vector of generalized external nodal loads acting at  $t + \Delta t$ ,

and

${}^t\mathbf{F}$  is the vector of generalized internal nodal loads acting at  $t + \Delta t$ , equivalent (in the virtual work sense) to the element stresses.

# Chapter 4

## Analysis of the Mixed-Interpolated Shell Element

In this chapter, an analysis of the mixed-interpolated shell element is presented. The purpose of this study is to gain insight into the interpolation scheme for the strain fields. Since the shear strain interpolations have already been discussed in Chapter 2, this chapter will focus on the in-plane strain interpolations. The behavior of the improved 8-node shell element introduced in Chapter 3 is discussed further. Finally, an efficient computational scheme is proposed and studied in terms of computational efficiency.

### 4.1 Covariant Strain Interpolation and Its Analysis

The behavior of covariant strains used in the mixed-interpolated shell elements is examined, and an example of a square plate is given to show how the in-plane strains are calculated in the element.

### 4.1.1 Covariant Strain in a One-Dimensional Bar

In this subsection, a simple example is carried out to demonstrate how the covariant strains in an element are calculated. The calculated covariant strains are then compared to the Green-Lagrange strain components obtained using the conventional formula. The calculation of the incremental strains using the total Lagrangian formulation was given in Sec. 3.2. Equation 3.27 is rewritten below for convenience.

$${}^0\epsilon = \frac{1}{2} \left[ \frac{\partial \mathbf{u}}{\partial r_i} \cdot {}^t\mathbf{g}_j + {}^t\mathbf{g}_j \cdot \frac{\partial \mathbf{u}}{\partial r_j} + \frac{\partial \mathbf{u}}{\partial r_i} \cdot \frac{\partial \mathbf{u}}{\partial r_j} \right] {}^0\mathbf{g}^i {}^0\mathbf{g}^j \quad (4.1)$$

A similar expression can be obtained for the updated Lagrangian formulation as well by using the procedure outlined in Sec. 3.2,

$$\begin{aligned} {}^t\epsilon &= \left[ {}^{t+\Delta t}{}^t\tilde{\epsilon}_{ij} - {}^t\tilde{\epsilon}_{ij} \right] {}^t\mathbf{g}^i {}^t\mathbf{g}^j \\ &= \frac{1}{2} \left[ {}^{t+\Delta t}\mathbf{g}_i \cdot {}^{t+\Delta t}\mathbf{g}_j - {}^t\mathbf{g}_i \cdot {}^t\mathbf{g}_j \right] {}^t\mathbf{g}^i {}^t\mathbf{g}^j \\ &= \frac{1}{2} \left[ \frac{\partial \mathbf{u}}{\partial r_i} \cdot {}^t\mathbf{g}_j + {}^t\mathbf{g}_j \cdot \frac{\partial \mathbf{u}}{\partial r_j} + \frac{\partial \mathbf{u}}{\partial r_i} \cdot \frac{\partial \mathbf{u}}{\partial r_j} \right] {}^t\mathbf{g}^i {}^t\mathbf{g}^j. \end{aligned} \quad (4.2)$$

The following comparisons can be made between Eqs. 4.1 and 4.2:

- The components of the strains are identical in the total Lagrangian and updated Lagrangian formulations,

$${}^0\tilde{\epsilon}_{ij} = {}^t\tilde{\epsilon}_{ij}. \quad (4.3)$$

Notice, however, that the base vectors in each formulation are different,

$${}^0\epsilon = {}^0\tilde{\epsilon}_{ij} {}^0\mathbf{g}^i {}^0\mathbf{g}^j \neq {}^t\tilde{\epsilon}_{ij} {}^t\mathbf{g}^i {}^t\mathbf{g}^j = {}^t\epsilon. \quad (4.4)$$

- In the total Lagrangian formulation, the initial displacement effects are accounted for via the base vectors, i.e.  ${}^0\mathbf{g}^i {}^0\mathbf{g}^j$  contains the initial displacement effects.

Hence, in the covariant strain calculation, the base vectors (in which each component



is measured) are as important as the components themselves. Therefore the assumed covariant strains need to be interpolated along with the base vectors in the mixed-formulation.

To obtain the components with respect to a different coordinate system, a second order tensor transformation should be used. For example, to get the global Cartesian components,

$$\tilde{\varepsilon}_{ij} \mathbf{g}^i \mathbf{g}^j = \varepsilon_{kl} \hat{\mathbf{e}}_k \hat{\mathbf{e}}_l \quad (4.5)$$

or

$$\varepsilon_{kl} = (\tilde{\varepsilon}_{ij})(\hat{\mathbf{e}}_k \cdot \mathbf{g}^i)(\mathbf{g}^j \cdot \hat{\mathbf{e}}_l) \quad (4.6)$$

should be used where  $\varepsilon_{kl}$  is the component of the strain tensor measured in the global Cartesian coordinate system.

A familiar expression of the Green-Lagrange strain component in the global Cartesian system is

$${}^t_0\varepsilon_{kl} = \frac{1}{2} \left[ {}^t_0u_{k,l} + {}^t_0u_{l,k} + {}^t_0u_{m,k} {}^t_0u_{m,l} \right], \quad (4.7)$$

from which, the following two expressions can be derived:

$${}_0\varepsilon_{kl} = \frac{1}{2} ({}_0u_{k,l} + {}_0u_{l,k} + {}^t_0u_{m,k} {}_0u_{m,l} + {}_0u_{m,k} {}^t_0u_{m,l} + {}_0u_{m,k} {}_0u_{m,l}) \quad (4.8a)$$

$${}^t\varepsilon_{kl} = \frac{1}{2} ({}^t u_{k,l} + {}^t u_{l,k} + {}^t u_{m,k} {}^t u_{m,l}). \quad (4.8b)$$

It can be shown without further elaboration that the expressions for the strain components in Eqs. 4.6 and 4.8 are identical.

In the next example a 1-D truss element is investigated. The configurations for the rod under consideration are shown in Fig. 4-1 for times 0,  $t$ , and  $t + \Delta t$ .

First, consider the total Lagrangian formulation. The only nonzero strain component of the rod is  ${}_0\varepsilon_{xx}$ , which can be expressed by using Eqs. 4.1 and 4.6 as follows:

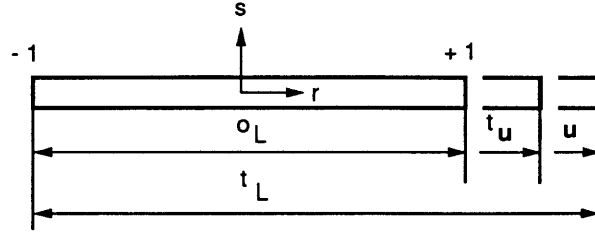


Figure 4-1: Covariant strains in a truss element.

$$\begin{aligned}
{}^0\varepsilon_{xx} &= \frac{1}{2} \left[ \frac{\partial \mathbf{u}}{\partial r} \cdot {}^t\mathbf{g}_r + {}^t\mathbf{g}_r \cdot \frac{\partial \mathbf{u}}{\partial r} + \frac{\partial \mathbf{u}}{\partial r} \cdot \frac{\partial \mathbf{u}}{\partial r} \right] ({}^0\mathbf{g}^r \cdot \hat{\mathbf{e}}_x) ({}^0\mathbf{g}^r \cdot \hat{\mathbf{e}}_x) \\
&= \frac{1}{2} \left[ \frac{u}{{}^0L} \frac{{}^tL}{{}^0L} + \frac{{}^tL}{2} \frac{u}{{}^0L} + \frac{u}{2} \frac{u}{{}^0L} \right] \left( \frac{2}{{}^0L} \right) \left( \frac{2}{{}^0L} \right) \\
&= \frac{{}^tLu}{{}^0L^2} + \frac{1}{2} \left( \frac{u}{{}^0L} \right)^2.
\end{aligned} \tag{4.9}$$

The same expression can be obtained by using the standard notation of Eq. 4.8a,

$$\begin{aligned}
{}^0\varepsilon_{xx} &= {}^0u_{1,1} + {}^t_0u_{1,1}u_{1,1} + \frac{1}{2}({}^0u_{1,1})^2 \\
&= \frac{u}{{}^0L} + \frac{{}^tu}{{}^0L} \frac{u}{{}^0L} + \frac{1}{2} \left( \frac{u}{{}^0L} \right)^2 \\
&= \frac{{}^0Lu + ({}^tL - {}^0L)u}{{}^0L^2} + \frac{1}{2} \left( \frac{u}{{}^0L} \right)^2 \\
&= \frac{{}^tLu}{{}^0L^2} + \frac{1}{2} \left( \frac{u}{{}^0L} \right)^2.
\end{aligned} \tag{4.10}$$

Similar comparison can be made using the updated Lagrangian formulation. The only nonzero strain component in the rod is  ${}^t\varepsilon_{xx}$ , which can be expressed by using Eqs. 4.2 and 4.6 as follows:

$${}^t\varepsilon_{xx} = \frac{1}{2} \left[ \frac{\partial \mathbf{u}}{\partial r} \cdot {}^t\mathbf{g}_r + {}^t\mathbf{g}_r \cdot \frac{\partial \mathbf{u}}{\partial r} + \frac{\partial \mathbf{u}}{\partial r} \cdot \frac{\partial \mathbf{u}}{\partial r} \right] ({}^t\mathbf{g}^r \cdot \hat{\mathbf{e}}_x) ({}^t\mathbf{g}^r \cdot \hat{\mathbf{e}}_x)$$

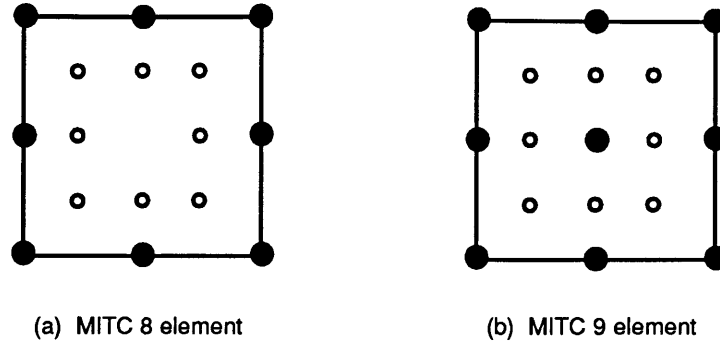


Figure 4-2: Sampling points for the membrane strain interpolation.

$$\begin{aligned}
 &= \frac{1}{2} \left[ \frac{u}{2} \frac{{}^tL}{2} + \frac{{}^tL}{2} \frac{u}{2} + \frac{u}{2} \frac{u}{2} \right] \left( \frac{2}{{}^tL} \right) \left( \frac{2}{{}^tL} \right) \\
 &= \frac{u}{{}^tL} + \frac{1}{2} \left( \frac{u}{{}^tL} \right)^2.
 \end{aligned} \tag{4.11}$$

Again, the same expression can be obtained by using the standard notation of Eq. 4.8b,

$$\begin{aligned}
 {}^t\varepsilon_{xx} &= \frac{1}{2} ({}^tu_{1,1} + {}^tu_{1,1}) + \frac{1}{2} ({}^tu_{1,1})^2 \\
 &= \frac{u}{{}^tL} + \frac{1}{2} \left( \frac{u}{{}^tL} \right)^2.
 \end{aligned} \tag{4.12}$$

### 4.1.2 Covariant Strain Interpolations in a Square Plate

Consider the square plate shown in Fig. 4-2. The plate has dimensions of  $2 \times 2 \times 2$  unit length and hence, the  $r$ - $s$  isoparametric coordinate system is aligned with the global  $X$ - $Y$  coordinate system. Figure 4-2 illustrates the nodal points as well as the in-plane strain sampling points for the MITC8 and MITC9 elements. The purpose of this example is to study the in-plane strain interpolations to gain insight into the assumed strain formulation methodology. The simplicity of the geometry allows for the analytical calculation of the interpolated strains.

First, note that,

$$\mathbf{g}_r = \bar{\mathbf{g}}_r = \mathbf{g}^r = \bar{\mathbf{g}}^r = \hat{\mathbf{e}}_i \quad (4.13a)$$

$$\mathbf{g}_s = \bar{\mathbf{g}}_s = \mathbf{g}^s = \bar{\mathbf{g}}^s = \hat{\mathbf{e}}_j \quad (4.13b)$$

$$\mathbf{g}_t = \mathbf{g}^t = \hat{\mathbf{e}}_k \quad (4.13c)$$

which are constant throughout the element.

The displacements are interpolated as

$$\mathbf{u} = \begin{cases} f(1, r, s, r^2, rs, s^2, r^2s, rs^2) & \text{for the MITC8 element,} \\ f(1, r, s, r^2, rs, s^2, r^2s, rs^2, r^2s^2) & \text{for the MITC9 element.} \end{cases} \quad (4.14)$$

The directly interpolated strains can be calculated using the usual displacement-strain relationships as follows: for the MITC8 element;

$$\tilde{\epsilon}_{rr}|^{DI} = f(1, r, s, rs, s^2) \quad (4.15a)$$

$$\tilde{\epsilon}_{ss}|^{DI} = f(1, r, s, rs, r^2) \quad (4.15b)$$

$$\tilde{\epsilon}_{rs}|^{DI} = f(1, r, s, rs, r^2, s^2) \quad (4.15c)$$

and for the MITC9 element;

$$\tilde{\epsilon}_{rr}|^{DI} = f(1, r, s, rs, s^2, rs^2) \quad (4.16a)$$

$$\tilde{\epsilon}_{ss}|^{DI} = f(1, r, s, rs, r^2, r^2s) \quad (4.16b)$$

$$\tilde{\epsilon}_{rs}|^{DI} = f(1, r, s, rs, r^2, s^2, r^2s, rs^2). \quad (4.16c)$$

The assumed strains are calculated using Eq. 3.40 as follows:

$$\begin{aligned} \tilde{\epsilon}_{rr}|^{AS} &= h_1^{IS} \tilde{\epsilon}_{rr}|_1^{DI} + h_2^{IS} \tilde{\epsilon}_{rr}|_2^{DI} + h_3^{IS} \tilde{\epsilon}_{rr}|_3^{DI} + h_4^{IS} \tilde{\epsilon}_{rr}|_4^{DI} \\ &\quad + \frac{1}{2} h_5^{IS} [\tilde{\epsilon}_{rr}|_1^{DI} + \tilde{\epsilon}_{rr}|_2^{DI}] + h_6^{IS} \tilde{\epsilon}_{rr}|_6^{DI} \end{aligned}$$

$$+\frac{1}{2}h_7^{IS}[\tilde{\epsilon}_{rr}|_3^{DI} + \tilde{\epsilon}_{rr}|_4^{DI}] + h_8^{IS}\tilde{\epsilon}_{rr}|_8^{DI} \quad (4.17a)$$

$$\begin{aligned} \tilde{\epsilon}_{ss}|^{AS} &= h_1^{IS}\tilde{\epsilon}_{ss}|_1^{DI} + h_2^{IS}\tilde{\epsilon}_{ss}|_2^{DI} + h_3^{IS}\tilde{\epsilon}_{ss}|_3^{DI} + h_4^{IS}\tilde{\epsilon}_{ss}|_4^{DI} \\ &\quad + h_5^{IS}\tilde{\epsilon}_{ss}|_5^{DI} + \frac{1}{2}h_6^{IS}[\tilde{\epsilon}_{ss}|_2^{DI} + \tilde{\epsilon}_{ss}|_3^{DI}] \\ &\quad + h_7^{IS}\tilde{\epsilon}_{ss}|_7^{DI} + \frac{1}{2}h_8^{IS}[\tilde{\epsilon}_{ss}|_1^{DI} + \tilde{\epsilon}_{ss}|_4^{DI}] \end{aligned} \quad (4.17b)$$

$$\begin{aligned} \tilde{\epsilon}_{rs}|^{AS} &= h_1^{IS}\tilde{\epsilon}_{rs}|_1^{DI} + h_2^{IS}\tilde{\epsilon}_{rs}|_2^{DI} + h_3^{IS}\tilde{\epsilon}_{rs}|_3^{DI} + h_4^{IS}\tilde{\epsilon}_{rs}|_4^{DI} \\ &\quad + \frac{1}{2}h_5^{IS}[\tilde{\epsilon}_{rs}|_1^{DI} + \tilde{\epsilon}_{rs}|_2^{DI}] + \frac{1}{2}h_6^{IS}[\tilde{\epsilon}_{rs}|_2^{DI} + \tilde{\epsilon}_{rs}|_3^{DI}] \\ &\quad + \frac{1}{2}h_7^{IS}[\tilde{\epsilon}_{rs}|_3^{DI} + \tilde{\epsilon}_{rs}|_4^{DI}] + \frac{1}{2}h_8^{IS}[\tilde{\epsilon}_{rs}|_1^{DI} + \tilde{\epsilon}_{rs}|_4^{DI}]. \end{aligned} \quad (4.17c)$$

From Eq. 4.17, the assumed strain fields can be summarized as follows:

$$\tilde{\epsilon}_{rr}|^{AS} = f(1, r, s, rs, s^2) \quad (4.18a)$$

$$\tilde{\epsilon}_{ss}|^{AS} = f(1, r, s, rs, r^2) \quad (4.18b)$$

$$\tilde{\epsilon}_{rs}|^{AS} = f(1, r, s, rs). \quad (4.18c)$$

In this example, the  $\tilde{\epsilon}_{rr}|^{AS}$  component is interpolated linearly in the  $r$ -direction, and quadratically in the  $s$ -direction. The  $\tilde{\epsilon}_{ss}|^{AS}$  component is interpolated in a similar manner. In the case of the MITC8 element, it is clear that  $\tilde{\epsilon}_{rr}|^{DI} = \tilde{\epsilon}_{rr}|^{AS}$ , and  $\tilde{\epsilon}_{ss}|^{DI} = \tilde{\epsilon}_{ss}|^{AS}$ . However, the  $\tilde{\epsilon}_{rs}|^{AS}$  component is interpolated linearly in both  $r$  and  $s$  directions ( $r^2$  and  $s^2$  terms are not included in the interpolation). In the case of the MITC9 element, all three strain fields in Eq. 4.18 correspond to reduced fields compared to the directly interpolated strains of Eq. 4.16.

When the mesh is distorted, the contravariant base vectors corresponding to each strain component are no longer simple polynomials. Therefore, it is not trivial to express the interpolated strains in closed form. Further, the directions of the base vectors at midside sampling points are not aligned with the directions of base vectors at the adjacent corner sampling points. In such situation, it is necessary to transform the strain tensor at the corner sampling points into the direction of the base vectors at the midside sampling

points in order to reduce the interpolation fields of the assumed in-plane strains. This transformation is equivalent to the projection shown in Eqs.3.42 to 3.47.

## 4.2 Improvement of the Eight-Node Element

Initially, the MITC8 element [Bathe and Dvorkin, 1986] was constructed directly as a general shell element. Its development was based on physical insight and the patch test. While the MITC8 element performs well in most cases, a suitable counterpart element in the analysis of incompressible media has not yet been found. As mentioned in Chapter 2, the MITC9 element corresponds to the  $Q_2 - P_1$  element (sometimes called 9/3 element, i.e. 9 node element with 3 pressure variables) which possesses the optimal convergence characteristics. Although the 8/3 element (8-node element with 3 pressure variables) does not satisfy all the mathematical conditions for optimal convergence, it has been shown that the element performs quite well in the study of incompressible media [Sussman and Bathe, 1987].

It is possible to construct an 8-node plate element which corresponds to the 8/3 element used in the analysis of incompressible media. The element is constructed by changing the fields of shear strain interpolation as shown in Eqs. 3.49 and 3.51. The resulting 8-node element with improved characteristics is referred to as the MITC8<sup>N</sup> element. The MITC8<sup>N</sup> element does not satisfy all the mathematical requirements for optimal convergence, but is closer to the mathematically suggested element compared to the conventional MITC8 element. The differences in the predictive capabilities between the MITC8 and MITC8<sup>N</sup> elements are in general not very significant. Yet, the following two examples demonstrate the improvements in the MITC8<sup>N</sup> element.

First, consider the analysis of a circular plate shown in Fig. 2-10. A finite element mesh with 16 elements per radial line which is obtained by subdividing each element in Fig. 2-10a is used (192 elements). The plate is subjected to a uniform pressure with clamped boundary conditions along its circumference. Figure 4-3 shows the lines of

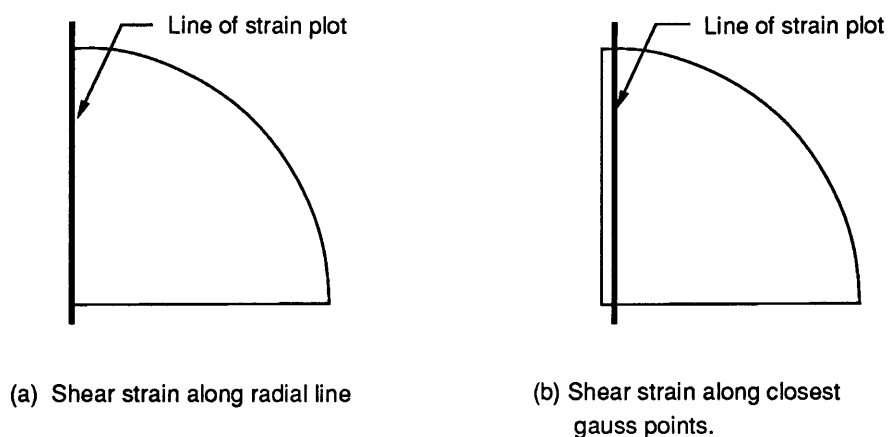
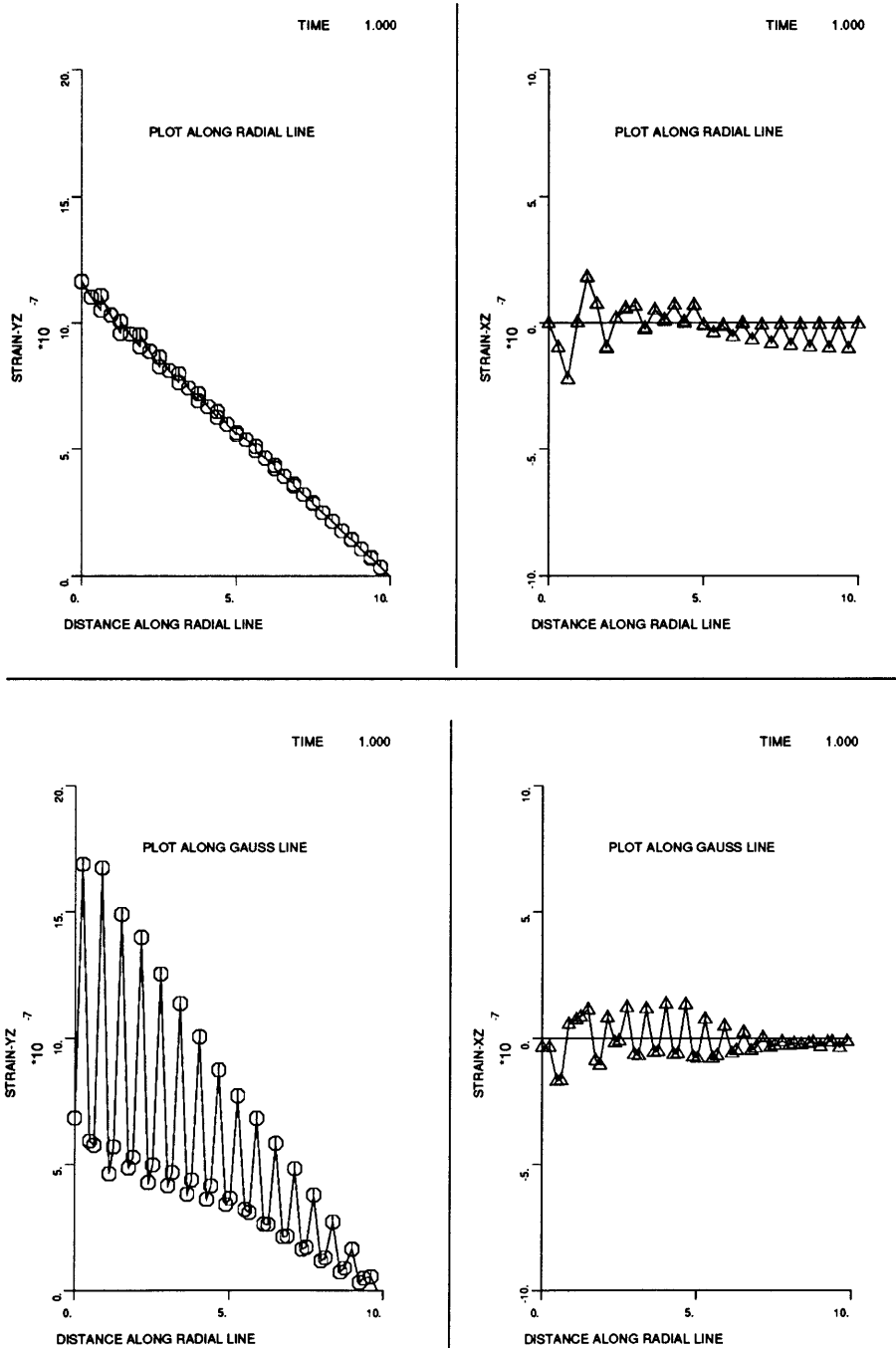


Figure 4-3: Lines of shear strain plot for a clamped circular plate under uniform pressure.  $h/D = 1/100$ . Finite element mesh used is 16 elements per radial line which is obtained by subdividing each element in Fig. 2-10a (192 elements).

interest for the shear strain plots. The shear strain variation along the radial line (Fig. 4-3a), as well as the same strain components along the Gauss integration points closest to the radial line (Fig. 4-3b) are examined. We should expect little variation in strains and in the shape of strain variation between these two lines. Figure 4-4a shows the strain plot constructed using the MITC8 element. The strain plot along the radial line shows reasonable variations in the  $yz$ -component. The  $xz$ -component strain plot along the radial line shows small oscillations. However, the  $yz$ -component plot along the Gauss line shows unreasonably large oscillations and the oscillations in the  $xz$ -component are also observed. On the average the shear strains along the Gauss line may satisfy the equilibrium condition. However, internally, they exhibit large oscillations. Figures 4-4b and 4-4c show the strain plots using the MITC8<sup>N</sup> and MITC9 elements. In both elements no oscillations are observed along both the radial and Gauss lines.

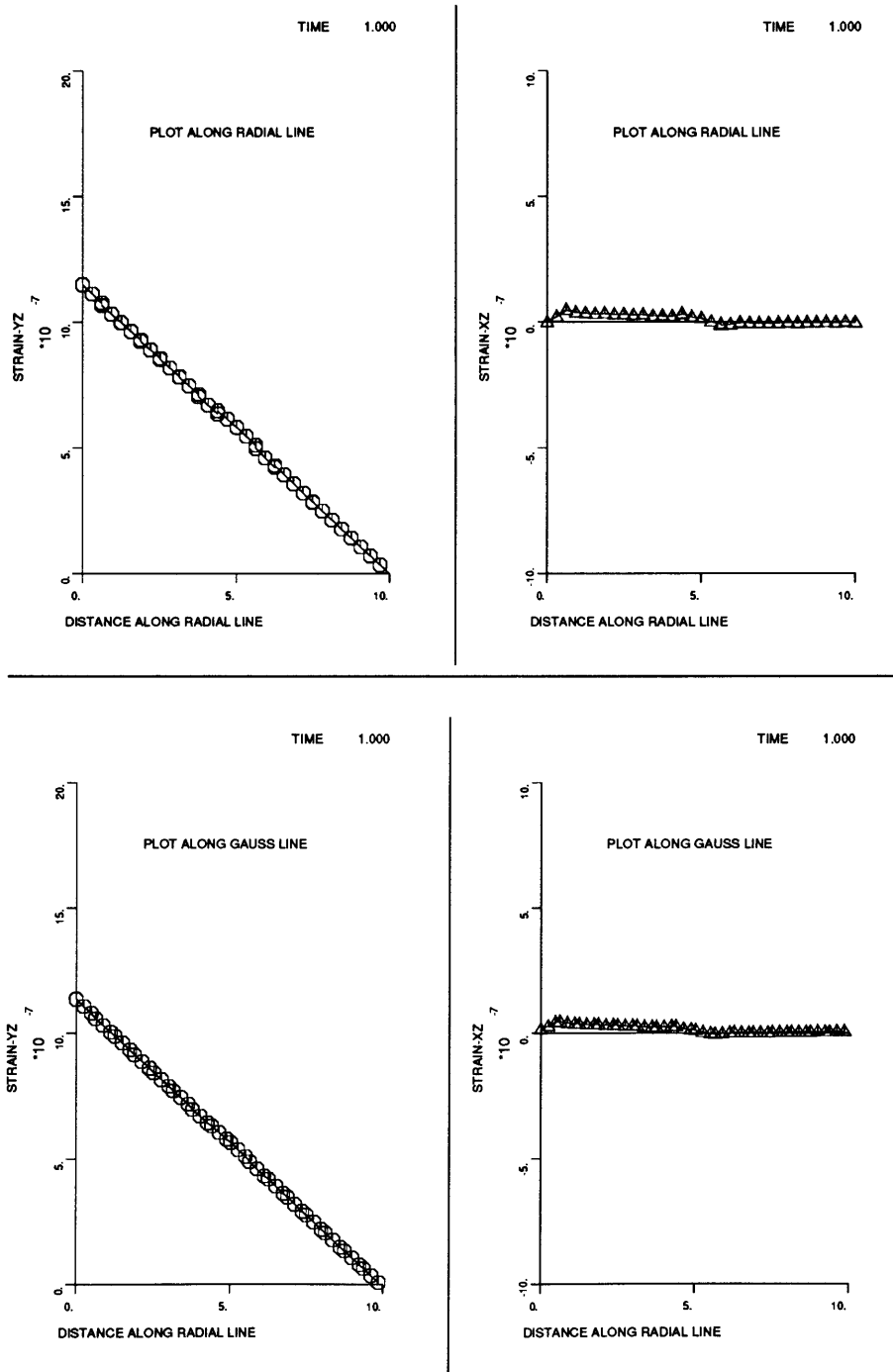
In the next example we will consider the analysis of a square plate using the graded mesh shown in Fig. 2-8. The plate is analyzed using both “soft” and “hard” boundary conditions and the shear stress along the top edge is plotted in Fig. 4-5. Notice that in this case stresses are calculated at the midside nodes as well as at the corner nodes. Figure 4-



(a) MITC8 element

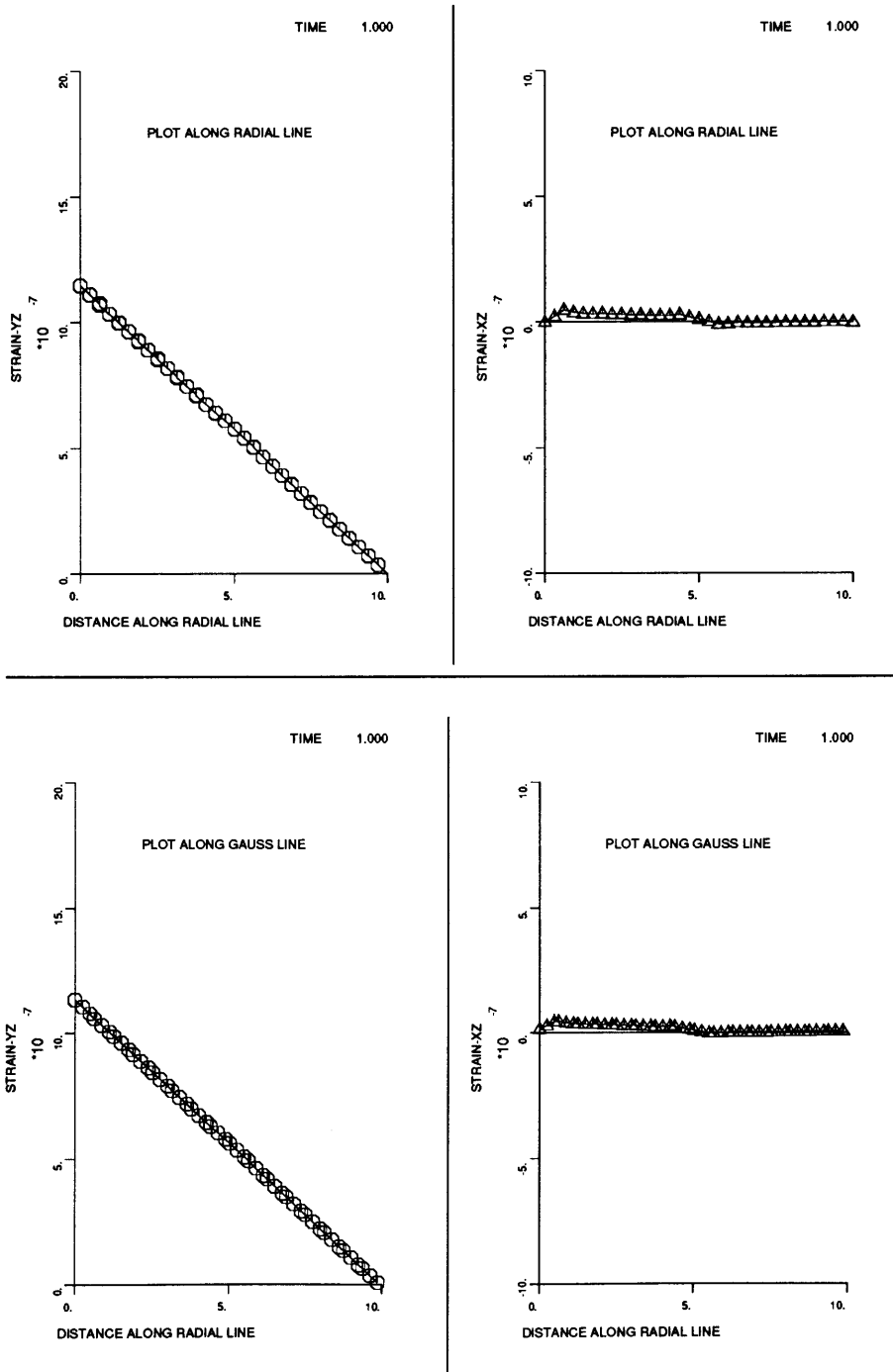
Figure 4-4: Shear strain oscillation in a circular plate.





(b) MITC8<sup>N</sup> element

Figure 4-4 Continued.



(c) MITC9 element

Figure 4-4 Continued.

5a shows that severe oscillations in shear stresses occur when the MITC8 element is used. As in the case of the previous example (circular plate), no oscillations are observed when the MITC8<sup>N</sup> and MITC9 elements are used in the shear stress plots (see Figs. 4-5b and 4-5c).

The oscillations in shear stresses result from the use of an inappropriate field in the shear strain interpolation within the MITC8 element. Recall that the fields used for shear strain interpolations are

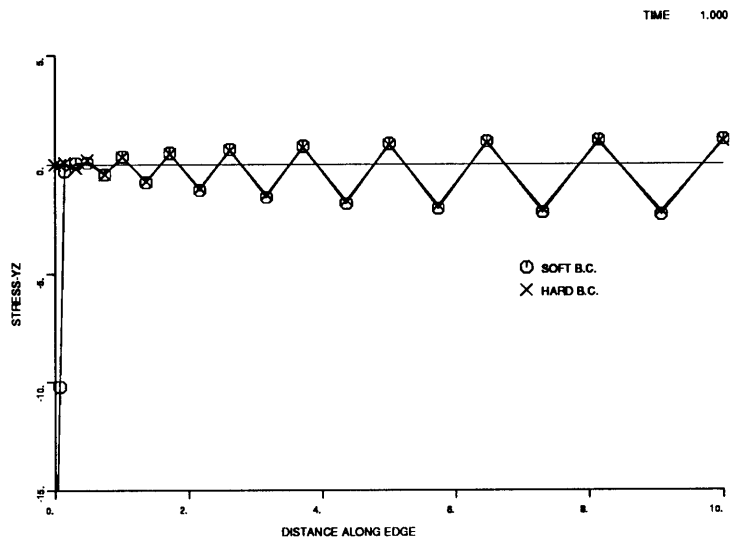
$$\tilde{\epsilon}_{rt} = \begin{cases} f(1, r, s, rs, r^2s^2) & \text{for the MITC8 element,} \\ f(1, r, s, rs, s^2) & \text{for the MITC8}^N \text{ and MITC9 elements,} \end{cases} \quad (4.19a)$$

$$\tilde{\epsilon}_{st} = \begin{cases} f(1, r, s, rs, r^2s^2) & \text{for the MITC8 element,} \\ f(1, r, s, rs, r^2) & \text{for the MITC8}^N \text{ and MITC9 elements.} \end{cases} \quad (4.19b)$$

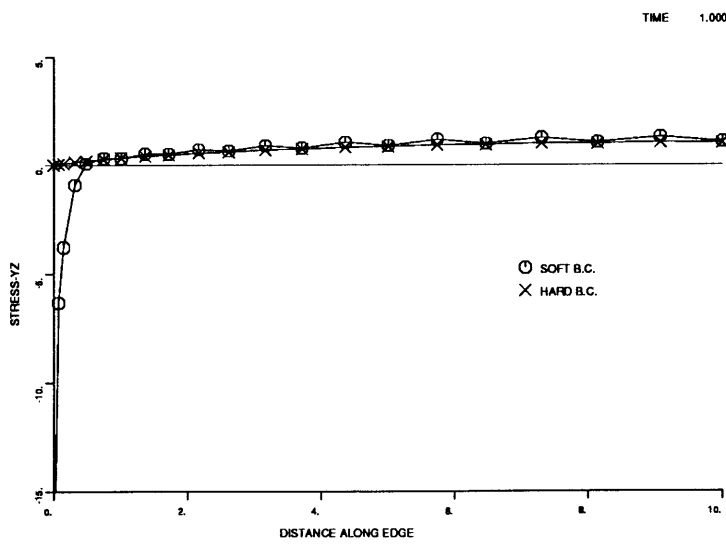
Each field in Eq. 4.19 consists of a bilinear field plus one additional field. In the case of the MITC8 element, the order of the fifth field,  $r^2s^2$ , is unreasonably high. This suggests that the MITC8 element is directly employing the  $r^2s^2$  field, skipping  $s^2$  and  $rs^2$  terms in the interpolation of  $\tilde{\epsilon}_{rt}$  component. The use of such incomplete field is responsible for the stress oscillation of the MITC8 element in the previous two examples.

### 4.3 Discussion of Different Interpolation Fields for the Nine-Node Elements

Now consider a curved cantilever under a tip moment as shown in Fig. 4-6. Table 4-1 summarizes the results obtained using the MITC8 element for the various meshes. The results show excellent predictive capabilities for all types of meshes used, except for the mesh distorted horizontally, as shown in Table 4-1c. Notice that the results obtained using the mesh distorted vertically (Table 4-1e) do not show any locking, even for extremely thin situations.

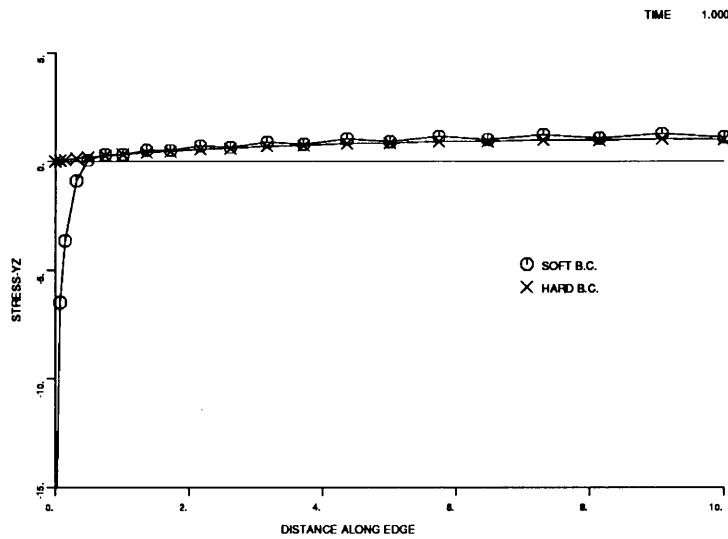


(a) MITC8 element



(b) MITC8<sup>N</sup> element

Figure 4-5: Shear stress oscillation in a square plate.



(c) MITC9 element

Figure 4-5 Continued.

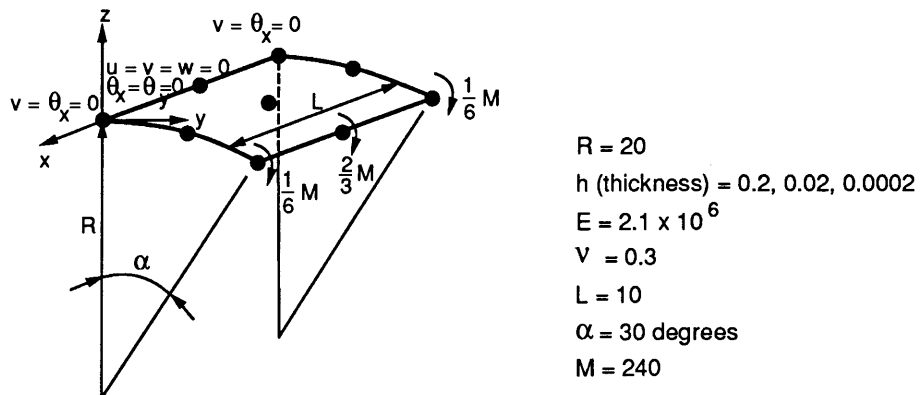
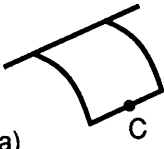
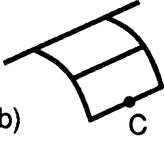
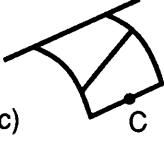
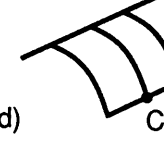
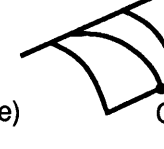


Figure 4-6: Physical model of the curved cantilever considered.

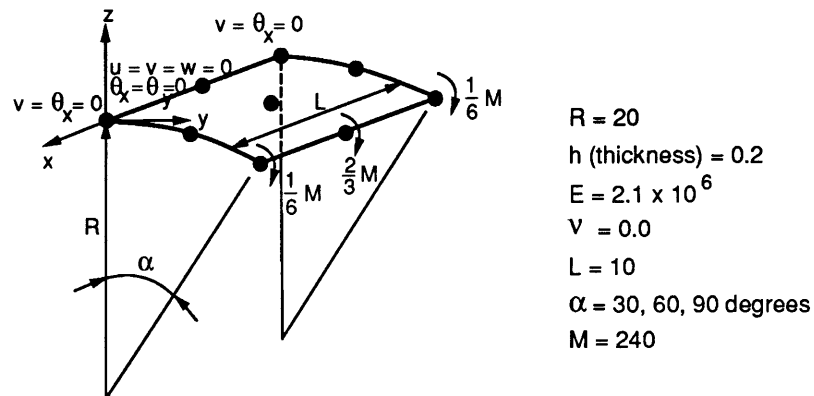
Table 4-1: 30 degrees curved cantilever under a tip moment for various mesh distortions.

Mesh used	$h/R$	$v = 0.0$	$v = 0.3$
(a) 	1 / 100	0.9998	1.0656
	1 / 1000	0.9996	1.0608
	1 / 10 <sup>5</sup>	0.9996	1.0608
(b) 	1 / 100	1.0008	1.0529
	1 / 1000	1.0000	1.0376
	1 / 10 <sup>5</sup>	1.0000	1.0373
(c) 	1 / 100	0.8958	0.9482
	1 / 1000	0.7230	0.7538
	1 / 10 <sup>5</sup>	0.0626	0.0649
(d) 	1 / 100	0.9995	1.0315
	1 / 1000	0.9996	0.9962
	1 / 10 <sup>5</sup>	0.9996	0.9947
(e) 	1 / 100	0.9999	1.0297
	1 / 1000	0.9999	1.0027
	1 / 10 <sup>5</sup>	0.9999	1.0016

A similar deterioration, as in the case of the horizontally distorted element, is observed when the side nodes are shifted in the opposite direction within a single element. Figure 4-7a shows the results of the analysis obtained using the undistorted element. Notice that the 90 degree curved cantilever beam can be analyzed using just a single shell element and yet maintain an error to within 3 percent of the tip rotation.

Figures 4-7b and 4-7c show the results of the analyses obtained using the elements with shifted nodes. In Fig. 4-7b, two side nodes are shifted in the same direction while the location of the other nodes are fixed. The elements are quite insensitive to node shifting of this kind.

The single element with two side nodes shifted in the opposite direction (see Fig. 4-7c) shows similar behavior as in the case of the horizontally distorted element (Table 4-1c). The behavior of the distorted elements is related to the orientation of the base vectors at the sampling points. Figure 4-8a shows the configuration of base vectors at the sampling points for the vertically distorted element. As can be seen in the side view of Fig. 4-8a, the distribution of sampling points for in-plane strain interpolation along the  $y$ -direction is equivalent to the 3-node curved beam element. It is known that the three node curved beam element does not membrane lock if the mixed-interpolation is used. Hence, if the membrane interpolation used at sampling points 6 and 8 (see 4-8a) is equivalent to the one used in the mixed-interpolated isobeam element, then a locking-free element for membrane strain is obtained. Since  $\bar{\mathbf{g}}_r$  and  $\bar{\mathbf{g}}_s$  run parallel to the  $x$ -axis and  $y$ -axis respectively, the strain component  $\varepsilon_{yy}$  is correctly interpolated as in the case of the 3-node isobeam element with mixed-interpolation. Notice that the  $\tilde{\varepsilon}_{ss}$  component of strains at the sampling point 6 is calculated using the projection of strains at sampling points 2 and 3. Component  $\tilde{\varepsilon}_{ss}$  at sampling point 8 is calculated similarly using the strains at sampling points 1 and 4. In other words, the strain components  $\tilde{\varepsilon}_{ss}$  at points 6 and 8 are not obtained by direct interpolation, but are interpolated using the strains at the neighboring sampling points. Notice also that the  $\tilde{\varepsilon}_{rr}$  components at points 6 and 8 are calculated by direct interpolation; however,  $\tilde{\varepsilon}_{rr}$  components do not contribute to the

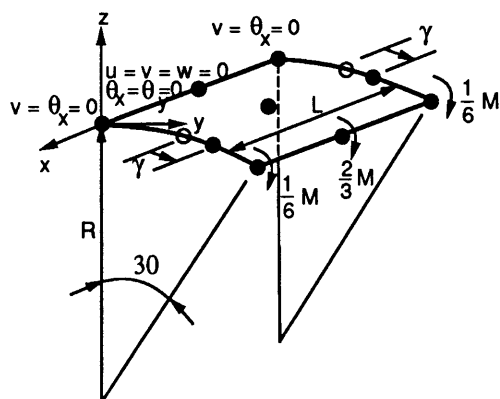


$\alpha$ (degrees)	MITC8	MITC9
30	0.999	0.999
60	0.994	0.993
90	0.974	0.972

(a) Analysis using undistorted element.

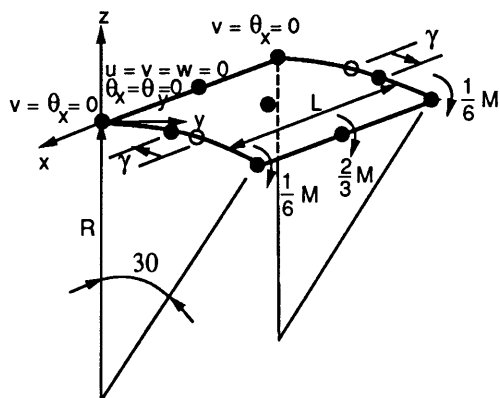
Figure 4-7: Analysis of a curved cantilever beam.





$\gamma$ (degrees)	MITC8	MITC9
0	0.999	0.999
3	1.001	1.002
5	1.003	1.005

(b) Analysis with node shifting in the same direction.



$\gamma$ (degrees)	MITC8	MITC9
0	0.999	0.999
3	0.971	0.980
5	0.895	0.893

(c) Analysis with node shifting in the opposite direction.

Figure 4-7 Continued.

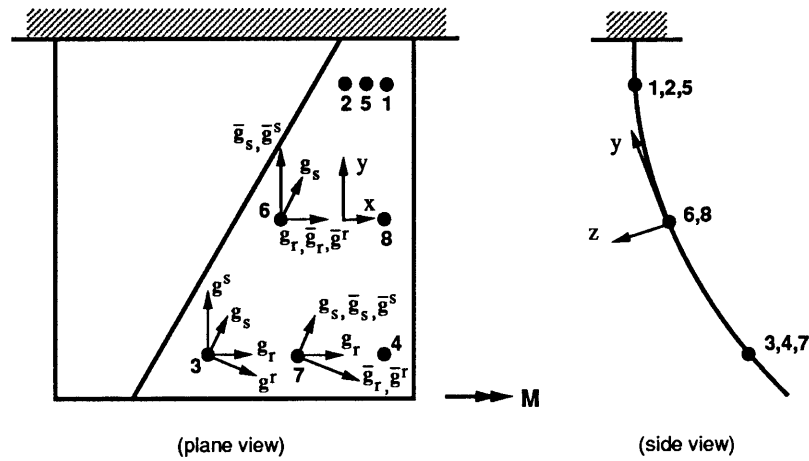
calculation of  $\varepsilon_{yy}$  since  $\bar{\mathbf{g}}_r$  is perpendicular to the  $y$ -axis as mentioned earlier.

Figure 4-8b shows the configuration of base vectors at the sampling points for the horizontally distorted element. Notice that the base vector orientation of the element in Fig. 4-7c is similar to the horizontally distorted element. In the case of a horizontally distorted element, the strain  $\varepsilon_{yy}$  cannot be interpolated properly for two reasons. First, as can be seen in the side view of Fig. 4-8a, more than enough sampling points are used along the  $y$ -direction. Only two sampling points must be used along the  $y$ -direction to avoid membrane locking, but the geometry of the mesh does not allow the reduced number of points in the sampling of strains. The second disadvantage of this geometry is that the base vector  $\bar{\mathbf{g}}_r$  is not orthogonal to the  $y$ -axis at sampling points 6 and 8. Hence, in the calculation of  $\varepsilon_{yy}$ , there is a contribution from the  $\tilde{\varepsilon}_{rr}$  component of strains at sampling points 6 and 8, which are directly interpolated (i.e. no projection is performed using neighboring elements). In other words, the structure becomes overconstrained in this situation.

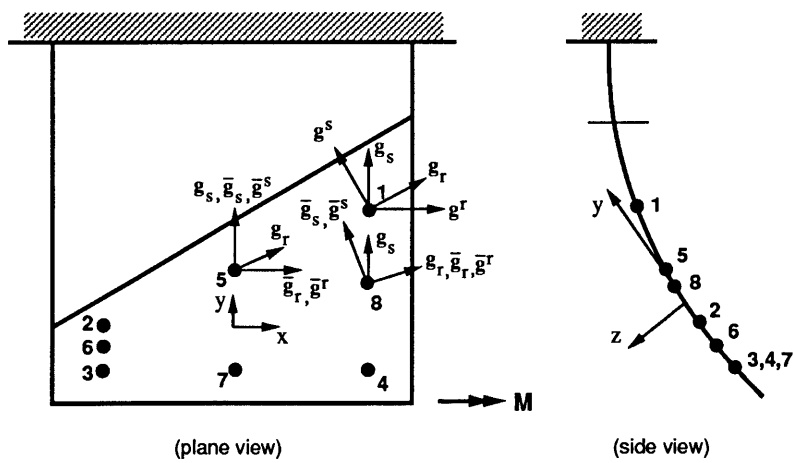
To improve the predictive capabilities of the element, the space of the displacement interpolation should be increased but without introducing spurious zero energy modes or nonconvergent behavior.

In the case of the MITC8 element, the space of the interpolation cannot be increased unless additional nodes are introduced. However, in the case of the 9-node element the space of the displacement interpolation can be increased by employing additional degrees of freedom at the center node. Table 4-2 shows the comparison between the MITC8, MITC9 and a few trial elements. The MITC9 element uses  $\theta_x$  and  $\theta_y$  (rotations only) at the center node. The TRIAL-1 element is obtained by using  $\theta_x$ ,  $\theta_y$ ,  $u_x$  and  $u_y$  at the center node, whereas the TRIAL-2 element is obtained by using  $\theta_x$ ,  $\theta_y$ ,  $u_x$ ,  $u_y$  and  $u_z$  at the center node.

Both the MITC9 and TRIAL-1 elements reduce to the MITC9 plate element given in Chap. 2 when the element is in the flat plate condition. The TRIAL-2 element violates the mathematical requirement even in the flat plate condition, but is included in Table 4-



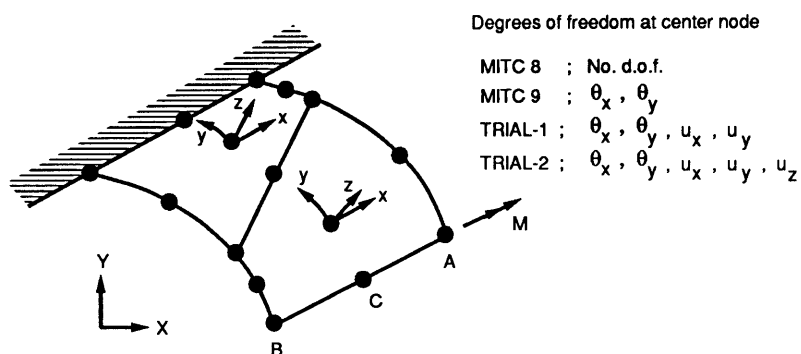
(a) Vertical distortion



(b) Horizontal distortion

Figure 4-8: Base vector variation in a curved cantilever beam.

Table 4-2: Response of a horizontally distorted curved cantilever.



Thickness	Location	MITC8	MITC9	TRIAL-1	TRIAL-2
$1/10^2$	A	1.067	1.012	1.020	1.037
	B	1.037	0.957	1.000	1.029
	C	0.948	0.996	1.067	1.083
$1/10^3$	A	0.783	0.846	0.979	0.963
	B	0.894	0.661	0.956	0.953
	C	0.754	0.668	1.036	1.073
$1/10^5$	A	0.125	0.400	0.902	0.968
	B	0.007	0.671	0.943	0.892
	C	0.065	0.287	0.951	1.065

2 for comparison. As the number of degrees of freedom employed at the center node increases, the locking is reduced. Comparing the MITC8 and MITC9 elements, the MITC9 element still has the tendency to lock in the case of very thin thickness, but the overall results are better compared to the MITC8 element. The TRIAL-1 element gives very accurate results (almost insensitive to the distortion and the element thickness). However, subsequent numerical experiment shows that the TRIAL-1 element is too soft in most situations, and hence is rejected from further consideration. As for the TRIAL-2 element, it can not be used in practice because the element contains one spurious zero energy mode.

The space of the displacement interpolation can be increased as long as the element does not contain any spurious zero energy mode. As the space of the displacement interpolation is increased in the element, the element exhibits softer behavior even in the case when there are no spurious zero energy modes (the TRIAL-1 element).

## 4.4 Implementation

Due to the complexity of the assumed strain interpolation, a proper computational scheme is necessary for the element to be effective. In this section, implementation of the MITC8<sup>N</sup> and MITC9 elements is discussed. First, consider the in-layer strain interpolation. Using Eqs. 3.41 through 3.46 in Eq. 3.40, the assumed strain field can be expressed as follows,

$$\begin{aligned}
\bar{\underline{\varepsilon}} = & \sum_{i=1}^4 h_i^{IS} \left[ \tilde{\varepsilon}_{rr} \mathbf{g}^r \mathbf{g}^r |_i^{DI} + \tilde{\varepsilon}_{ss} \mathbf{g}^s \mathbf{g}^s |_i^{DI} + \tilde{\varepsilon}_{rs} (\mathbf{g}^r \mathbf{g}^s + \mathbf{g}^s \mathbf{g}^r) |_i^{DI} \right] \\
& + h_5^{IS} \tilde{\varepsilon}_{ss} \bar{\mathbf{g}}^s \bar{\mathbf{g}}^s |_5^{DI} + h_5^{IS} \left[ \bar{\mathbf{g}}_r \cdot \{ \underline{\varepsilon}|_1^{DI} + \underline{\varepsilon}|_2^{DI} \} \cdot \bar{\mathbf{g}}_r \right] \bar{\mathbf{g}}^r \bar{\mathbf{g}}^r |_5^{DI} \\
& + h_5^{IS} \left[ \bar{\mathbf{g}}_r \cdot \{ \underline{\varepsilon}|_1^{DI} + \underline{\varepsilon}|_2^{DI} \} \cdot \bar{\mathbf{g}}_s \right] (\bar{\mathbf{g}}^r \bar{\mathbf{g}}^s + \bar{\mathbf{g}}^s \bar{\mathbf{g}}^r) |_5^{DI} \\
& + h_7^{IS} \tilde{\varepsilon}_{ss} \bar{\mathbf{g}}^s \bar{\mathbf{g}}^s |_7^{DI} + h_7^{IS} \left[ \bar{\mathbf{g}}_r \cdot \{ \underline{\varepsilon}|_3^{DI} + \underline{\varepsilon}|_4^{DI} \} \cdot \bar{\mathbf{g}}_r \right] \bar{\mathbf{g}}^r \bar{\mathbf{g}}^r |_7^{DI} \\
& + h_7^{IS} \left[ \bar{\mathbf{g}}_r \cdot \{ \underline{\varepsilon}|_3^{DI} + \underline{\varepsilon}|_4^{DI} \} \cdot \bar{\mathbf{g}}_s \right] (\bar{\mathbf{g}}^r \bar{\mathbf{g}}^s + \bar{\mathbf{g}}^s \bar{\mathbf{g}}^r) |_7^{DI}
\end{aligned}$$

$$\begin{aligned}
& + h_6^{IS} \tilde{\varepsilon}_{rr} \bar{\mathbf{g}}^r \bar{\mathbf{g}}^r |_6^{DI} + h_6^{IS} \left[ \bar{\mathbf{g}}_s \cdot \{ \underline{\varepsilon}|_2^{DI} + \underline{\varepsilon}|_3^{DI} \} \cdot \bar{\mathbf{g}}_s \right] \bar{\mathbf{g}}^s \bar{\mathbf{g}}^s |_6^{DI} \\
& \quad + h_6^{IS} \left[ \bar{\mathbf{g}}_r \cdot \{ \underline{\varepsilon}|_2^{DI} + \underline{\varepsilon}|_3^{DI} \} \cdot \bar{\mathbf{g}}_s \right] (\bar{\mathbf{g}}^r \bar{\mathbf{g}}^s + \bar{\mathbf{g}}^s \bar{\mathbf{g}}^r) |_6^{DI} \\
& + h_8^{IS} \tilde{\varepsilon}_{rr} \bar{\mathbf{g}}^r \bar{\mathbf{g}}^r |_8^{DI} + h_8^{IS} \left[ \bar{\mathbf{g}}_s \cdot \{ \underline{\varepsilon}|_1^{DI} + \underline{\varepsilon}|_4^{DI} \} \cdot \bar{\mathbf{g}}_s \right] \bar{\mathbf{g}}^s \bar{\mathbf{g}}^s |_8^{DI} \\
& \quad + h_8^{IS} \left[ \bar{\mathbf{g}}_r \cdot \{ \underline{\varepsilon}|_1^{DI} + \underline{\varepsilon}|_4^{DI} \} \cdot \bar{\mathbf{g}}_s \right] (\bar{\mathbf{g}}^r \bar{\mathbf{g}}^s + \bar{\mathbf{g}}^s \bar{\mathbf{g}}^r) |_8^{DI}. \quad (4.20)
\end{aligned}$$

Next the following tensor transformation is used to obtain the global Cartesian components of the strain,

$$\tilde{\varepsilon}_{ij} \mathbf{g}^i \mathbf{g}^j = \varepsilon_{kl} \hat{\mathbf{e}}_k \hat{\mathbf{e}}_l \quad (4.21)$$

or

$$\varepsilon_{kl} = (\tilde{\varepsilon}_{ij})(\hat{\mathbf{e}}_k \cdot \mathbf{g}^i)(\mathbf{g}^j \cdot \hat{\mathbf{e}}_l) \quad (4.22)$$

where  $\varepsilon_{kl}$  is the component of the strain tensor measured in the global Cartesian coordinate system.

The resulting components of strain tensor in the global Cartesian coordinate system are,

$$\begin{aligned}
\varepsilon_{kl} = \tilde{\varepsilon}_{rr} |_1 & \left[ h_1^{IS} \hat{\mathbf{e}}_k \cdot (\mathbf{g}^r \mathbf{g}^r) |_1 \cdot \hat{\mathbf{e}}_l \right. \\
& + h_8^{IS} R_{18s} \hat{\mathbf{e}}_k \cdot (\mathbf{g}^s \mathbf{g}^s) |_8 \cdot \hat{\mathbf{e}}_l + h_8^{IS} R_{18t} \hat{\mathbf{e}}_k \cdot (\mathbf{g}^r \mathbf{g}^s + \mathbf{g}^s \mathbf{g}^r) |_8 \cdot \hat{\mathbf{e}}_l \\
& + h_5^{IS} R_{15s} \hat{\mathbf{e}}_k \cdot (\mathbf{g}^s \mathbf{g}^s) |_5 \cdot \hat{\mathbf{e}}_l + h_5^{IS} R_{15t} \hat{\mathbf{e}}_k \cdot (\mathbf{g}^r \mathbf{g}^s + \mathbf{g}^s \mathbf{g}^r) |_5 \cdot \hat{\mathbf{e}}_l \left. \right] \\
+ \tilde{\varepsilon}_{ss} |_1 & \left[ h_1^{IS} \hat{\mathbf{e}}_k \cdot (\mathbf{g}^s \mathbf{g}^s) |_1 \cdot \hat{\mathbf{e}}_l \right. \\
& + h_8^{IS} S_{18s} \hat{\mathbf{e}}_k \cdot (\mathbf{g}^s \mathbf{g}^s) |_8 \cdot \hat{\mathbf{e}}_l + h_8^{IS} S_{18t} \hat{\mathbf{e}}_k \cdot (\mathbf{g}^r \mathbf{g}^s + \mathbf{g}^s \mathbf{g}^r) |_8 \cdot \hat{\mathbf{e}}_l \\
& + h_5^{IS} S_{15r} \hat{\mathbf{e}}_k \cdot (\mathbf{g}^r \mathbf{g}^r) |_5 \cdot \hat{\mathbf{e}}_l + h_5^{IS} S_{15t} \hat{\mathbf{e}}_k \cdot (\mathbf{g}^r \mathbf{g}^s + \mathbf{g}^s \mathbf{g}^r) |_5 \cdot \hat{\mathbf{e}}_l \left. \right] \\
+ \tilde{\varepsilon}_{rs} |_1 & \left[ h_1^{IS} \hat{\mathbf{e}}_k \cdot (\mathbf{g}^r \mathbf{g}^s + \mathbf{g}^s \mathbf{g}^r) |_1 \cdot \hat{\mathbf{e}}_l \right. \\
& + h_8^{IS} T_{18s} \hat{\mathbf{e}}_k \cdot (\mathbf{g}^s \mathbf{g}^s) |_8 \cdot \hat{\mathbf{e}}_l + h_8^{IS} T_{18t} \hat{\mathbf{e}}_k \cdot (\mathbf{g}^r \mathbf{g}^s + \mathbf{g}^s \mathbf{g}^r) |_8 \cdot \hat{\mathbf{e}}_l \\
& + h_5^{IS} T_{15r} \hat{\mathbf{e}}_k \cdot (\mathbf{g}^r \mathbf{g}^r) |_5 \cdot \hat{\mathbf{e}}_l + h_5^{IS} T_{15t} \hat{\mathbf{e}}_k \cdot (\mathbf{g}^r \mathbf{g}^s + \mathbf{g}^s \mathbf{g}^r) |_5 \cdot \hat{\mathbf{e}}_l \left. \right] \\
& + \text{similar expressions for sampling points 2, 3 and 4}
\end{aligned}$$

$$\begin{aligned}
& + \tilde{\epsilon}_{ss}|_5 \quad [ \quad h_5^{IS} \hat{e}_k \cdot (\mathbf{g}^s \mathbf{g}^s)|_5 \cdot \hat{e}_l ] \\
& + \tilde{\epsilon}_{rr}|_6 \quad [ \quad h_6^{IS} \hat{e}_k \cdot (\mathbf{g}^r \mathbf{g}^r)|_6 \cdot \hat{e}_l ] \\
& + \tilde{\epsilon}_{ss}|_7 \quad [ \quad h_7^{IS} \hat{e}_k \cdot (\mathbf{g}^s \mathbf{g}^s)|_7 \cdot \hat{e}_l ] \\
& + \tilde{\epsilon}_{rr}|_8 \quad [ \quad h_8^{IS} \hat{e}_k \cdot (\mathbf{g}^r \mathbf{g}^r)|_8 \cdot \hat{e}_l ]
\end{aligned} \tag{4.23}$$

where  $R$ ,  $S$  and  $T$  are constants derived from the product of base vectors:

$$R_{mni} = \frac{1}{2} \mathbf{g}_i|_n \cdot (\mathbf{g}^r \mathbf{g}^r)|_m \cdot \mathbf{g}_i|_n \tag{4.24a}$$

$$S_{mni} = \frac{1}{2} \mathbf{g}_i|_n \cdot (\mathbf{g}^s \mathbf{g}^s)|_m \cdot \mathbf{g}_i|_n \tag{4.24b}$$

$$T_{mni} = \frac{1}{2} \mathbf{g}_i|_n \cdot (\mathbf{g}^r \mathbf{g}^s + \mathbf{g}^s \mathbf{g}^r)|_m \cdot \mathbf{g}_i|_n. \tag{4.24c}$$

Equation 4.23 represents the contribution from the in-layer part of the strains to the global Cartesian strain components.

The contribution from the shear strain can be constructed in a similar way. Using Eqs. 3.48 and 3.50 in Eq. 4.22, the components of the strain tensor measured in the global Cartesian coordinate system are,

$$\begin{aligned}
\epsilon_{kl} & = \sum_{i=1}^4 \tilde{\epsilon}_{rt}|_i h_i^{RT} \hat{e}_k \cdot (\mathbf{g}^r \mathbf{g}^t + \mathbf{g}^t \mathbf{g}^r)|_i \cdot \hat{e}_l \\
& + \frac{1}{2} \tilde{\epsilon}_{rt}|_{RA} h_5^{RT} \hat{e}_k \cdot (\mathbf{g}^r \mathbf{g}^t + \mathbf{g}^t \mathbf{g}^r)|_5 \cdot \hat{e}_l \\
& + \frac{1}{2} \tilde{\epsilon}_{rt}|_{RB} h_5^{RT} \hat{e}_k \cdot (\mathbf{g}^r \mathbf{g}^t + \mathbf{g}^t \mathbf{g}^r)|_5 \cdot \hat{e}_l \\
& + \sum_{i=1}^4 \tilde{\epsilon}_{st}|_i h_i^{ST} \hat{e}_k \cdot (\mathbf{g}^s \mathbf{g}^t + \mathbf{g}^t \mathbf{g}^s)|_i \cdot \hat{e}_l \\
& + \frac{1}{2} \tilde{\epsilon}_{st}|_{SA} h_5^{ST} \hat{e}_k \cdot (\mathbf{g}^s \mathbf{g}^t + \mathbf{g}^t \mathbf{g}^s)|_5 \cdot \hat{e}_l \\
& + \frac{1}{2} \tilde{\epsilon}_{st}|_{SB} h_5^{ST} \hat{e}_k \cdot (\mathbf{g}^s \mathbf{g}^t + \mathbf{g}^t \mathbf{g}^s)|_5 \cdot \hat{e}_l.
\end{aligned} \tag{4.25}$$

Notice that Eqs. 4.23 and 4.25 are the expressions for the general total strains. Hence,

they can be used for the calculation of both linear and nonlinear incremental strains.

For linear incremental strains, Eq. 3.31 can be used to calculate the strains at the sampling points (*i.e.*  ${}_0\tilde{\epsilon}_{ij}|_{sp}$ ) in Eqs. 4.23 and 4.25. Then, defining a vector

$${}_0\mathbf{e}^T = [{}_0e_{xx} \quad {}_0e_{yy} \quad {}_0e_{zz} \quad 2{}_0e_{xy} \quad 2{}_0e_{xz} \quad 2{}_0e_{yz}], \quad (4.26)$$

the usual relation [Bathe, 1982]

$${}_0\mathbf{e}^T = {}^t_0\mathbf{B}_L \mathbf{U} \quad (4.27)$$

is obtained. Expression of strains in a form given in Eq. 4.27 is possible because all the strain terms in Eq. 3.31 are expressed in terms of nodal point variables.

From the linearized equation of motion,

$${}^t_0\mathbf{K}_L = \int_{{}_0V} {}^t_0\mathbf{B}_L^T {}_0\mathbf{C} {}^t_0\mathbf{B}_L {}^0dV \quad (4.28)$$

is obtained where  ${}_0\mathbf{C}$  is a constitutive matrix formed with the contravariant components  ${}_0C^{ijkl}$  of the constitutive tensor. The contravariant components  ${}_0C^{ijkl}$  of the constitutive tensor relates the increments of the contravariant components  ${}_0S^{ij}$  of the 2nd Piola-Kirchhoff stress tensor with the increments of the covariant components  ${}_0\epsilon_{ij}$  of the Green-Lagrange strain tensor. Both  ${}_0S^{ij}$  and  ${}_0\epsilon_{ij}$  components are measured in the global Cartesian system. The incremental constitutive equation in matrix notation is,

$${}_0\mathbf{S} = {}_0\mathbf{C} {}_0\boldsymbol{\epsilon} \quad (4.29)$$

where

$${}_0\mathbf{S}^T = [{}_0S^{xx} \quad {}_0S^{yy} \quad {}_0S^{zz} \quad {}_0S^{xy} \quad {}_0S^{xz} \quad {}_0S^{yz}] \quad (4.30)$$

and

$${}_0\boldsymbol{\epsilon}^T = [{}_0\epsilon_{xx} \quad {}_0\epsilon_{yy} \quad {}_0\epsilon_{zz} \quad 2{}_0\epsilon_{xy} \quad 2{}_0\epsilon_{xz} \quad 2{}_0\epsilon_{yz}]. \quad (4.31)$$

The global Cartesian components  ${}_0C^{ijkl}$  are calculated from the components in  $\bar{r}$ ,  $\bar{s}$ ,



$t$  Cartesian shell-aligned coordinate system  $(\bar{\mathbf{e}}_{\bar{r}}, \bar{\mathbf{e}}_{\bar{s}}, \bar{\mathbf{e}}_{\bar{t}})$ .

$${}_0C^{ijkl} = {}_0\bar{C}_{mnpq}(\hat{\mathbf{e}}_i \cdot \bar{\mathbf{e}}_{\bar{m}})(\hat{\mathbf{e}}_j \cdot \bar{\mathbf{e}}_{\bar{n}})(\hat{\mathbf{e}}_k \cdot \bar{\mathbf{e}}_{\bar{p}})(\hat{\mathbf{e}}_l \cdot \bar{\mathbf{e}}_{\bar{q}}). \quad (4.32)$$

The fourth-order tensor transformation in Eq. 4.32 can be effectively evaluated using the matrix notation,

$${}_0\mathbf{C} = \mathbf{Q}_{sh}^T {}_0\bar{\mathbf{C}} \mathbf{Q}_{sh} \quad (4.33)$$

where

$${}_0\bar{\mathbf{C}} = \frac{E}{1-\nu^2} \begin{bmatrix} 1 & \nu & 0 & 0 & 0 & 0 \\ \nu & 1 & 0 & 0 & 0 & 0 \\ & & 0 & 0 & 0 & 0 \\ \text{symmetric} & & \frac{1-\nu}{2} & 0 & 0 & \\ & & & k\frac{1-\nu}{2} & 0 & \\ & & & & k\frac{1-\nu}{2} & \end{bmatrix} \quad (4.34)$$

and  $\mathbf{Q}_{sh}$  represents a matrix that transforms the stress-strain law from an  $\bar{\mathbf{e}}_{\bar{r}}, \bar{\mathbf{e}}_{\bar{s}}, \bar{\mathbf{e}}_{\bar{t}}$  Cartesian shell-aligned coordinate system to the global Cartesian coordinate system. The elements of the matrix  $\mathbf{Q}_{sh}$  are obtained from the direction cosines of the  $\bar{\mathbf{e}}_{\bar{r}}, \bar{\mathbf{e}}_{\bar{s}}, \bar{\mathbf{e}}_{\bar{t}}$  coordinate axes measured in the  $x, y, z$  coordinate directions.

The non-linear part of the tangent stiffness matrix can be derived from the equality

$$\delta \mathbf{U}^T {}_0^t \mathbf{K}_{NL} \mathbf{U} = \int_{0V} {}_0^t S^{ij} \delta {}_0 \eta_{ij} {}_0 dV \quad (4.35)$$

In the formulation, the strain-displacement matrix corresponding to the global Cartesian strain components, which were obtained from the assumed strain components by tensor transformation, was calculated. Alternatively, one could calculate the strain components corresponding to coordinate axes aligned with the midsurface of the shell element and establish a strain-displacement matrix for strain components. In the displacement-based shell element, the relative computational efficiency of these two approaches depends on whether it is more effective to transform the strain components (which always differ

at the integration points) or to transform the stress-strain law.

This comparison does not apply in the current formulation. In the assumed strain formulation, the components of the strains are interpolated together with the base vectors referred to them at the sampling points. Therefore, the base vector at a particular integration point and its component cannot be separated. As shown in Eq. 4.20, the strain is always expressed in terms of the components and the base vectors interpolated together at the sampling points. To extract the component at a particular point of interest (usually at an integration point), a second order tensor transformation is required. This transformation is necessary regardless of the coordinate system used at that point, and can be performed by using Eq. 4.23 after replacing  $\hat{\mathbf{e}}_k$  and  $\hat{\mathbf{e}}_l$  with the base vectors from the coordinate frame employed at the point of interest. In the present case where the global Cartesian coordinate frame is used for stress and strain reference, both the strain components and the stress-strain law need to be transformed. Therefore it is tempting to use  $\bar{r}, \bar{s}, t$  shell-aligned Cartesian coordinate system ( $\bar{\mathbf{e}}_{\bar{r}}, \bar{\mathbf{e}}_{\bar{s}}, \bar{\mathbf{e}}_t$ ) in order to avoid the transformation of the stress-strain law given in Eq. 4.33. However, the use of the global Cartesian coordinate frame in the present formulation is more efficient because of the following two reasons.

First, consider the transformation of strains in Eqs. 4.23 and 4.25. In the case of using the global Cartesian coordinate system, the base vector product involved has the following form

$$\varepsilon_{kl} = f(\hat{\mathbf{e}}_k \cdot (\mathbf{g}^i \mathbf{g}^j)|_{sp} \cdot \hat{\mathbf{e}}_l, \dots) \quad (4.36)$$

where  $(\mathbf{g}^i \mathbf{g}^j)|_{sp}$  are the contravariant base vectors at the sampling points.

In the case of the shell aligned  $\bar{r}, \bar{s}, t$  Cartesian coordinate system, the base vector products involved are

$$\bar{\varepsilon}_{kl} = f(\bar{\mathbf{g}}_k \cdot (\mathbf{g}^i \mathbf{g}^j)|_{sp} \cdot \bar{\mathbf{g}}_l, \dots). \quad (4.37)$$

Since all base vectors are expressed in terms of the global Cartesian coordinate, the base vector product in Eq. 4.36 does not require any multiplication operation. Only the

$k$ -component from the  $\mathbf{g}^i$  vector is necessary to calculate  $\hat{\mathbf{e}}_k \cdot (\mathbf{g}^i)|_{sp}$ . However, in the case of using the  $\bar{r}, \bar{s}, t$  Cartesian coordinate system in Eq. 4.37, the base vector product requires explicit evaluation of the vector product  $\bar{\mathbf{g}}_k \cdot (\mathbf{g}^i)|_{sp}$ . Due to the large number of operations involved in the base vector product, this approach is less efficient in spite of the computational time savings in applying the stress-strain law.

Second, and more importantly, the advantage of using the global Cartesian coordinate system is that the product  $\hat{\mathbf{e}}_k \cdot (\mathbf{g}^i)|_{sp}$  is constant throughout the element for the fixed layer. In the  $\bar{r}, \bar{s}, t$  Cartesian coordinate system, the products  $\bar{\mathbf{g}}_k \cdot (\mathbf{g}^i)|_{sp}$  always differ at the integration points. The fact that the product  $\hat{\mathbf{e}}_k \cdot (\mathbf{g}^i)|_{sp}$  is constant contributes to the large reduction in computation time in evaluating Eqs. 4.23 and 4.25. In Eqs. 4.23 and 4.25 the only varying term at each integration point for the fixed layer is the value of interpolation function. Hence, the calculation of all the constant terms and the base vector product can be extracted from the numerical integration loop for the fixed layer. This extraction is not possible if the  $\bar{r}, \bar{s}, t$  Cartesian coordinate system is used since the base vector products are not constants.

Since the evaluation of Eqs. 4.23 and 4.25 involves large amount of computation, it is important to extract the operation, as much as possible, from the in-plane numerical integration loop. Careful implementation considering these characteristics reduces computation time in the stiffness matrix evaluation by a factor of two compared to the existing procedure in the the case of a linear analysis. In the case of a nonlinear analysis, full quadratic convergence is observed as expected, without additional computation time increase for executing nonlinear stiffness matrix reformation. Additional discussion is presented with an example in Chapter 5.

For the MITC8<sup>N</sup> and MITC9 shell elements, the following steps are carried out in the implementation.

**step 1:** At the midsurface,

- Calculate the base vectors at the sampling points for the transverse shear strain interpolation.

- Calculate the directly interpolated shear strains at each sampling point and put them in a storage.
- Calculate constant terms and base vector products in Eq. 4.25 and put them in a storage.

**step 2:** For each layer (integration through  $t$ -direction),

- Calculate base vectors at the sampling points for in-layer strain interpolation.
- Calculate the directly interpolated in-layer strains at each sampling point and put them in a storage.
- Calculate constant terms and base vector products in Eq. 4.23 and put them in a storage.
- For each integration point with a fixed layer (integration over  $r$ - $s$  plane, while  $t$  is fixed.),
  - Transform the stress-strain law to the global Cartesian coordinate system using Eq. 4.33.
  - Calculate the component of strains using Eqs. 4.23 and 4.25. Here, only the values of the interpolation function at the integration point need to be evaluated. Then, use the constant terms and directly interpolated strains in the storage for the actual evaluation of the strain components.
  - From the strain components calculated, construct the strain displacement matrix.
  - Use Eq. 4.28 to calculate the linear contribution to the stiffness matrix.
  - For a nonlinear analysis, accumulate the coefficients corresponding to each directly interpolated nonlinear strain in Eq. 4.23.
- For the nonlinear analysis use Eq. 4.35 to calculate nonlinear contribution to the stiffness matrix. Here, the previously accumulated coefficients are multiplied to the corresponding directly interpolated nonlinear strains.

# Chapter 5

## Numerical Tests and Problem Solutions

The new nine node shell element discussed in Chapters 3 and 4 has been implemented in the general purpose computer program ADINA [ADINA R&D, 1987]. In this chapter, various numerical tests are conducted to study the predictive capabilities of the element. The results demonstrate the excellent predictive capabilities of the new MITC9 shell element.

For some analyses, results obtained with the MITC4 [Bathe and Dvorkin, 1985] and MITC8 [Bathe and Dvorkin, 1986] elements are also presented for comparison. A comparison with other existing elements in the literature is also included. As in the case of the MITC plate analyses, the MITC9 shell element stiffness matrix is evaluated with “full” numerical integration ( $3 \times 3$  Gauss integration in case of the MITC9 element).

### 5.1 Stability of the Element

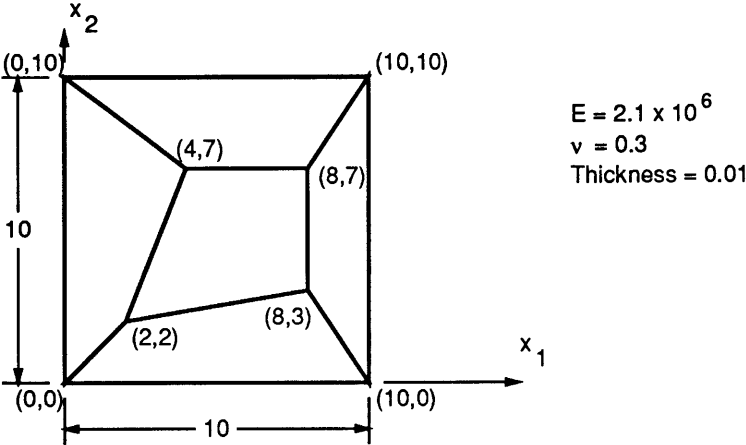
As a first step to check the stability of the MITC9 element, the eigenvalues of the stiffness matrices of undistorted and distorted elements were calculated. In all cases, the element displayed the six rigid body modes and no spurious zero energy modes.

Next, various patch tests were performed for the patch of elements shown in Fig. 5-1a. Since the pass of the patch tests is only a necessary condition for convergence, this simple patch test does not display the complete convergence characteristics of an element. However, the pass of the patch tests is an indication of the stability of the element for practical purposes and is regarded as a condition for a reliable element.

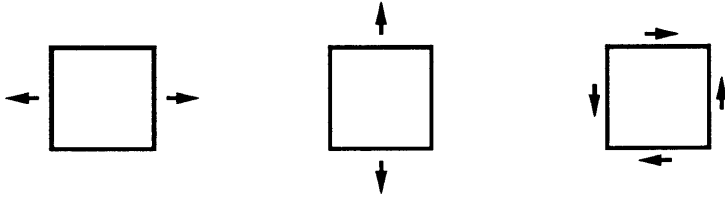
In the first analysis (Fig. 5-1b), distributed edge tension and shearing forces of constant intensity are applied for the membrane patch test. In this test, only the minimum number of degrees of freedom are deleted to eliminate the physical rigid body modes [Dvorkin and Bathe, 1984]. Linear displacements and constant membrane stresses (both tensile and in-plane shear) are obtained.

In the second analysis, the bending patch test shown in Fig. 5-1c was performed. In the test distributed edge couples of constant intensity were applied at the right hand edge of the patch of elements which is clamped at the left hand edge. Note that the vertical deflections at the two corner nodes on the clamped edge are left free to enable the shell to deform with constant curvature. A constant curvature (linear distribution of rotations) was obtained in the two directions.

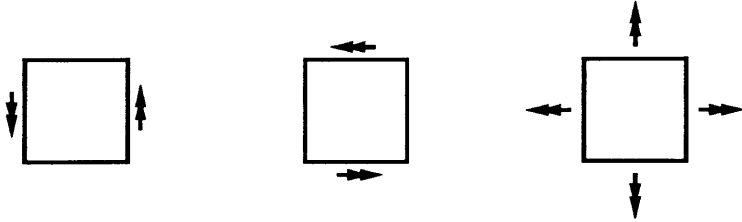
In the third analysis, the mesh was subjected to an external twisting moment as shown in Fig. 5-1d. In the test, the patch of elements is supported on three corners and loaded with a point load on the fourth corner. This test is reasonable for Mindlin plates which are very thin. In this test (thickness/length = 1/1000), a slight asymmetry in the displacement response (the sixth digit) was obtained due to the asymmetric representation of the transverse shear deformations. In the thin plate analysis (thickness/length = 1/10000), this asymmetry is not observed and constant curvatures were obtained in both plate directions and the transverse displacements agreed with the analytical thin plate solution.



(a) Patch of elements considered.



(b) Membrane tests



(c) Bending tests

(d) Twisting test

Figure 5-1: Patch of the elements used in a patch test.

## 5.2 Sample Analyses

### 5.2.1 Analysis of a Perforated Tension Strip

To illustrate the difference in stress prediction between the new 9-node shell element and the usual isoparametric 8-node plane stress element, the results obtained in the analysis of the plate shown in Fig. 5-2a are given. The analytical solution for the stress  $\tau_{zz}$  at locations  $C$  and  $D$  in Fig. 5-2a is given in [Timoshenko and Goodier, 1970]. Figure 5-2b shows the finite element mesh used in the analysis. For the stress calculations in both cases, the strains are obtained from the strain-displacement matrices evaluated directly at the points  $C$  and  $D$ . Hence, no stress extrapolation or stress smoothing is used. Figure 5-2c shows that the 8-node isoparametric element yields a slightly more accurate solution. Notice that the 8-node isoparametric element passes the membrane patch test even for curved element sides.

### 5.2.2 Analysis of a Cantilever under Distributed Load

In this example, a cantilever shown in Fig. 5-3 was analyzed to verify the shell element when subjected to distributed loading. The cantilever is discretized with five equally spaced shell elements. Using beam theory the theoretical solution for the end displacement is

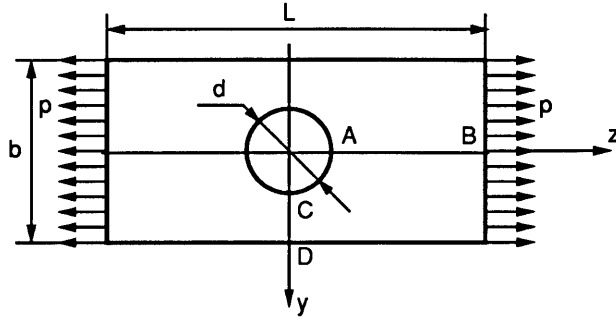
$$\delta = -\frac{11 PL^3}{60 EI} - \frac{5 PL}{6 A_S G} \quad (5.1)$$

Figure 5-3a shows normalized solution for the end displacement and the axial stress (in the direction of the beam) at the upper stress point closest to the fixed end. The results show a good agreement with the analytical solution.

### 5.2.3 Analysis of Morley Skew Plate

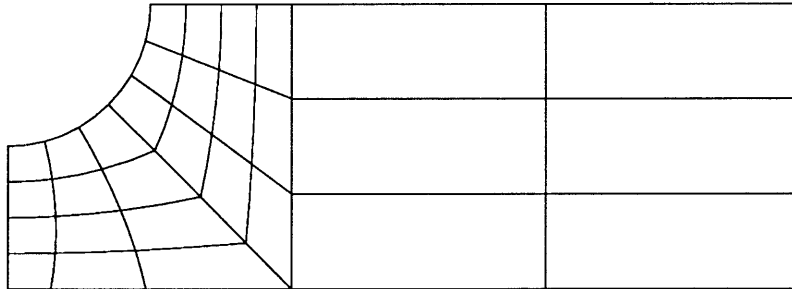
Figure 5-4 shows the thirty degree skew plate which is simply supported on all edges. This problem is often used to test the performance of the shell element because of the





$L = 56$                        $E = 7 \times 10^4$   
 $b = 20$                          $\nu = 0.25$   
 $d = 10$                          $p = 25$   
 $h$  (thickness) = 1

(a) Physical model considered.



(b) Finite element discretization.

Stress	Reference	2-D element	MITC8	MITC9
$\tau_{zz} _C$	107.5	109.7	112.4	112.4
$\tau_{zz} _D$	18.75	16.73	16.79	16.80

(c) Analysis results.

Figure 5-2: Analysis of a perforated tension strip.

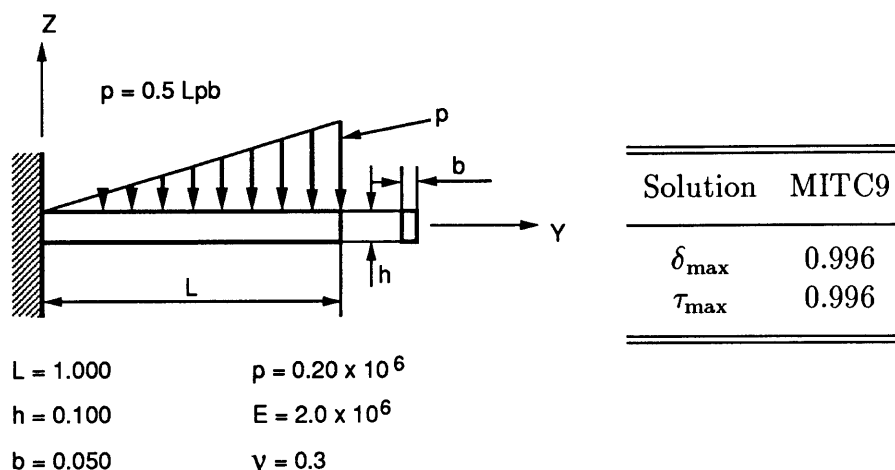


Figure 5-3: Analysis of a cantilever under a distributed load.

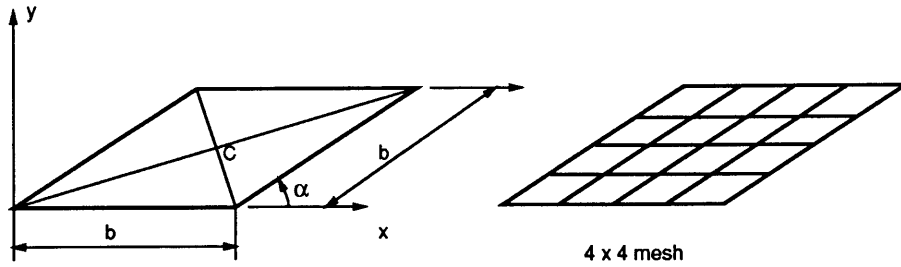
The cantilever is discretized with five equally spaced shell elements.

difficulty in the analysis due to the singularity in the bending moment at the obtuse corner.

The typical finite element discretization with the uniform skew mesh topology is also shown in Fig. 5-4a. The appropriate boundary condition to model the simple support with a Reissner/Mindlin plate theory-based element is that only the transverse displacement  $w$  is constrained to zero (soft condition). Figure 5-4b shows the good convergence behavior of the MITC9 element to the solution obtained by Morley [Morley, 1963]. The MITC8<sup>N</sup> element shows a slight improvement compared to the old MITC8 element. The result obtained by Huang and Hinton is also included for comparison [Huang and Hinton, 1984; Hinton and Huang, 1986]. Huang and Hinton tested various assumed strain elements in the literature, the best results obtained using QUAD9\* element are compared. Notice that the MITC9 element outperforms the QUAD9\* element.

#### 5.2.4 Analysis of Scordelis-Lo Cylindrical Roof

The Scordelis-Lo roof shown in Fig. 5-5a has attained the status of a de facto standard test problem. In this test, a cylindrical shell roof subjected to gravity loading is considered.



Simply supported edges

Boundary condition  $w = 0$   
on four edges

$E = 30. \times 10^6$

$\nu = 0.3$

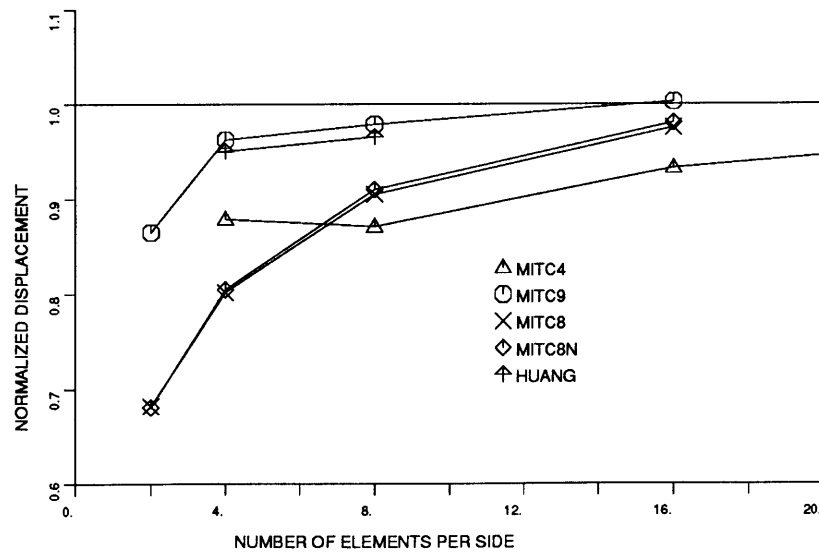
$b = 1$

$\alpha = 30$  degrees

Thickness = 0.01

Uniform pressure  $p = 1$

(a) Physical model considered.



(b) Analysis results.

Figure 5-4: Analysis of Morley skew plate.

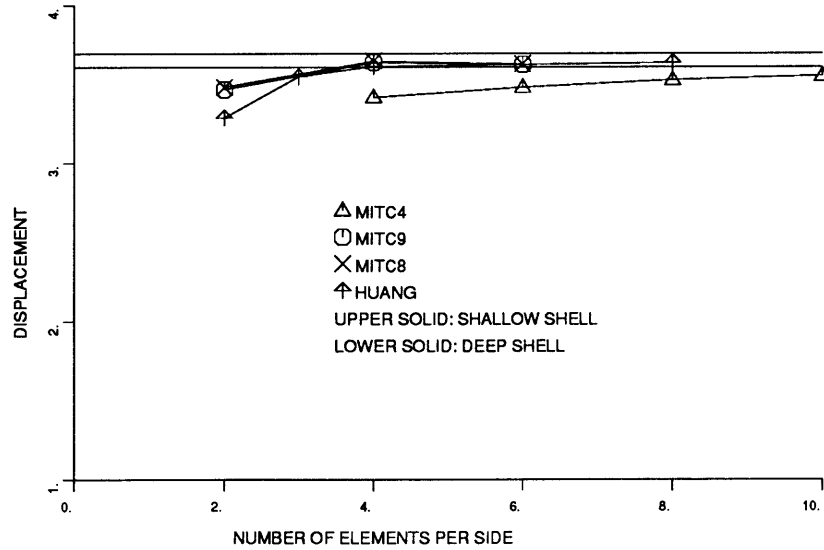
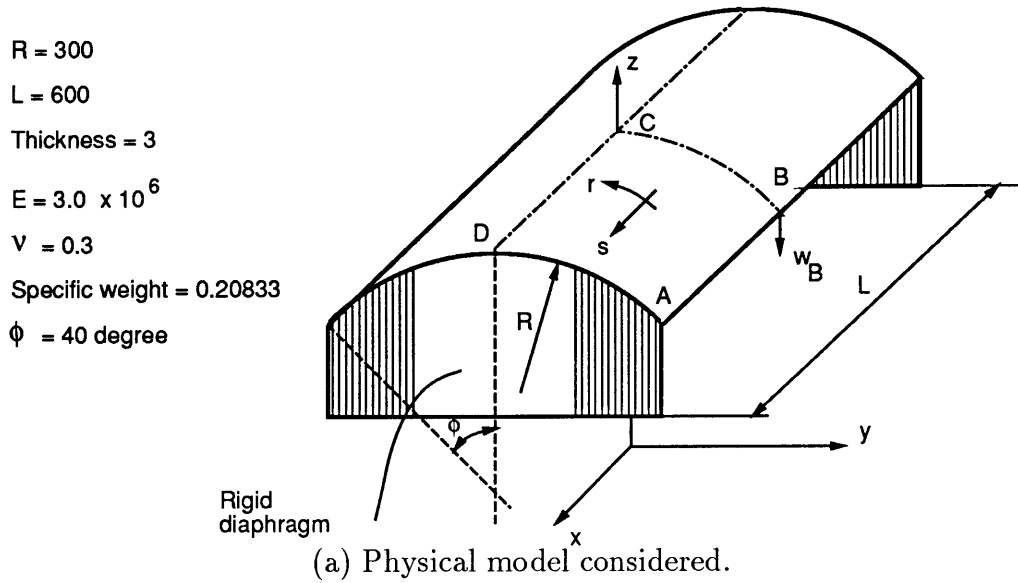
The shell roof is supported on diaphragms at the ends and it is free along the longitudinal sides. Both membrane and bending deformations contribute significantly to the response. The analytical shallow shell solution generally quoted for the vertical deflection at the center of the free edge (point B in Fig. 5-5a) is 3.703 [Scordelis and Lo, 1964], but many finite elements converge to a slightly smaller value and some authors use 3.696 as a reference solution. A deep shell exact analytical solution quoted is 3.610. Figure 5-5b shows that using the MITC9 element good convergence to the analytical solution is obtained. The result obtained by Huang and Hinton is also included for comparison [Huang and Hinton, 1986]. Huang's result shown in Fig. 5-5b is the one obtained using their best element QUAD9\*\* for this problem. Notice also that the MITC9 element converges fast and gives excellent results even with the coarse meshes.

Figures 5-5c and 5-5d are the pressure band plots obtained using the MITC4 and MITC9 elements respectively. Notice that the pressure band plot using the MITC9 element shows smoother distribution of the stresses. Figures 5-5e, 5-5f, and 5-5g are the in-plane stress plots along the line BC obtained using the MITC4, MITC8, and MITC9 elements respectively. The  $rr$ -component plots show the advantage of using higher order element in the stress prediction.

### 5.2.5 Analysis of a Pinched Cylindrical Shell

The cylindrical shell structure shown in Fig. 5-6a is analyzed to study its static response. The cylinder is freely supported at its ends and is loaded by two centrally located and diametrically opposed concentrated forces. Using the double symmetry of the structure and the loads, only one eighth of the cylinder is analyzed. The results were compared to the analytical solution reported in [Lindberg *et al.*, 1969]. It is interesting to note that the MITC9 element converges from upward in this problem. This is due to the fact that the MITC9 element employs more expanded field in the displacement interpolation, resulting in a softer solution compared to the MITC8 element in general.

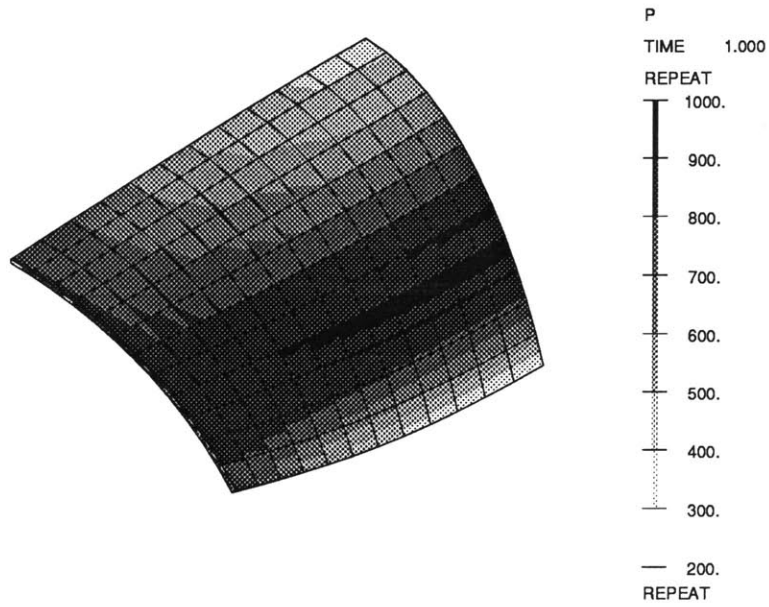
Figure 5-6c shows that for the  $10 \times 10$  element idealizations, the stress distributions



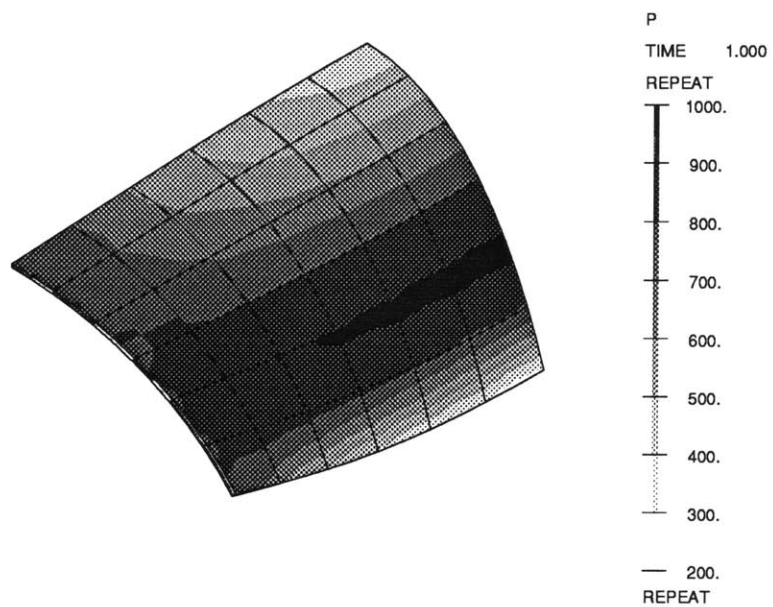
Shallow shell solution: 3.703/3.696  
 Deep shell theory: 3.610

(b) Analysis results.

Figure 5-5: Analysis of Scordelis-Lo cylindrical roof.

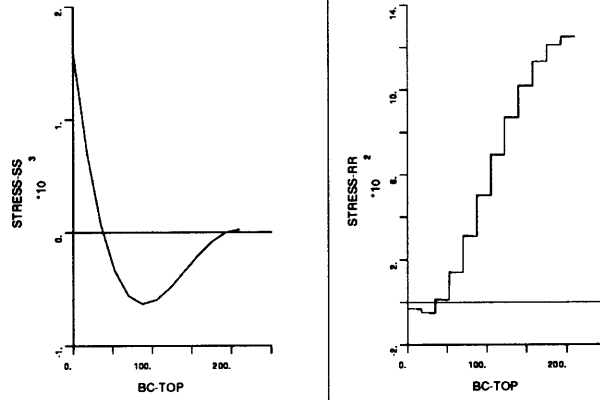


(c) Pressure band plot using the MITC4 element ( $12 \times 12$  mesh).

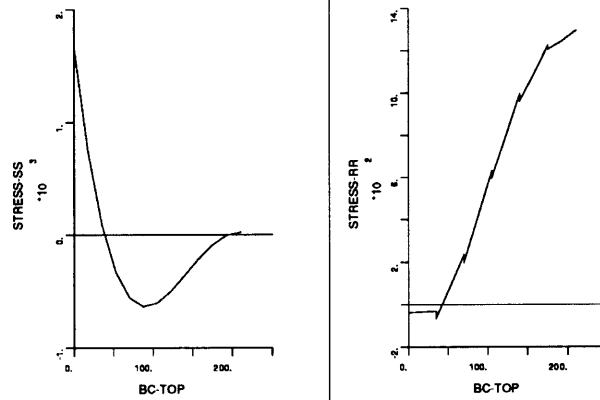


(d) Pressure band plot using the MITC9 element ( $6 \times 6$  mesh).

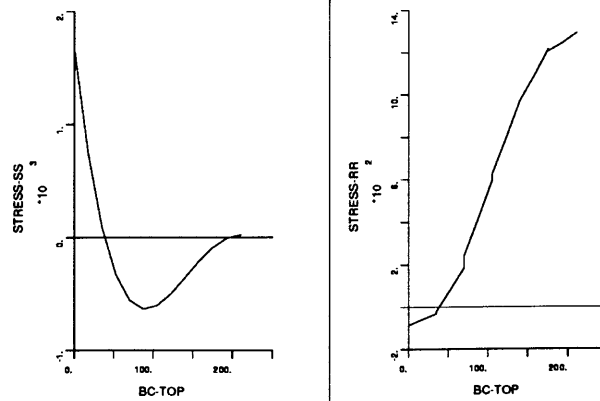
Figure 5-5 Continued.



(e) In-plane stress plot using the MITC4 element ( $12 \times 12$  mesh).



(f) In-plane stress plot using the MITC8 element ( $6 \times 6$  mesh).



(g) In-plane stress plot using the MITC9 element ( $6 \times 6$  mesh).

Figure 5-5 Continued.

obtained are in good agreement with the analytical solution. Figure 5-6d shows the pressure band plot for the mesh used in the stress calculations.

### 5.2.6 Fundamental Frequency of a Cantilever

A cantilever shown in Fig. 5-7a was analyzed again in order to verify the dynamical behavior of the MITC9 shell element in frequency analysis. Three equally spaced MITC9 elements are employed using the subspace iteration method in the frequency solution. A consistent mass discretization is used. The theoretical solution for this problem is presented in [Blevins, 1979].

Figure 5-7b shows the fundamental frequency for motion in the Y-Z plane (mode 2). In frequency analysis, the result obtained with only three MITC9 elements shows good agreement with the analytical solution.

### 5.2.7 Fundamental Frequency of a Simply Supported Plate

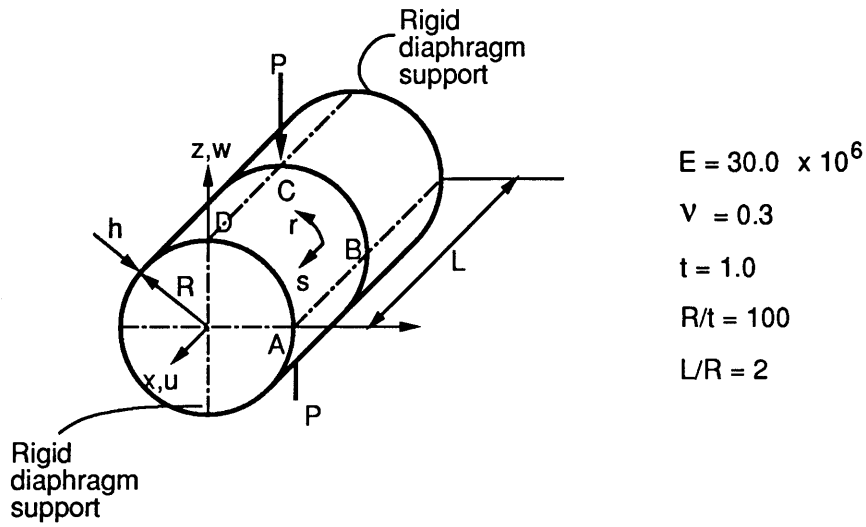
A simply supported square plate shown in Fig. 5-8a was analyzed in order to verify the dynamic behavior of the MITC9 shell element in frequency analysis. In order to calculate the asymmetric modes as well, the full plate is modeled using  $4 \times 4$  uniform meshes. A subspace iteration method is employed using the consistent mass matrix in the frequency solution. The theoretical solution for this problem is also presented in [Blevins, 1979].

Figure 5-8b shows the natural frequencies obtained using the MITC8 and MITC9 elements. In this analysis, the results obtained with MITC elements show good agreement with the analytical solution. Notice that the MITC9 element performs better than the MITC8 element in the calculation of the higher modes.

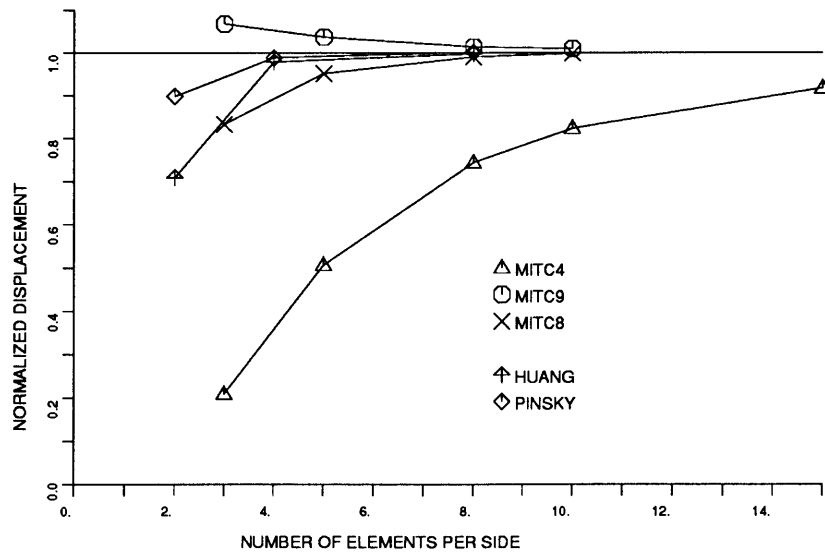
### 5.2.8 Analysis of a Cantilever under Large Displacement

The cantilever shown in Fig. 5-9a has been analyzed using the MITC9 element. The finite element model consists of two MITC9 shell elements, as shown in Fig. 5-9b. The



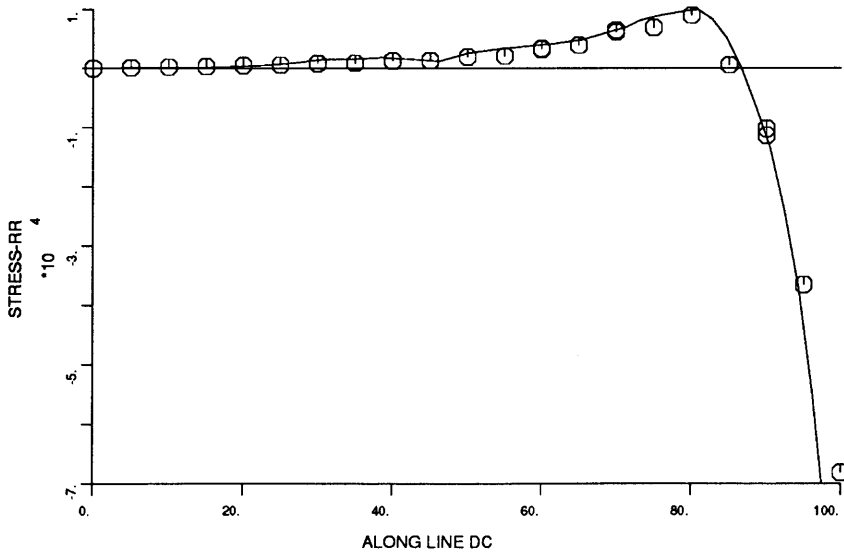
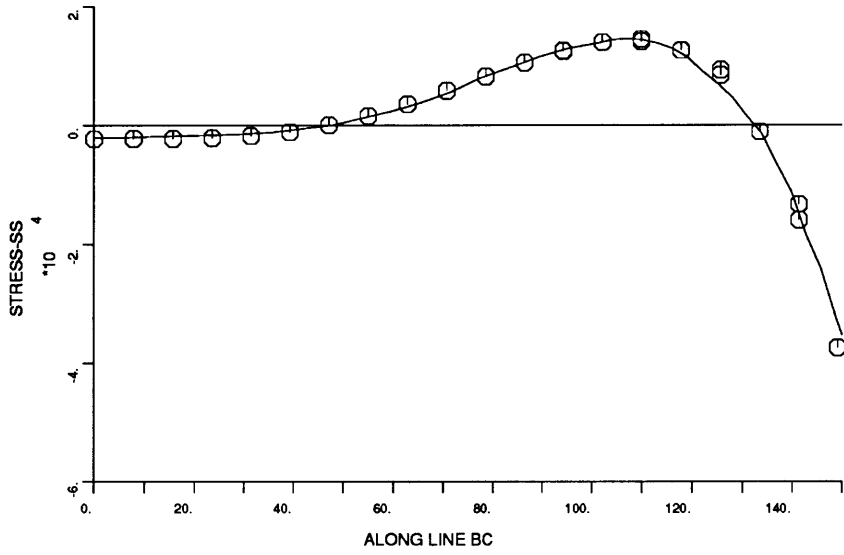


(a) Physical model considered.



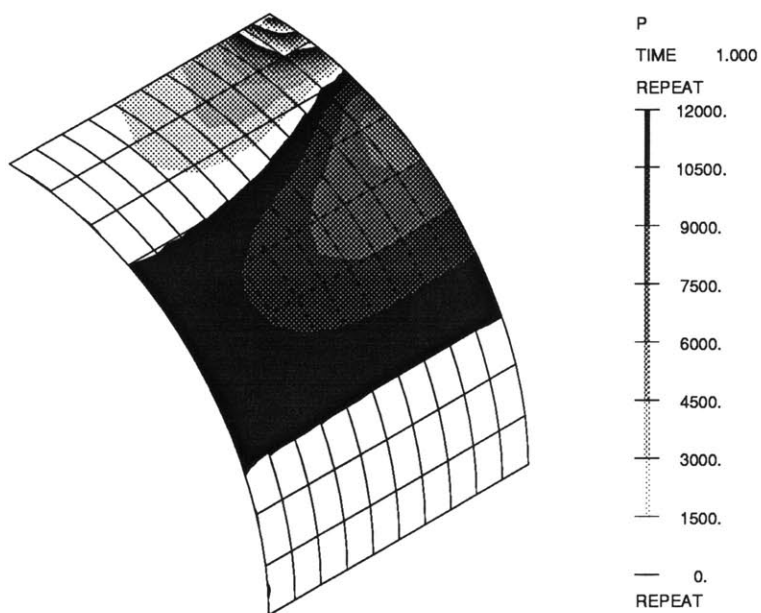
(b) Analysis results.

Figure 5-6: Analysis of a pinched cylindrical shell.



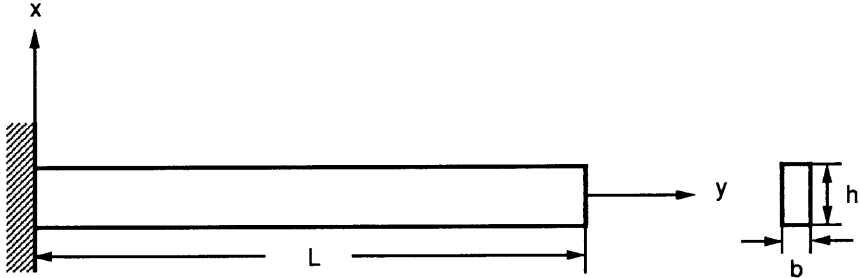
(c) In-plane stress plots using the MITC9 element ( $10 \times 10$  mesh).

Figure 5-6 Continued.



(d) Pressure band plot using the MITC9 element ( $10 \times 10$  mesh).

Figure 5-6 Continued.



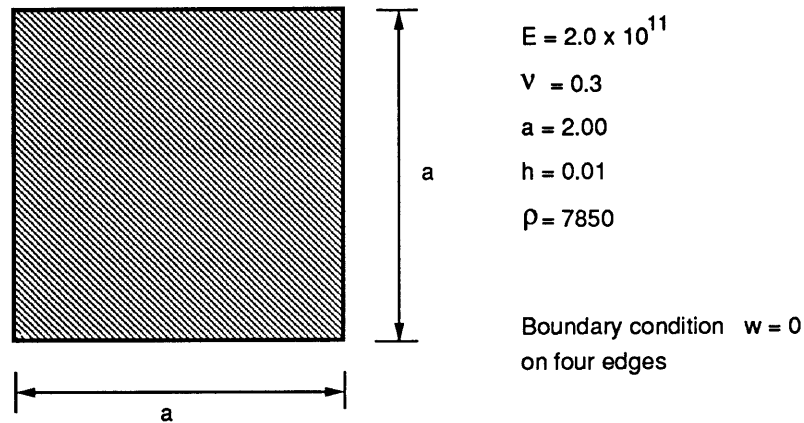
$L = 1.0$                        $E = 2.0 \times 10^{11}$   
 $b = 0.05$                        $\nu = 0.30$   
 $h = 0.10$  (thickness)       $\rho = 7800$

(a) Physical model considered.

Beam theory	MITC9
81.80	81.19

(b) Analysis results.

Figure 5-7: Fundamental frequency of a cantilever.



(a) Physical model considered.

Mode Number	Reference	MITC8 (ratio)	MITC9 (ratio)
1	12.00	12.03 (1.003)	12.03 (1.003)
2	29.99	30.56 (1.019)	30.10 (1.004)
3	29.99	30.56 (1.019)	30.10 (1.004)
4	47.99	50.39 (1.050)	49.55 (1.033)
5	59.98	64.39 (1.073)	56.36 (0.940)
6	59.98	64.39 (1.073)	56.36 (0.940)

(b) Analysis results.

Figure 5-8: Fundamental frequency of a simply supported plate.

load is applied in twenty equal load steps in a large displacement analysis with stiffness reformation and equilibrium iterations using the full Newton method in each step. Figure 5-9c shows the solution results obtained for tip rotation and displacements. It is observed that even using only two elements to model the cantilever, excellent results are obtained for up to 180 degrees of rotations. The standard isoparametric 9-node element with full integration, which matches the exact result in linear analysis, locks in the large displacement solution.

Table 5-1 summarizes the number of equilibrium iterations required for each time step up to ten time steps. Table 5-2 shows the convergence ratio for out-of-balance energy at time step 10. Three types of nonlinear stiffness matrices which have been used in this numerical test are:

$\mathbf{K}_{NL}^{DI}$  Directly interpolated tangent stiffness. In this case, the assumed strain interpolation is ignored in the nonlinear stiffness matrix construction. This formulation has been used in the existing MITC8 shell element.

$\mathbf{K}_{NL}^{AS-1}$  Assumed strain tangent stiffness matrix with first order rotations only. Hence in the construction of the nonlinear stiffness matrix, only the linear terms in Eq. 3.16 are kept in the formulation.

$\mathbf{K}_{NL}^{AS-2}$  Assumed strain tangent stiffness with second order rotations included. In this case, the assumed strain interpolation is also accounted for in the construction of nonlinear incremental strain tensor. Hence this formulation includes every term that can be considered in nonlinear incremental strain calculations. This formulation has been used for the MITC9 and the new MITC8<sup>N</sup> shell elements.

Notice that in all three cases, the linear stiffness matrix and out of balance load vector were constructed using the formulation presented in Chapter 3. Hence the use of different nonlinear stiffness matrices affects only the rates of convergence in the equilibrium iterations.

First, it is observed that inclusion of the second order rotations in the nonlinear stiffness construction is crucial. The convergence rate of the element with  $\mathbf{K}_{NL}^{AS-1}$  rapidly slows down as the geometric nonlinearity becomes large.

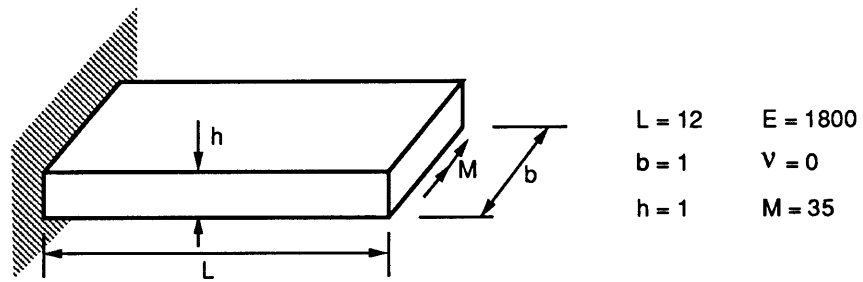
The element with  $\mathbf{K}_{NL}^{DI}$  shows better convergence compared to the element with  $\mathbf{K}_{NL}^{AS-1}$ . However this element also loses quadratic convergence as geometric nonlinearity becomes large (see Table 5-2).

Next observation is that the assumed strain formulation should be accounted for in order to keep full quadratic convergence even in the analysis with large geometric nonlinearity. The last columns of Tables 5-1 and 5-2 show full quadratic convergence when using the element with  $\mathbf{K}_{NL}^{AS-2}$  (the MITC9 and MITC9<sup>I</sup> element).

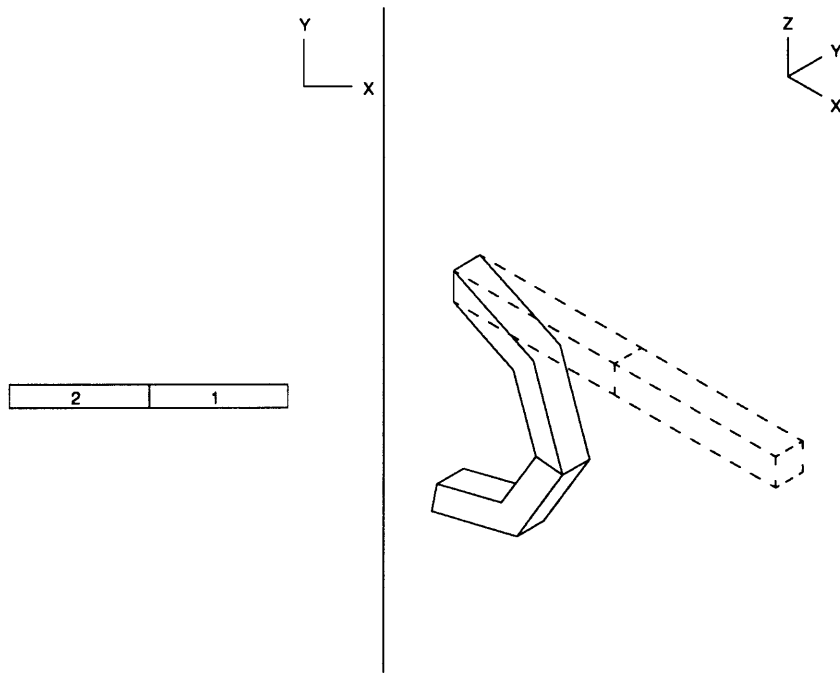
The MITC8 element employs  $\mathbf{K}_{NL}^{DI}$  because of its simplicity in the implementation. However using the computational scheme presented in Sec. 4.4, the exact nonlinear stiffness matrix can be constructed without increasing the computation time. Individual construction time of  $\mathbf{K}_{NL}^{AS-2}$  is slightly higher than the time required for  $\mathbf{K}_{NL}^{DI}$ , but since the total number of iterations required for the element using  $\mathbf{K}_{NL}^{AS-2}$  is smaller, the total computational time is reduced.

### 5.2.9 Large Displacement Analysis of a Simply-Supported Plate

The simply supported square plate subjected to a uniformly distributed pressure shown in Fig. 5-10a was analyzed to study its large deflection response. Because of symmetry conditions only one quarter of the plate is modeled using  $2 \times 2$  MITC9 elements. Constraint equations are used to model uniform in-plane edge displacements. In the numerical solution, the loading is applied in 22 load steps up to the final load parameter  $K = qa^4/Eh^4 = 500$ . The computed center deflection ratio  $w/h$  as a function of the load parameter  $K$  is shown in Fig. 5-10b. The computed displacement response agrees very closely with the solution given by Levy [Levy, 1942].



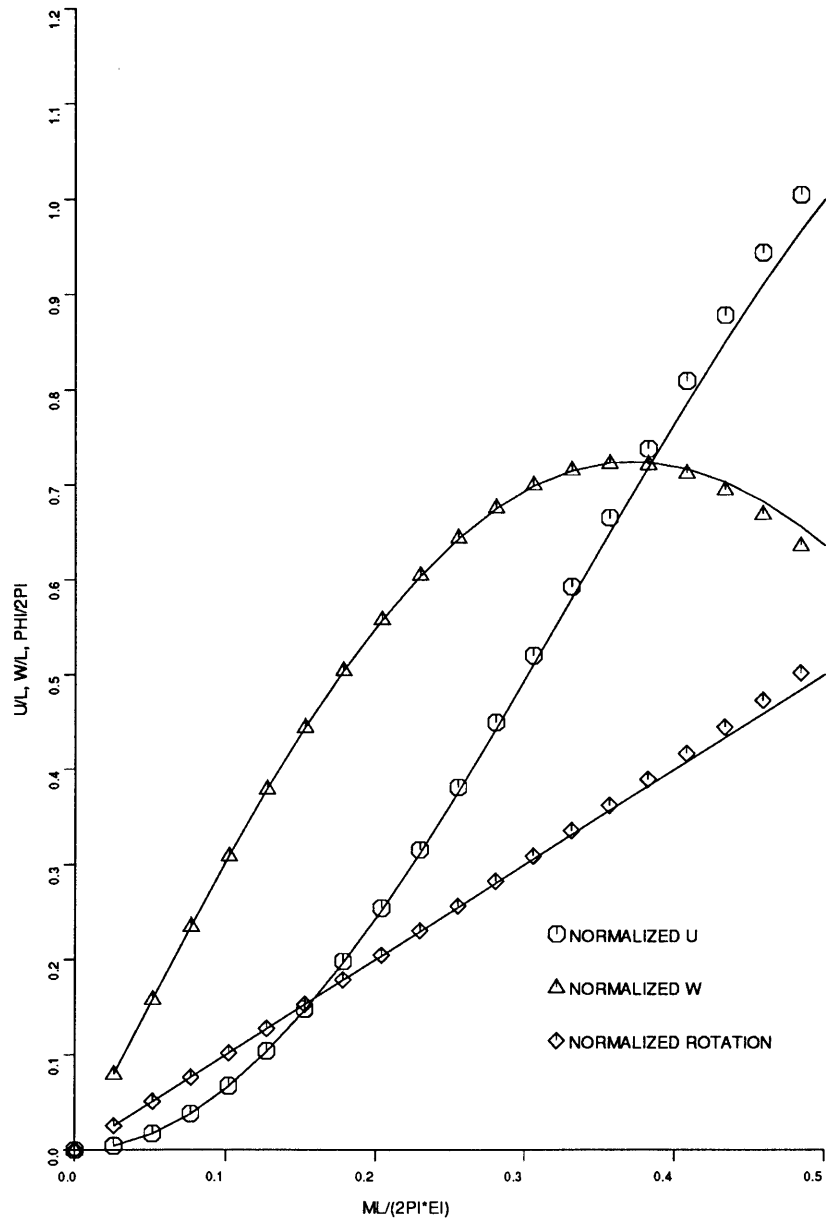
(a) Physical model considered.



(b) Finite element discretization and the deformed configuration.

Figure 5-9: A cantilever under large displacement.





(c) Analysis results for the tip rotation and displacements.

Figure 5-9 Continued.

Table 5-1: Number of iterations for the cantilever analysis using the MITC9 element.

Time Step	$\mathbf{K}_{NL}^{DI}$	$\mathbf{K}_{NL}^{AS-1}$	$\mathbf{K}_{NL}^{AS-2}$
1	4	4	4
2	4	5	4
3	4	7	4
4	5	9	4
5	5	12	4
6	5	15	5
7	5	20	5
8	6	26	5
9	7	36	5
10	9	50	5
Total Iterations	54	184	45
Total CPU Time	348	1201	340

$\mathbf{K}_{NL}^{DI}$ : Directly interpolated tangent stiffness.

$\mathbf{K}_{NL}^{AS-1}$ : Assumed strain tangent stiffness with first order rotations only.

$\mathbf{K}_{NL}^{AS-2}$ : Assumed strain tangent stiffness with second order rotations included.

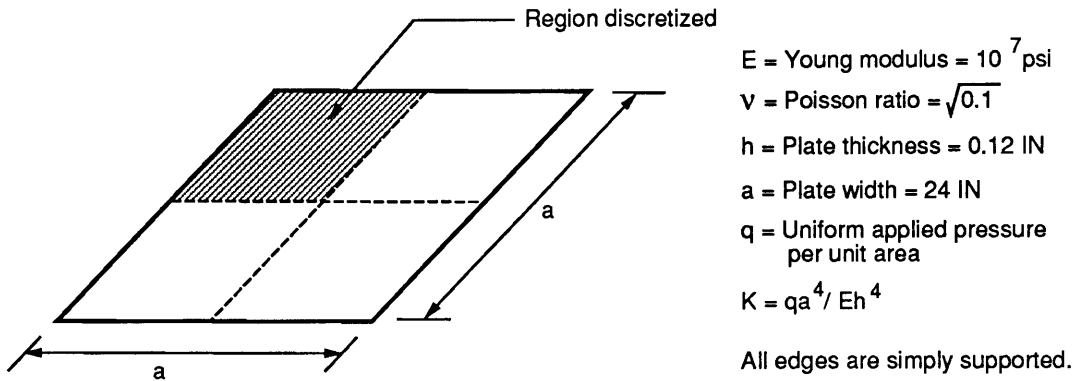
Table 5-2: Convergence ratio for the out-of-balance energy at time step 10.

Iteration	$\mathbf{K}_{NL}^{DI}$	$\mathbf{K}_{NL}^{AS-1}$	$\mathbf{K}_{NL}^{AS-2}$
1	$0.56 \times 10^{+1}$	$0.48 \times 10^{+0}$	$0.87 \times 10^{+1}$
2	$0.35 \times 10^{-1}$	$0.30 \times 10^{+0}$	$0.34 \times 10^{-1}$
3	$0.83 \times 10^{-2}$	$0.21 \times 10^{+0}$	$0.18 \times 10^{-2}$
4	$0.13 \times 10^{-2}$	$0.15 \times 10^{+0}$	$0.49 \times 10^{-4}$
5	$0.14 \times 10^{-3}$	$0.11 \times 10^{+0}$	$0.93 \times 10^{-8}$
6	$0.14 \times 10^{-4}$	$0.85 \times 10^{-1}$	(Converged.)
7	$0.14 \times 10^{-5}$	$0.64 \times 10^{-1}$	
8	$0.15 \times 10^{-6}$	$0.48 \times 10^{-1}$	
9	$0.16 \times 10^{-7}$	$0.37 \times 10^{-1}$	
10	(Converged.)	$0.28 \times 10^{-1}$	
11		$0.22 \times 10^{-1}$	
12		$0.17 \times 10^{-1}$	
13		$0.13 \times 10^{-1}$	
14		$0.10 \times 10^{-1}$	
15		$0.81 \times 10^{-2}$	
16		$0.64 \times 10^{-2}$	
17		$0.51 \times 10^{-2}$	
18		$0.41 \times 10^{-2}$	
19		$0.32 \times 10^{-2}$	
20		$0.26 \times 10^{-2}$	
21		$\vdots$	

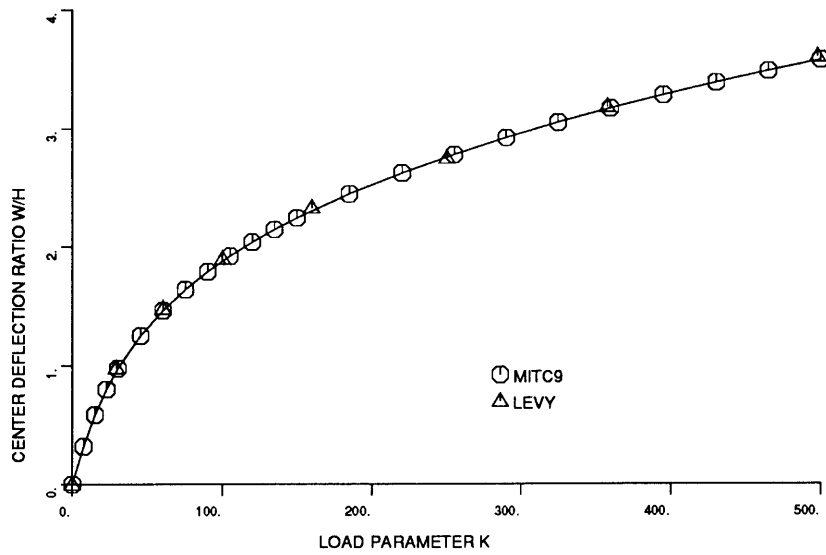
$\mathbf{K}_{NL}^{DI}$ : Directly interpolated tangent stiffness.

$\mathbf{K}_{NL}^{AS-1}$ : Assumed strain tangent stiffness with first order rotations only.

$\mathbf{K}_{NL}^{AS-2}$ : Assumed strain tangent stiffness with second order rotations included.



(a) Physical model considered.



(b) Analysis results.

Figure 5-10: Large displacement analysis of a simply-supported plate.

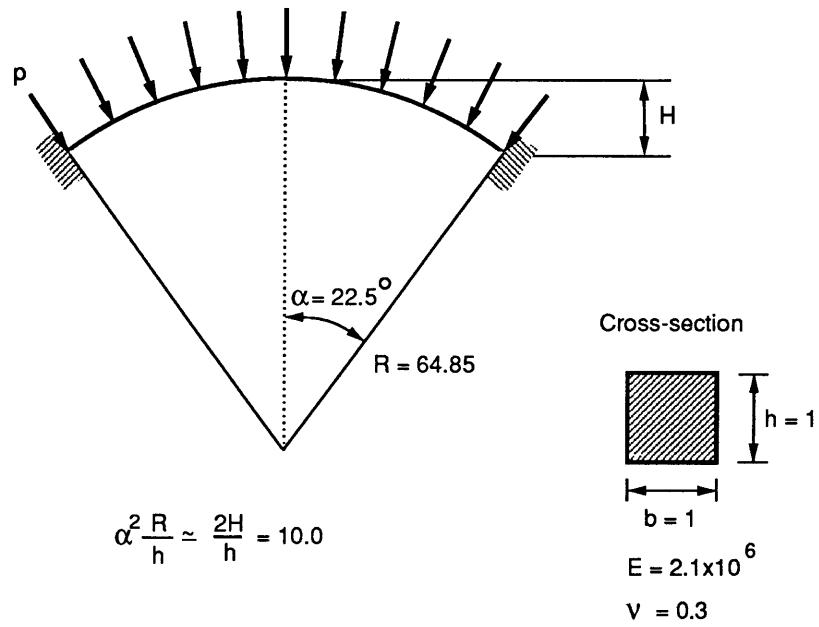
### 5.2.10 Linearized Buckling Analysis of a Circular Arch

A circular arch with fixed ends shown in Fig. 5-11a was considered. The arch is subjected to a distributed load. An analysis is performed to calculate estimates of the applied distributed load intensities corresponding to the first in-plane buckling modes of the arch. A linearized buckling analysis is performed using 10 equally spaced shell elements. Since the first buckling mode is expected to be skew-symmetric, the full arch is modeled in the analysis even though the arch structure has an axis of symmetry. The linearized buckling analysis involves two steps. First, the displacement response is calculated for the unit distributed load. Next, using the deformed geometry corresponding to the prescribed external loading, an eigenvalue problem is solved to obtain the estimates of the linearized buckling distributed load intensities. Figures 5-11b shows the analysis results compared to the analytical solution [Timoshenko and Gere, 1961].

Since the value of nonlinear stiffness matrix is directly used in the linearization, exact construction of the nonlinear stiffness matrix is necessary. However, it is observed that the directly interpolated nonlinear stiffness matrix also gives accurate results (the MITC8 element) for this problem.

### 5.2.11 Large Deflection Analysis of a Shallow Cylindrical Shell

A shallow cylindrical shell with a concentrated central load was analyzed to study its large deflection behavior. The longitudinal boundaries are hinged and immobile whereas the curved edges are completely free (see Fig. 5-12a). The structure exhibits a snap-through as well as a snap-back phenomena with horizontal and vertical tangents. Using the symmetry of the structure and the load, only one quarter of the cylinder is analyzed using  $3 \times 3$  MITC9 elements. The load-displacement control method is used in the analysis [ADINA R&D, 1987]. Figure 5-12b shows the analysis results compared to the solution obtained by Sabir and Lock [Sabir and Lock, 1973].

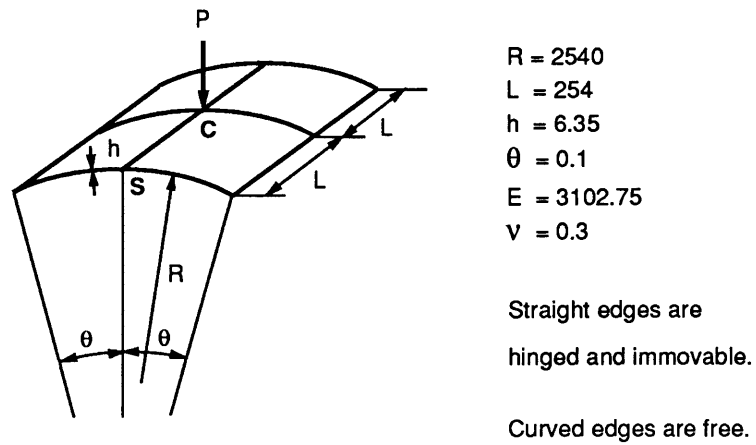


(a) Physical model considered.

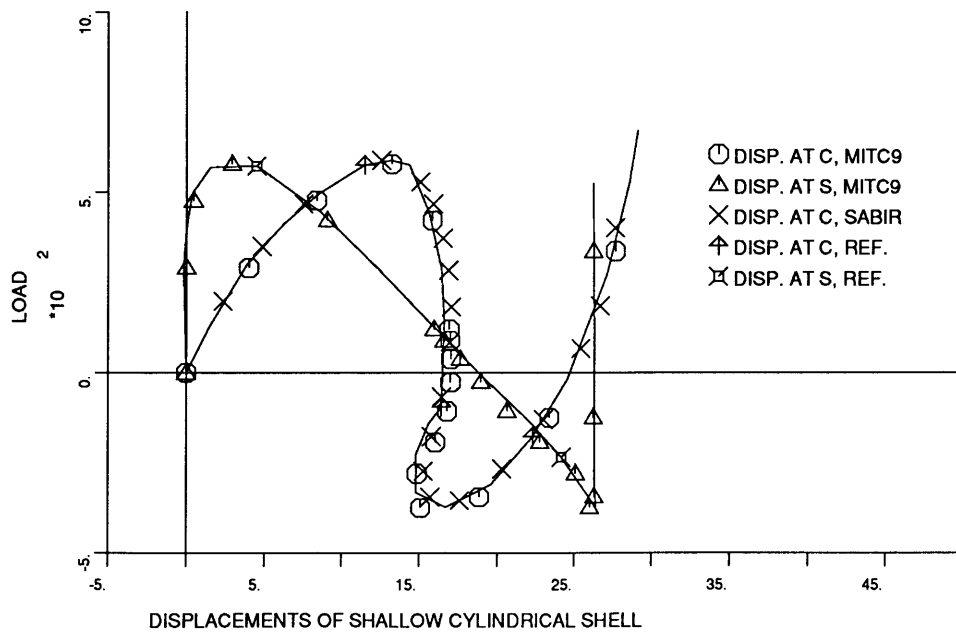
Reference Solution	MITC8	MITC9
83.0	82.7	82.9

(b) Analysis results.

Figure 5-11: Linearized buckling analysis of a circular arch.



(a) Physical model considered.



(b) Analysis results.

Figure 5-12: Analysis of a shallow cylindrical shell.

# Chapter 6

## Concluding Remarks

New plate and general shell finite elements for nonlinear analysis have been developed. The formulation corresponds to the use of a mixed variational principle. The independent strain interpolations are “tied internally” to the interpolations of the displacements/section rotations; hence the only final element unknowns are the nodal point displacements and section rotations. The element stiffness matrices are calculated using “full” numerical integration and do not contain spurious zero energy modes. The new plate and shell elements have the following important properties:

- The elements are formulated using three-dimensional continuum mechanics theory; therefore the use of the elements is not restricted by application of a specific shell theory. Also the formulation does not depend on any special numerical parameters.
- The elements satisfy, to a high degree, the objectives of being mechanistically clear, mathematically stable, and accurate.
- The new computational scheme for mixed-interpolated shell elements reduces computation time in the calculation of the stiffness matrix by a factor of two compared to the existing procedure in the case of linear analysis.
- The nonlinear shell formulation with the assumed strain interpolations gives full quadratic convergence during the equilibrium iterations when the full Newton



method is used.

In this thesis, a number of MITC plate elements as well as a 9-node general nonlinear shell element have been presented and studied. The MITC plate elements are based on the previously proposed mathematical theory. It is interesting that the mathematical theory used in the formulation of the elements strictly asks for some point-tying and an integral-tying of the assumed transverse shear strain components to the transverse displacement/section rotations. However, the numerical results show that instead of the integral-tying, a point-tying can be used. The numerical results from the point-tying are as accurate as those of the integral-tying; and for both triangular and quadrilateral elements, the point-tying is computationally more efficient. Hence, the point-tying scheme of the shear strains is employed for the development of the new 9-node general nonlinear shell element.

It has been demonstrated that the elements are very effective and reliable both in linear and nonlinear analyses. The solution results obtained are most encouraging. The success of the MITC shell elements is due to their sound mathematical foundations in the plate formulation, although a mathematical convergence study of the in-plane strain interpolation of the element is still not available. Hence, future work should focus on the analytical study of membrane strain interpolation, as well as the extension of the other MITC plate elements to general shell elements. To model structures with higher nonlinearity or for the analysis of structures with complicated loading conditions, the development of even higher-order mixed-interpolated shell elements is desired (e.g. MITC16 shell element). Also, the development of triangular shell elements (e.g. the MITC7 or MITC12 shell elements) would be valuable since the triangular geometry is employed extensively in many geometric modellers for automatic mesh constructions.

# References

- [ADINA R&D, 1987] ADINA R&D. ADINA—A finite element program for automatic dynamic incremental nonlinear analysis. Report 87-1, ADINA R&D, Watertown, MA., 1987.
- [Argyris, 1982] J. Argyris. An excursion into large rotations. *Computer Methods in Applied Mechanics and Engineering*, 32:85–155, 1982.
- [Bathe and Bolourchi, 1980] K. J. Bathe and S. Bolourchi. A geometric and material nonlinear plate and shell element. *Computers & Structures*, 11:23–48, 1980.
- [Bathe and Brezzi, 1985] K. J. Bathe and F. Brezzi. On the convergence of a four-node plate bending element based on Mindlin/Reissner plate theory and a mixed interpolation. In J. R. Whiteman, editor, *Proceedings of the Conference on Mathematics of Finite Elements and Applications V*, pages 491–503. Academic Press, 1985.
- [Bathe and Brezzi, 1987] K. J. Bathe and F. Brezzi. A simplified analysis of two plate bending elements — the MITC4 and MITC9 elements. In G. N. Pande and J. Middleton, editors, *Proceedings of the International Conference on Numerical Methods in Engineering (NUMETA 87)*, page D46, Wales, 1987. University College of Swansea.
- [Bathe and Dvorkin, 1985] K. J. Bathe and E. Dvorkin. A four-node plate bending element based on Mindlin/Reissner plate theory and a mixed interpolation. *International Journal for Numerical Methods in Engineering*, 21:367–383, 1985.
- [Bathe and Dvorkin, 1986] K. J. Bathe and E. Dvorkin. A formulation of general shell elements — the use of mixed interpolation of tensorial components. *International Journal for Numerical Methods in Engineering*, 22:697–722, 1986.
- [Bathe and Ho, 1981a] K. J. Bathe and L.-W. Ho. A simple and effective elements for analysis of general shell structure. *Computers & Structures*, 13:673–681, 1981.
- [Bathe and Ho, 1981b] K. J. Bathe and L. W. Ho. Some results in the analysis of thin shell structures. In Wunderlich et al., editors, *Nonlinear Finite Element Analysis in Structural Mechanics*, pages 72–100, Berlin, 1981. Springer-Verlag.

- [Bathe *et al.*, 1983] K. J. Bathe, E. Dvorkin, and L. W. Ho. Our discrete-kirchhoff and isoparametric shell elements for nonlinear analysis — an assessment. *Computers & Structures*, 16(1–4):89–98, 1983.
- [Bathe *et al.*, 1989a] K. J. Bathe, F. Brezzi, and S. W. Cho. The MITC7 and MITC9 plate bending elements. *Computers & Structures*, 32(3/4):797–814, 1989.
- [Bathe *et al.*, 1989b] K. J. Bathe, S. W. Cho, M. L. Bucelem, and F. Brezzi. On our MITC plate bending/shell elements. In *Symposium on Analytical and Computational Models of Shells, ASME Winter Annual Meeting*, pages 261–278, 1989.
- [Bathe, 1982] K. J. Bathe. *Finite Element Procedures in Engineering Analysis*. Prentice-Hall, Inc., Englewood Cliffs, 1982.
- [Bathe, 1986] K. J. Bathe. *Finite Element Procedures for solids and structures – Non-linear Analysis*. M.I.T Center for Advanced Engineering Study, 1986. Video Course Study Guide.
- [Batoz *et al.*, 1980] J.-L. Batoz, K. J. Bathe, and L.-W. Ho. A study of three-node triangular plate bending elements. *International Journal for Numerical Methods in Engineering*, 15:1771–1812, 1980.
- [Blevins, 1979] R. D. Blevins. *Formulas for Natural Frequency and Mode Shape*. Van Nostrand Reinhold Company, 1979.
- [Brezzi and Bathe, 1986] F. Brezzi and K. J. Bathe. Studies of finite element procedures — the Inf-Sup condition, equivalent forms and applications. In K. J. Bathe and D. R. J. Owen, editors, *Reliability of Methods for Engineering Analysis*, pages 197–219, Swansea, 1986. Pineridge Press.
- [Brezzi *et al.*, 1987] F. Brezzi, J. Douglas, Jr., M. Fortin, and L. D. Marini. Efficient rectangular mixed finite elements in two and three space variables. *RAIRO MAN, Mathematical Modeling and Numerical Analysis*, 21:581–604, 1987.
- [Brezzi *et al.*, 1989] F. Brezzi, K. J. Bathe, and M. Fortin. Mixed-Interpolated elements for Reissner-Mindlin plates. *International Journal for Numerical Methods in Engineering*, 28:1787–1801, 1989.
- [Crisfield, 1984] M. A. Crisfield. A quadratic mindlin element using shear constraints. *Computers & Structures*, 18(5):833–852, 1984.
- [Crisfield, 1985] M. A. Crisfield. Some recent research on numerical techniques for structural analysis. In J. Middleton and G. N. Pande, editors, *Proceeding of the International Conference on Numerical Methods in Engineering (NUMETA 85)*, pages 565–575, Wales, UK, 1985. University College of Swansea.

- [Douglas, Jr. and Roberts, 1985] J. Douglas, Jr. and J. E. Roberts. Global estimates for mixed methods for second-order elliptic equations. *Mathematics of Computation*, 44:39–52, 1985.
- [Dvorkin and Bathe, 1984] E. Dvorkin and K. J. Bathe. A continuum mechanics based four-node shell element for general nonlinear analysis. *Engineering Computations*, 1:77–88, 1984.
- [Green and Zerna, 1968] A. E. Green and W. Zerna. *Theoretical Elasticity*. Oxford University Press, second edition, 1968.
- [Hägglblad and Bathe, 1990] B. Häggblad and K. J. Bathe. Specifications of boundary conditions for Reissner-Mindlin plate bending finite elements. *International Journal for Numerical Methods in Engineering*, 30:981–1011, 1990.
- [Hinton and Huang, 1986] E. Hinton and H. C. Huang. A family of quadrilateral mindlin plate elements with substitute shear strain fields. *Computers & Structures*, 23(3):409–431, 1986.
- [Huang and Hinton, 1984] H. C. Huang and E. Hinton. A nine node lagrangian mindlin plate element with enhanced shear interpolation. *Engineering Computations*, 1:369–379, 1984.
- [Huang and Hinton, 1986] H. C. Huang and E. Hinton. A new nine node degenerated shell element with enhanced membrane and shear interpolation. *International Journal for Numerical Methods in Engineering*, 22:73–92, 1986.
- [Huang, 1987] H. C. Huang. Implementation of assumed strain degenerated shell elements. *Computers & Structures*, 25(1):147–155, 1987.
- [Hughes and Tezduyar, 1981] T. J. R. Hughes and T. E. Tezduyar. Finite elements based upon mindlin plate theory with particular reference to the four-node bilinear isoparametric element. *Journal of Applied Mechanics, Transactions of ASME*, 48:587–596, 1981.
- [Hughes *et al.*, 1977] T. J. R. Hughes, R. L. Taylor, and W. Kanoknukulchai. A simple and efficient finite element for plate bending. *International Journal for Numerical Methods in Engineering*, 11:1529–1543, 1977.
- [Hughes *et al.*, 1978] T. J. R. Hughes, M. Cohen, and M. Haroun. Reduced and selective integration techniques in the finite element analysis of plates. *Nuclear Engineering Design*, 46:203–222, 1978.
- [Jang and Pinsky, 1987] J. Jang and P. M. Pinsky. An assumed covariant strain based 9-node shell element. *International Journal for Numerical Methods in Engineering*, 24:2389–2411, 1987.

- [Jang and Pinsky, 1988] J. Jang and P. M. Pinsky. Convergence of curved shell elements based on assumed covariant strain interpolations. *International Journal for Numerical Methods in Engineering*, 26:329–347, 1988.
- [Lee and Wong, 1982] S. W. Lee and S. C. Wong. Mixed formulation finite elements for mindlin theory plate bending. *International Journal for Numerical Methods in Engineering*, 18:1297–1311, 1982.
- [Levy, 1942] S. Levy. Bending of rectangular plates with large deflections. Technical Report 846, National Advisory Committee for Aeronautics, 1942.
- [Lindberg *et al.*, 1969] G. M. Lindberg, M. D. Olson, and E. R. Cowper. New developments in the finite element analysis of shells. *National Research Council of Canada, Quarterly Bulletin of the Division of Mechanical Engineering and the National Aeronautical Establishment*, 4:1–38, 1969.
- [MacNeal, 1982] R. H. MacNeal. Derivation of element stiffness matrices by assumed strain distributions. *Nuclear Engineering Design*, 70:3–12, 1982.
- [Morley, 1963] L. S. D. Morley. *Skew Plates and Structures*. Pergamon Press, Oxford, 1963.
- [Park and Stanley, 1986] K. C. Park and G. M. Stanley. A curved  $C^0$  shell element based on assumed natural-coordinate strains. *Journal of Applied Mechanics, Transactions of ASME*, 53:278–290, 1986.
- [Raviart and Thomas, 1975] P. A. Raviart and J. M. Thomas. *A Mixed Finite Element Method for Second-Order Elliptic Problems*, volume 606 of *Lecture Notes in Mathematics*, pages 292–315. Springer-Verlag, Berlin, 1975.
- [Sabir and Lock, 1973] A. B. Sabir and A. C. Lock. The application of finite elements in the large deflection geometrically nonlinear behavior of cylindrical shells. In Brebbia A. and Tottenham H., editors, *Variational Methods in Engineering*, pages 7/66–7/75. Southampton University Press, 1973.
- [Scordelis and Lo, 1964] A. C. Scordelis and K. S. Lo. Computer analysis of cylindrical shells. *Journal of American Concrete Institute*, 61:539–560, 1964.
- [Simo, 1988] J. C. Simo. A framework for finite strain elastoplasticity based on maximum plastic dissipation and the multiplicative decomposition: Part I. continuum formulation. *Comput. Meths. Appl. Mech. Engrg.*, 66:199–219, 1988.
- [Sussman and Bathe, 1987] T. Sussman and K. J. Bathe. A finite element formulation for nonlinear incompressible elastic and inelastic analysis. *Computers & Structures*, 26:357–409, 1987.

- 
- [Taylor and Simo, 1985] R. L. Taylor and J. C. Simo. Bending and membrane elements for analysis of thick and thin shells. In J. Middleton and G. N. Pande, editors, *Proceeding of the International Conference on Numerical Methods in Engineering (NUMETA 85)*, pages 587–591, Wales, UK, 1985. University College of Swansea.
- [Tessler and Hughes, 1983] A. Tessler and T. J. R. Hughes. An improved treatment of transverse shear in the mindlin-type four-node quadrilateral element. *International Journal for Numerical Methods in Engineering*, 39:311–335, 1983.
- [Timoshenko and Gere, 1961] S. P. Timoshenko and J. M. Gere. *Theory of Elastic Stability*. McGraw-Hill, 1961.
- [Timoshenko and Goodier, 1970] A. P. Timoshenko and J. N. Goodier. *Theory of Elasticity*. McGraw-Hill, third edition, 1970.
- [Timoshenko and Woinowsky-Krieger, 1959] S. P. Timoshenko and S. Woinowsky-Krieger. *Theory of Plates and Shells*. MacGraw-Hill, second edition, 1959.